Theses and Dissertations | 1. Thesis and Dissertation Collection, all items

2012-09

Spectral Unmixing Applied to Desert Soils for the Detection of Sub-Pixel Disturbances

(Howard), Jessica Stuart

Monterey, California. Naval Postgraduate School

NAVAL POSTGRADUATE SCHOOL

MONTEREY, CALIFORNIA

THESIS

SPECTRAL UNMIXING APPLIED TO DESERT SOILS FOR THE DETECTION OF SUB-PIXEL DISTURBANCES

by

Jessica Stuart (Howard)

September 2012

Thesis Advisor:	Fred A. Kruse
Second Reader:	Richard C. Olsen

Approved for public release; distribution is unlimited

THIS PAGE INTENTIONALLY LEFT BLANK

REPORT DOCUMENTATION PAGE		*Form Approved OMB No. 0704-0188*
Public reporting burden for this collection of information is estimated to average 1 hour per response, including the time for reviewing instruction, searching existing data sources, gathering and maintaining the data needed, and completing and reviewing the collection of information. Send comments regarding this burden estimate or any other aspect of this collection of information, including suggestions for reducing this burden, to Washington headquarters Services, Directorate for Information Operations and Reports, 1215 Jefferson Davis Highway, Suite 1204, Arlington, VA 22202-4302, and to the Office of Management and Budget, Paperwork Reduction Project (0704-0188) Washington DC 20503.		
1. AGENCY USE ONLY *(Leave blank)*	**2. REPORT DATE** September 2012	**3. REPORT TYPE AND DATES COVERED** Master's Thesis
4. TITLE AND SUBTITLES Spectral Unmixing Applied to Desert Soils for the Detection of Sub-Pixel Disturbances		**5. FUNDING NUMBERS**
6. AUTHOR(S) Jessica Stuart (Howard)		
7. PERFORMING ORGANIZATION NAME(S) AND ADDRESS(ES) Naval Postgraduate School Monterey, CA 93943-5000		**8. PERFORMING ORGANIZATION REPORT NUMBER**
9. SPONSORING /MONITORING AGENCY NAME(S) AND ADDRESS(ES) N/A		**10. SPONSORING/MONITORING AGENCY REPORT NUMBER**
11. SUPPLEMENTARY NOTES The views expressed in this thesis are those of the author and do not reflect the official policy or position of the Department of Defense or the U.S. Government. IRB Protocol number _____N/A_____.		
12a. DISTRIBUTION / AVAILABILITY STATEMENT Approved for public release; distribution is unlimited		**12b. DISTRIBUTION CODE** A
13. ABSTRACT (maximum 200words) Desert areas cover approximately one-fifth of the Earth, making it important to understand how disturbance affects arid regions on a spectral level. Remote sensing technology can be used to detect and characterize surface disturbance both literally (visually) and non-literally (analytically). Non-literal approaches may even allow detection of anthropogenic-related surface disturbances that are not visible in individual images or color composites. This is achievable through identification of differences in spectral reflectance among like soil components, both chemical and biological. Previous research suggests that surface disturbances cause alteration of soil properties, making it feasible to detect variation in reflectance signatures. This research supports that assumption and has determined that disturbance-related changes do have unique spectral characteristics in hyperspectral imagery that are detectable, even at the sub-pixel level and using endmembers from geographically different yet geologically similar regions.		
14. SUBJECT TERMS spectral unmixing, mixture-tuned match filter, biological soil crusts, desert soils, hyperspectral		**15. NUMBER OF PAGES** 108
		16. PRICE CODE
17. SECURITY CLASSIFICATION OF REPORT Unclassified	**18. SECURITY CLASSIFICATION OF THIS PAGE** Unclassified	**19. SECURITY CLASSIFICATION OF ABSTRACT** Unclassified	**20. LIMITATION OF ABSTRACT** UU

THIS PAGE INTENTIONALLY LEFT BLANK

Approved for public release; distribution is unlimited

SPECTRAL UNMIXING APPLIED TO DESERT SOILS FOR THE DETECTION OF SUB-PIXEL DISTURBANCES

Jessica L. Stuart (Howard)
Civilian, United States Navy
B.S. Earth and Planetary Science, UC Santa Cruz, 2011

Submitted in partial fulfillment of the
requirements for the degree of

MASTER OF SCIENCE IN REMOTE SENSING INTELLIGENCE

from the

NAVAL POSTGRADUATE SCHOOL
September 2012

Author: Jessica Stuart (Howard)

Approved by: Fred A. Kruse
                 Thesis Advisor

                 Richard C. Olsen
                 Second Reader

                 Dan Boger
                 Chair, Department of Information Sciences

THIS PAGE INTENTIONALLY LEFT BLANK

ABSTRACT

Desert areas cover approximately one-fifth of the Earth, making it important to understand how disturbance affects arid regions on a spectral level. Remote sensing technology can be used to detect and characterize surface disturbance both literally (visually) and non-literally (analytically). Non-literal approaches may even allow detection of anthropogenic-related surface disturbances that are not visible in individual images or color composites. This is achievable through identification of differences in spectral reflectance among like soil components, both chemical and biological. Previous research suggests that surface disturbances cause alteration of soil properties, making it feasible to detect variation in reflectance signatures. This research supports that assumption and has determined that disturbance-related changes do have unique spectral characteristics in hyperspectral imagery that are detectable, even at the sub-pixel level and using endmembers from geographically different yet geologically similar regions.

THIS PAGE INTENTIONALLY LEFT BLANK

TABLE OF CONTENTS

LIST OF FIGURES

THIS PAGE INTENTIONALLY LEFT BLANK

LIST OF TABLES

THIS PAGE INTENTIONALLY LEFT BLANK

LIST OF ACRONYMS AND ABBREVIATIONS

ASD- Analytical Spectral Device

AVIRIS- Airborne Visible/Infrared Imaging Spectrometer

ASTER- Advanced Spaceborne Thermal emission and Reflection Radiometer

BSCs- Biological Soil Crusts/Cryptobiotic Soils

ENVI- Environment for Visualizing Images

FLAASH- Fast Line-of-sight Atmospheric Analysis of Spectral Hypercubes

FOV- Field of View

HSI- Hyperspectral Imagery

HYDICE- Hyperspectral Digital Imagery Collection Experiment

HyMAP- Hyperspectral Mapper

HyspIRI- Hyperspectral Infrared Imager

LWIR- Long Wave Infrared

MODTRAN- Moderate Resolution Atmospheric Radiance and Transmission Model

MF- Matched Filtering

MNF- Minimum Noise Fraction

MTMF- Mixture-tuned Matched Filter

MT- Mixture Tuning

NIR- Near Infrared

OHV- Off Highway Vehicle

PPI- Pixel Purity Index

SNR- Signal-to-Noise Ratio

SWIR- shortwave infrared

THIS PAGE INTENTIONALLY LEFT BLANK

I. INTRODUCTION

A study published by Doug V. Prose in 1985 looked at the persisting effects of military maneuvers on soils in the Mojave Desert (Prose, 1985). This study revealed that tracks left in a single pass of military equipment caused soil resistance (or electrical conductivity) 50% greater than in areas that were undisturbed. The study also indicated that despite diminished visible evidence, there were underlying effects in the soil such as vertical and lateral increases in bulk density and soil impenetrability. The implications are that even minimal surface disturbances have measurable impacts on desert soils that can serve as indicators of activity.

Based on the idea posed by Prose (1985), this thesis has sought to demonstrate that one can use endmembers from a geographically different yet geologically similar area in conjunction with satellite imagery, and spectral mixture analysis to detect sub-pixel surface disturbances related to anthropogenic uses in arid environments. Spectral unmixing allows analysis of the distribution of surface components within a single image picture element (pixel) not visible to the naked eye and can be exploited to detect signature changes related to anthropogenic surface disturbances (Goetz et al., 1985). Areas with high concentrations of altered soil components can be mapped and analyzed to gain understanding of the spatial extent and location of those changes; providing comprehensive knowledge of target areas. To be able to use these soil components for such applications gives us an edge on adversaries allowing us to track activity locations in a timely manner. By creating a library of spectral properties of soil types exposed to various surface disturbances in geologically similar conditions, surface disturbances in remote areas should be spectrally detectable on a sub pixel level in imaging spectrometer data; thus providing a means of analyzing large areas for signs of activity.

As a spaced based asset, this technology poses the opportunity to conduct adversary tracking in regions that are highly inaccessible. The ability to use endmembers from easily accessed areas to detect spectral changes in desert soils in general, enables quick response and potential mitigation efforts to be more effective in the long haul. As adversaries continue to adapt to current remote sensing methods, it becomes more

difficult to maintain an informational edge. This makes it necessary to develop new methods for tracking their activity and whereabouts. Detection and mapping of disturbed soils using remote sensing and hyperspectral imaging technology is one approach that may contribute to the solution of this problem, however, this area requires further research to fully establish the potential of this technology.

II.   THE PHYSICS BEHIND REMOTE SENSING

A.   REMOTE SENSING

The term remote sensing refers to the ability to conduct measurements and interpretation of events without being present at the location being studied (Goetz and Rowan, 1981). Remote Sensing instruments make measurements by utilizing solutions to the wave equation:

$$E = Ae^{i(kr - \omega t + \phi)} \tag{1}$$

where:

A is the wave amplitude,

ω is the angular frequency,

ϕ is the phase,

k is the wave vector in some propagation medium (Elachi and Van Zyl, 2006).

Remote sensing is useful for a variety of applications including mineral distribution mapping, geologic formation mapping, pollution studies, and geo-ecological relationships (Gathercole, 1987). Use of remote systems such as satellite borne sensors is possible because when light interacts with materials on the surface of the earth it is scattered, transmitted, reflected and absorbed by those materials (Figure 1). Some of that light is then directed in the form of photons toward an observing sensor and measured as radiance (Clark, 1999). The radiance measured by the sensor is calculated using the radiance equation (2) below after Gao and Goetz (1990).

$$L_0(\lambda) = L_{sun}(\lambda)\, \tau(\lambda)\, R(\lambda)\, \cos(\theta) + L_{path}(\lambda) \tag{2}$$

where:

$L_0(\lambda)$ is the radiance observed by the sensor,

$L_{sun}(\lambda)$ is the radiance above the atmosphere from the sun,

$\tau(\lambda)$ is the total atmospheric transmittance,

$R(\lambda)$ is reflectance from the surface material,

θ is the angle of incidence of the sensor,

$L_{path}(\lambda)$ is the path of the scattered radiance.
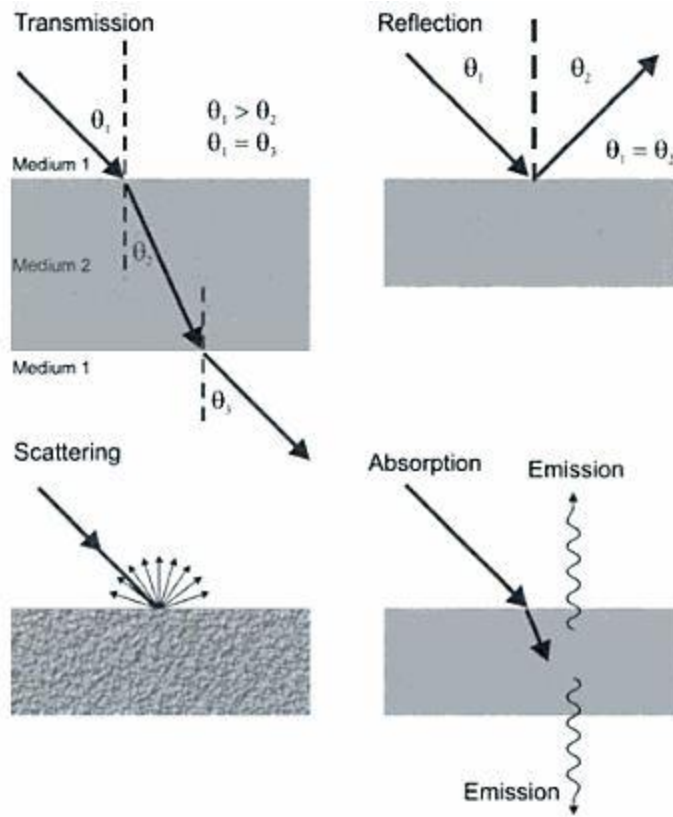
Figure 1.   The above figure shows how incident light interacts with surface materials via transmission, reflection, scattering and absorption (From Olsen, 2007).

The accuracy of measuring land surface characteristics remotely is dependent on spectral, spatial, temporal, and radiometric resolution (Jensen, 1983). These different types of resolution are the dimension and number of wavelength intervals a sensor is sensitive to, the smallest angular or linear separation between imaged surface materials that can be determined by the sensor, how often the sensor is imaging the area, and how

4

sensitive a given sensor is to differences in the radiant flux being measured, respectively (Jensen, 1983). It is the spatial, spectral, temporal, and radiometric resolutions that determine the sensors overall capability in distinguishing one signal from another (Jensen, 1983). In hyperspectral imagery, these four resolution types are utilized to sample surface materials using contiguous bands allowing for identification of those materials. This is done via spectral absorption features in the collected signal, or spectrum (Goetz et al., 1985). This capability is discussed in detail in the Imaging Spectrometry section.

B.   THE ELECTROMAGNETIC SPECTRUM

Electromagnetic radiation can come from a number of sources, mostly all associated with a changing of energy state of electrons (Olsen, 2007). It travels in the form of transverse waves that result in a continuous spectrum of frequencies or wavelengths (Olsen, 1979). The electromagnetic radiation concerning us here is the kind that interacts with matter, called incident radiation (Olsen, 2007). Generation of these electromagnetic waves occurs when energy is transformed from kinetic, chemical, thermal, and other similar sources (Elachi and Van Zyl, 2006). This electromagnetic radiation is how energy gets from some surface material to an optical sensor and is divided into a series of spectral regions that are illustrated in Figure 2 (Elachi and Van Zyl, 2006).
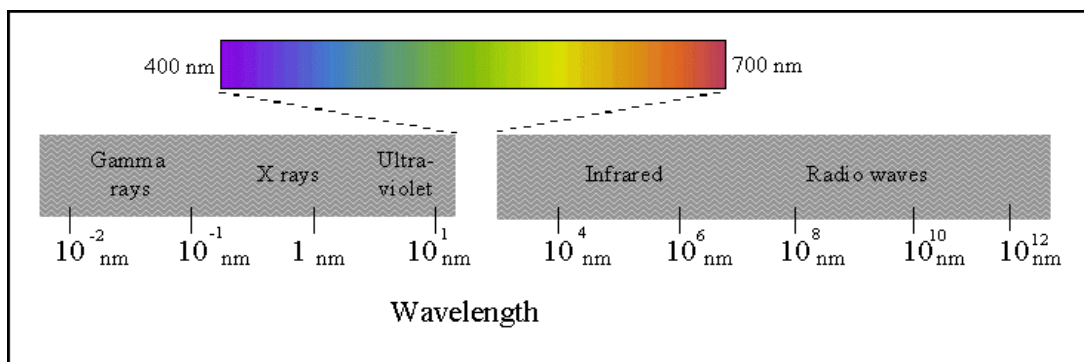
Figure 2.   This figure from
http://www.astro.cornell.edu/academics/courses/astro201/emspectrum.htm
shows the divisions of the electromagnetic spectrum. The region most often
exploited by remote sensing scientists range from the ultraviolet to infrared
portions of the spectrum (Halvatzis, 2002, Goetz and Rowan, 1981).

5

The spectral regions most often exploited by remote sensing scientists are the visible and infrared (Halvatzis, 2002). These regions have wavelengths that typically fall between 0.4 and 15 micrometers (400–1500 nm), though different applications will utilize different portions of this range (Goetz and Rowan, 1981; Halvatzis, 2002). The wavelength range utilized is based on the material being analyzed and which spectral region will most easily distinguish this material from the others in the imagery (Jensen, 1983). It is widely agreed that the most appropriate regions for remotely sensing vegetation, soils, and rocks is the 0.4–2.5 micrometer (400–2500 nm) range; because of the detailed information on the unique properties of surface materials it can provide, even at the sub-pixel level (Goetz and Rowan, 1981; Jensen, 1983; Kruse et al, 2004).

C.   IMAGING SPECTROMETRY

Imaging Spectrometry data measures reflectance or emissivity of surface materials using up to hundreds of spectral bands (Figure3) (Goetz et al., 1985; Kruse et al., 2003). This technique allows for the collection of an entire spectral signature for every surface material within that image on a picture element (pixel) by pixel basis (Goetz et al., 1985). Spectral features are a response to chemical bonds specific to a given material based on chemistry and structure, known as electronic and vibrational processes (Figure 2) (Clark, 1999) called absorption features (Goetz et al., 1985). Absorption features are the phenomena in which a collected spectrum from a material will have varying maxima and minima across the associated wavelength range. Minima are related to absorption bands that are somewhat unique to the material and contribute to its characteristic spectrum (Goetz et al., 1985; Jensen, 2007; Clark, 1999).
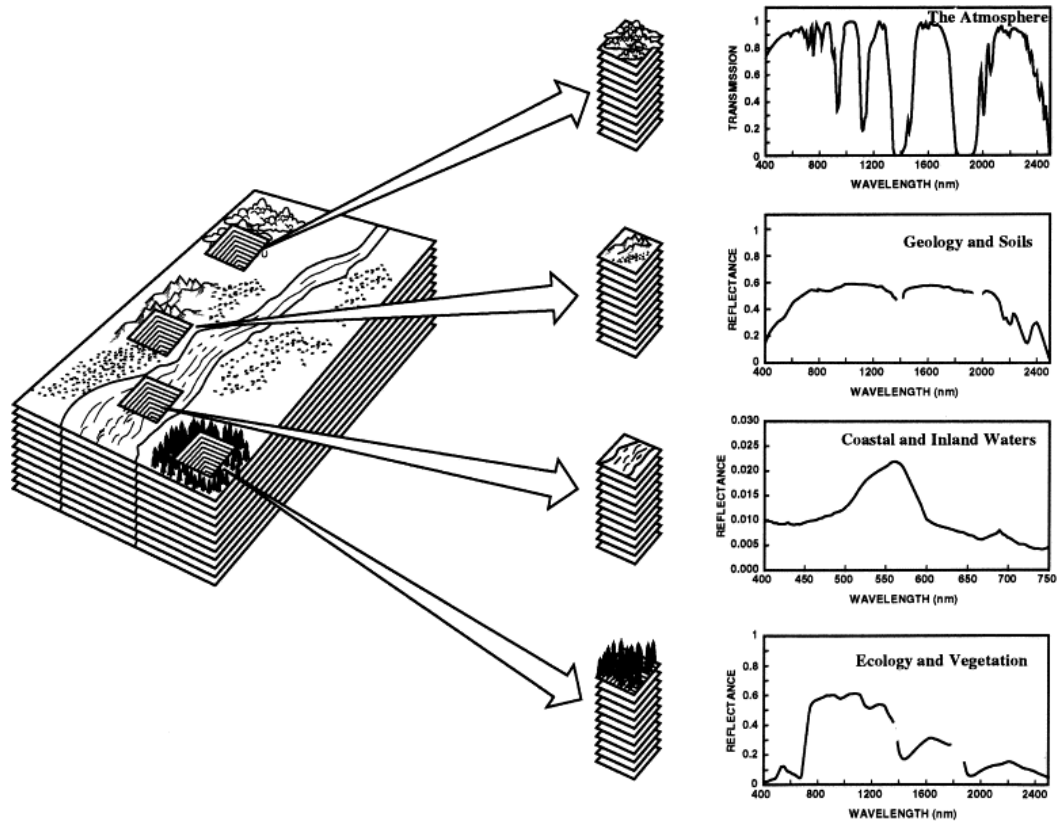
Figure 3.   From Green et al. (1998), this figure shows the concept behind imaging spectroscopy and how it measures a spectrum for each image component (pixel) in a satellite image.

1.   Electronic Processes

Electronic processes are the result of changes in energy states of electrons when they are emitted or absorbed by some material. The most common of these are related to the unfilled electron shells of transition elements such as Iron (Fe), also known as the Crystal Field Effect (Clark, 1999). For transition elements, energy levels are split if an atom is in the crystal field, allowing an electron to jump from a lower to higher energy state when an photon with enough energy to make up the difference between energy states is absorbed (Clark, 1999). Because the crystal field varies with the atomic structure of the material, the splitting energy will also vary causing spectral signatures unique to an individual material (Clark, 1999; Jensen, 2007). Other material specific electronic processes are associated with color centers, charge transfers, and conduction bands (Clark, 1999; Jensen, 2007). Charge transfers occur when there are inter-element

transitions in which electron movement is between ions or ions and ligands and in Fe, for example, are the reason for its red color. When electrons move amongst two different energy levels there is a gap in the band (band gap) represented by the difference in energy levels. These bands often show themselves in the visible range and causes colorations in some minerals. Color centers are a response to impurities and defects in the structure of the material and cause for example, the blue color in fluorite. They show up as absorption features because they use photon energy to gain electrons (Clark, 1999).

2. Vibrational Processes

Vibrational Processes are associated with the crystal lattice structure and the bonds within it and can be compared to a spring with a weight attached vibrating with fundamental frequencies and overtones (Clark, 1999; Jensen, 2007). Fundamental frequencies are the normal modes of vibrations; overtones are multiples of the fundamental frequency as well as different combinations of it (Clark, 1999; Jensen, 2007). Natural materials exhibiting these vibrational processes include phosphates, borates, carbonates, water and hydroxyl (Jensen, 2007). Vibration fundamental modes have traditionally been represented as ν_1, ν_2, ν_3 and overtones as $2\,\nu_1$, $3\,\nu_1$, $2\,\nu_2$ with combinations being represented as additions and subtractions of fundamentals (Clark, 1999).

3. Imagery Collection, Processing, and Analysis

a. Collection

The collection and analysis of these spectra allows one to identify such things as mineral and rock type in a given area remotely based on its unique absorption features. The current Hyperspectral Imagery (HSI) technology utilizes spatial resolution of 2–20 m, spectral resolution of 10–20 nm and a signal-to-noise (SNR) ratio that is greater than 500:1 for data collection (Kruse, 2012) On a mineral or rock surface, incident light (photons) can be absorbed, reflected/refracted, or passed through to other grains of a material. Reflected or refracted light is also called scattered light which can be directed toward a remote sensing sensor capable of measuring abundances and properties of some material within the sensors field of view (FOV) (Figure 4). When

8

analyzing imagery spectra, it is most useful to have the spectra in units of reflectance rather than radiance because radiance energy tends to be dominated by the solar spectrum (Roberts and Herold, 2004). Remote sensing primarily uses two different types of reflectance; directional-hemispherical reflectance and bidirectional reflectance collected commonly in the nadir (normal to the surface) viewing geometry. The differentiating factor between the two types of reflectance is that they are measured in the laboratory and in the field, respectively (Roberts and Herold, 2004).

Wavelength (µm) (1000–2600 nm)
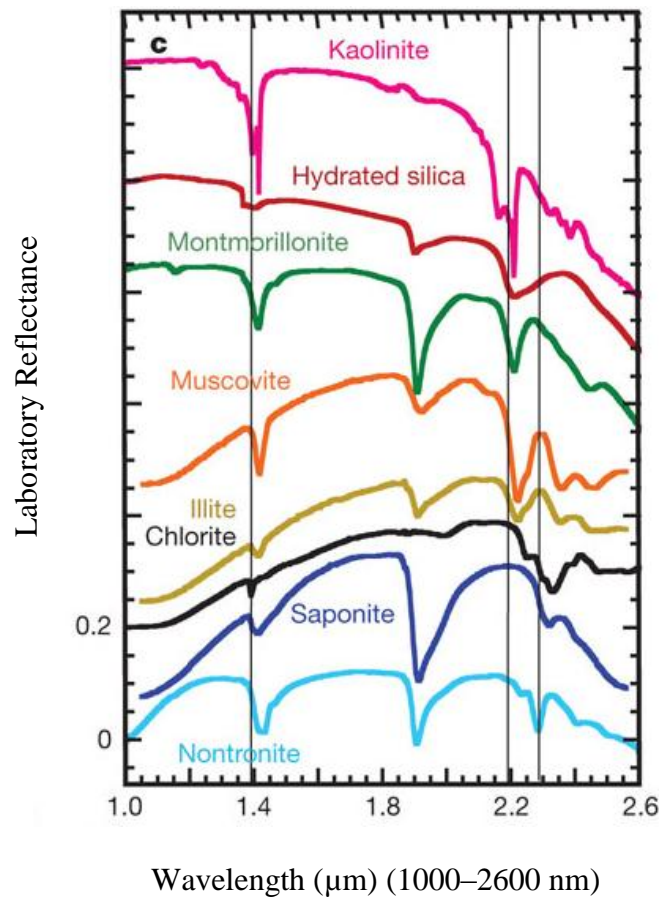
Figure 4.   This figure from Mustard et al (2008) shows the varying and somewhat unique absorption features for a variety of different minerals at the 1.4 and 2.2 micrometer (1400–2200 nm) wavelengths. These absorption features are related to the electronic and vibrational processes associated with the chemistry of the different materials (Goetz et al., 1985; Clark, 1999). Here, a number of processes and interactions come into play, which determines the amount of energy each type of material will emit, absorb, and scatter (Jensen, 2007)

b.   Processing

The image processing of hyperspectral data involves several steps. The most critical of these is the conversion of the spectrometer data into reflectance (Kruse et al., 2000).   Radiometric calibration is the method utilized in converting data to reflectance and does so by standardizing the collected signal via a series of gains and offsets that essentially divide each collected spectrum by the solar irradiance at the sensor; this step is a requirement for atmospheric correction during the image processing phase (Kruse et al., 2000; Roberts and Herold, 2004).   A method for checking the accuracy of the conversion is to compare it to wavelength ranges known to have atmospheric absorption features (Figure 5) to see if they are in the correct location after the conversion (Kruse et al., 2000). Atmospheric absorption bands are portions of the electromagnetic spectrum that are opaque to a sensor viewing from space so the collected signal is noisy in these regions.   These absorption bands are always at the same wavelength (Olsen, 2007) so one should be able to utilize them as an accuracy check as Kruse et al. (2000) suggests.
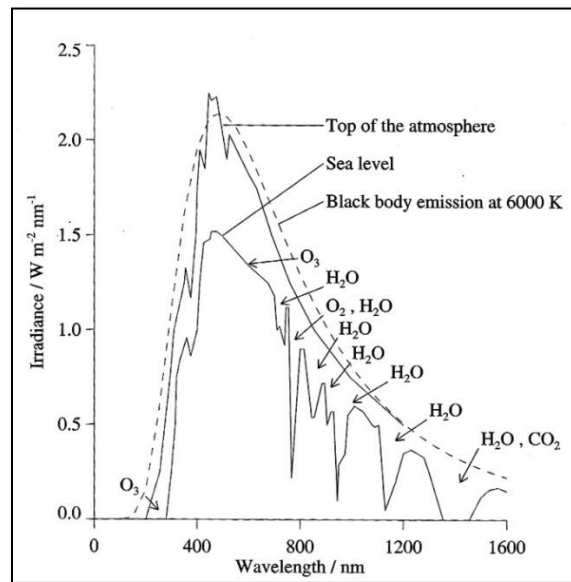
Figure 5.   This figure from the
http://lasp.colorado.edu/~bagenal/3720/CLASS5/5Spectroscopy.html
shows the regions of atmospheric absorption bands in the visible through
short wave infrared regions of the electromagnetic spectrum. The
atmospheric components responsible for a given absorption band are
labeled (Olsen, 2007).

10

After data have been converted to reflectance, they must then be atmospherically corrected to account for interactions with the atmosphere such as scattering and absorption by atmospheric gas and particulate material (Kruse et al., 2000). Atmospheric correction is a necessary step that allows for determining physical aspects of imaged materials and making inferences with the data during analysis (Kruse et al., 2000).

c. *Analysis Using Continuum Removal*

A continuum can be thought of as a mathematical means by which you can isolate a particular absorption feature of a spectrum and is related to the electronic and vibrational processes that occur within surface materials discussed earlier (Clark and Roush, 1984). The purpose of continuum removal is to rid the spectrum being analyzed of affects from other processes within the material or other materials in a mixture so characteristics of an individual feature can be better examined (Clark and Roush, 1984; Clark, 1999; Clark et al., 2003; Kruse, 2008). The continuum removal is done by estimating the other absorption processes using functions such as, but not limited to Gaussians and straight-line segments (Clark and Roush, 1984). The mathematical function for continuum removal, according to Clark and Roush (1984) is expressed as:

$$r(\lambda) = e^{(-k_1\bar{l}_1)}e^{(-k_2\bar{l}_2)}e^{(-k_3\bar{l}_3)} \tag{3}$$

where:

r is reflectance,

$k_1, \bar{l}_1$ are functions of the wavelength and represent absorption of some process of interest in the material,

$k_2, \bar{l}_2$ are absorption related to other processes in the mineral,

$k_3, \bar{l}_3$ are absorption related to other processes from other materials.

Continuum removal during spectral analysis is useful in both biological and mineralogical analysis. This method has been found to be successful in correlation of

biochemical components of plants to absorption feature depths in plant material (Curran et al., 2001; Kokaly and Clark, 1999; Mutanga et al., 2004; Noomen et al., 2006). Weber et al. (2008) and O'Neill (1994) were able to use the continuum removal method to discriminate biological crustal components of soils known as cryptobiotic crusts from bare soils and Clark and Roush (1984) as well as Kruse (1988) discuss the usefulness of continuum removal in mineral mixture analysis.

D.   RELEVANT MILITARY AND CIVILIAN APPLICATIONS OF IMAGING SPECTROSCOPY

Imaging spectroscopy has been used by the military for a number of purposes. One instance is in determining terrain trafficability (the capability of an area to bear traffic and permit continued movement of that traffic) by first identifying and then mapping surface compositions of an area (Kruse et al., 2000). While the hyperspectral data alone were not sufficient due to a lack of information on terrain such as slope or surface texture; when used in conjunction with digital elevation models (DEMs), synthetic aperture radar (SAR), or other datasets, hyperspectral imagery can be very useful (Kruse et al., 2000). The information that was provided by hyperspectral data in this study included composition and distribution of soils, vegetation, manmade materials, and drainage features (Kruse et al., 2000). Kruse et al. (2000) were then able to use this information to produce a trafficability product providing the consumer with information that is helpful in navigating through areas of potential risk; such as steep slopes with a principal constituent of clay that could potentially hinder movement (Kruse et al., 2000). A second example where hyperspectral imagery has been of use to the military is in the exploration of target and anomaly detection (Manolakis et al., 2003). Because hyperspectral imagery relies on data collected over a contiguous spectrum, unlike some traditionally used passive imaging systems, it can identify objects that are partially hidden from view and identify them by their spectral characteristics instead (Manolakis et al., 2003).

A study by Collins et al. (1997) provides an example of spectral characteristics being utilized to identify anomalies using SEBASS data in the long wave infrared regions (LWIR). Through the use of Hyperspectral imagery and principal component analysis,

Collins et al. (1997) was able to successfully use the characteristic spectrum of desert varnish to not only detect targets such as military vehicles and fox holes, but tank tracks on the desert varnish itself (Colins et al., 1997). Use of the differences in restrahlen emissivity between the desert varnish and other materials provided a useful visualization of vehicle traffic and target location (Figure 6) (Collins et al., 1997).
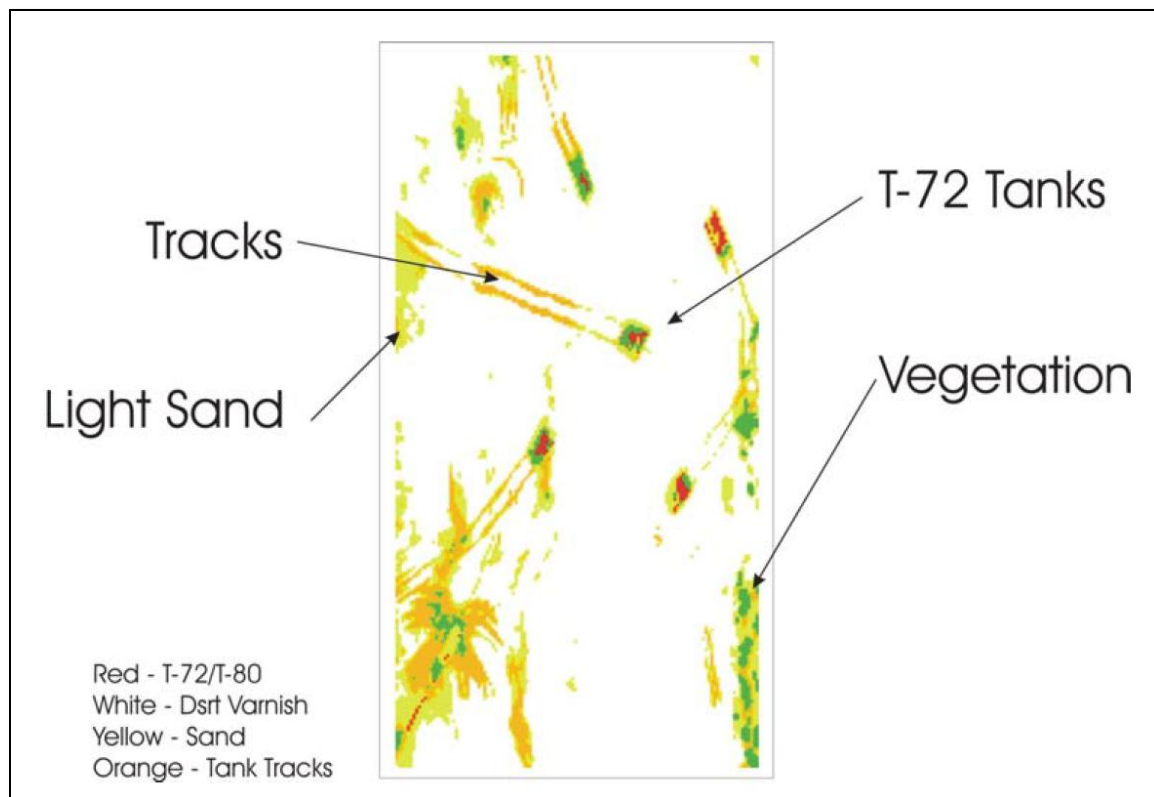
Figure 6. The above image from Collins et al. (1997) shows the results of using principal component analysis achieved using LWIR hyperspectral SEBASS data for their target detection and terrain classification study.

Hyperspectral imagery have also proved useful for several environmental applications. One in particular that applies to this research is the use of hyperspectral data to identify plant stress during a study conducted in 2004 (Smith et al., 2004). Observed spectral changes consisted of decreased reflectance in plants that were undergoing stress in the near infrared range between 0.72 and 0.73 μm (720 and 730 nm) (Smith et al., 2004). Characteristic changes in reflectance related to stress can be seen in

Figure 7 from the study by Smith et al. (2004). The stress of the plants was then successfully utilized to find where gas was leaking from pipe lines underground because gas injection into the soil caused a feature of discoloration known as chlorosis in addition to changes in chlorophyll *A* concentration of gassed grasses (Smith et al., 2004).
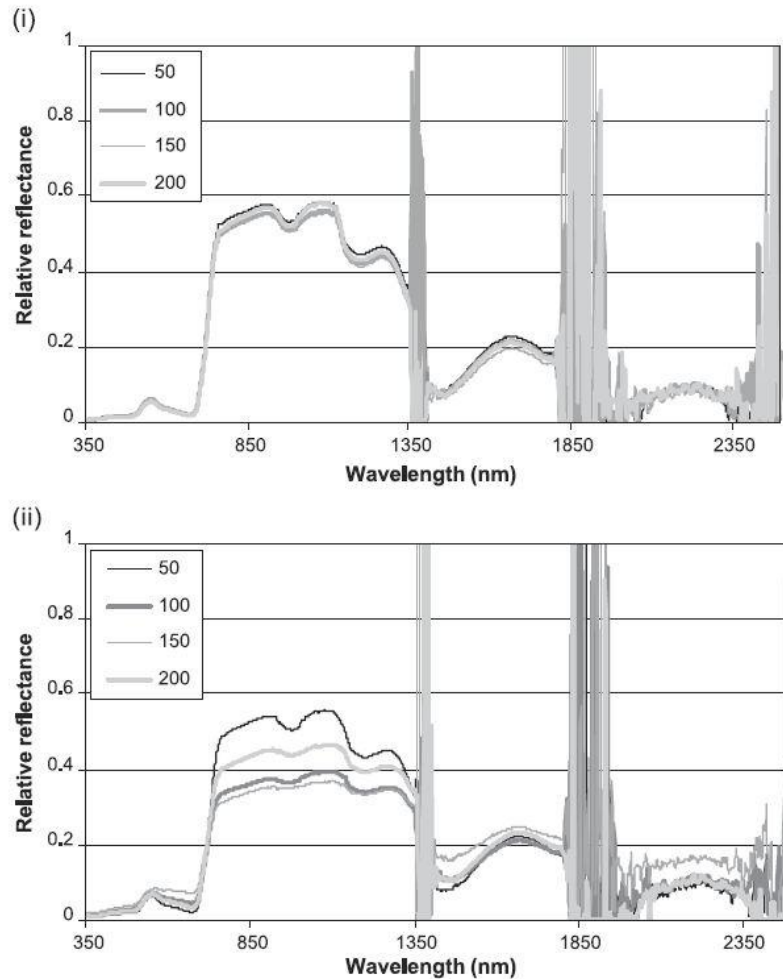
Figure 7.   The above figure is from Smith et al. (2004), and shows the spectrum of control grass (i) compared to early-gassed grass (ii) at varying distances from a gas source along a transect (in meters). Looking at the region between 350 and 850 nm (0.35–0.85 micrometers) in (i), you can see that reflectance does not vary much along the transect. Contrastingly, the change in reflectance varies significantly with distance from the gas source due to varying levels of plant stress.

The above studies illustrate the capability of hyperspectral data in characterizing target materials based on components not visible to the naked eye for multiple purposes.

14

These purposes include, but are not limited to locating a target itself, the ability to maneuver within the space the target material resides in, or finding hidden targets via the disruption they cause to some ecosystem constituent (Kruse et al., 2000; Manolakis et al., 2003; Smith et al., 2004). It seems a likely assumption that hyperspectral data can characterize changes in soil properties based on those reflectance changes in both biological and chemical components (Smith et al., 2004). It also seems a likely assumption that hyperspectral data can be used to track areas supporting anthropogenic activities by identifying alterations of characteristic properties caused by some surface disturbance (Prose, 1985).

THIS PAGE INTENTIONALLY LEFT BLANK

III. DESERT ECOSYSTEM CHARACTERISTICS

A. DESERTS AND THEIR DISTRIBUTION

1. Humans and the Arid Environment

By definition, deserts are arid or semi-arid regions where rainfall is the limiting factor for productivity and/or is unpredictable to the point that growing crops is not possible (Whitford, 2002). Biological constituents of a desert are often considered to be living at or near their threshold of tolerance for a given environmental or ecological condition; resulting in local extinctions of some species when they are stressed beyond their ability to cope (Whitford, 2002). Desert ecosystems have been found to be so sensitive that constant disturbances have been known to cause change in both the structure and function within the region itself and extending to surrounding ecosystems (Webb et al., 2009). One example of how anthropogenic disturbances alter desert ecosystems is the distribution of plant communities and the close correlation of human impacts with increased rates of non-native plant invasions (Webb et al., 2009). Other changes are decreases in soil conductivity (electricity) because of impact-related decreases in soil porosity. These alterations lead to higher erosion rates and wind transporting of soil materials (Prose, 1985). Because structural characteristics of soils affect all processes in the desert environment, links can be established between bio-chemical interactions and human-related impacts (Prose, 1985; Whitford, 2002) based on changes in reflectance within hyperspectral imagery (Smith et al., 2004).

2. Desert Biomes

According to Whitford (2002), desert biomes cover roughly one-third of the Earth's surface, occurring in areas with less than 50 cm/year of rainfall. Figures 8 and 9 illustrate a distribution of desert regions and correlating soil types, respectively.

.
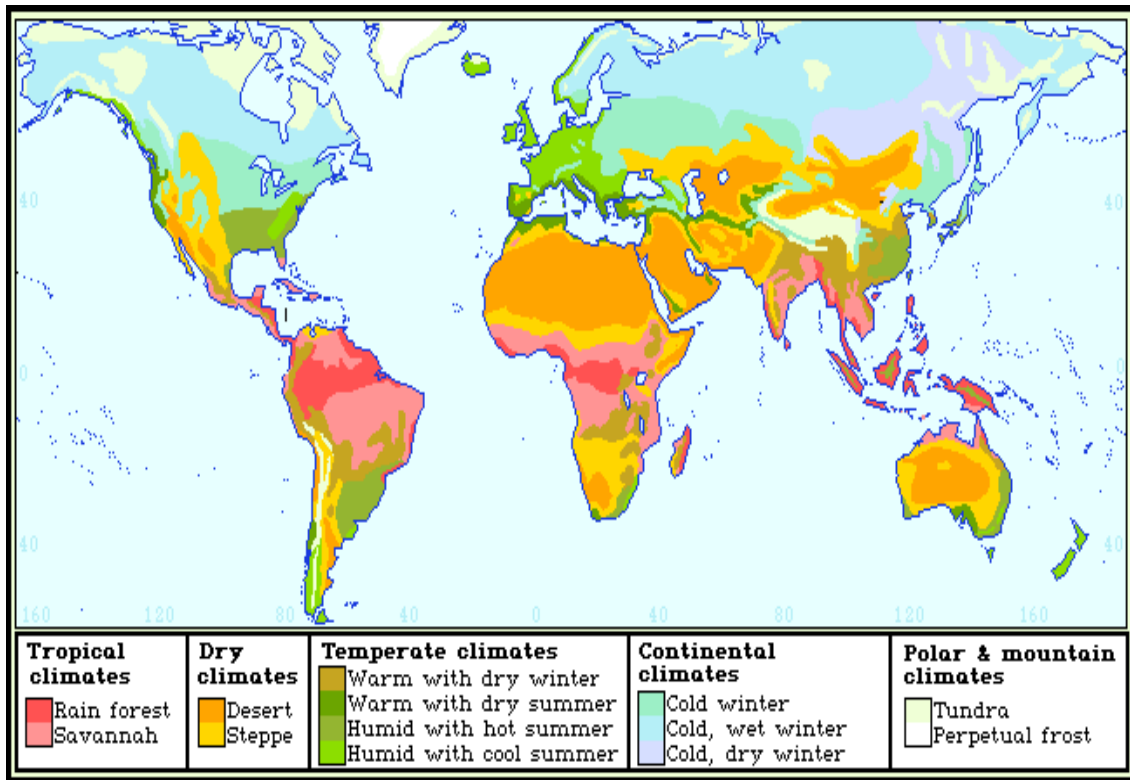
Figure 8.   In this image from http://serc.carleton.edu/eslabs/weather/4a.html the distribution of global biomes is shown. The areas that are colored orange and yellow comprise the Desert and Steppe ecosystems of the world that constitute the hot and dry, coastal, and semiarid desert regions. Cold deserts would be included in certain portions of the blue regions on the map.

Desert biomes fall under four major classifications: hot and dry, semiarid, coastal, and cold (Allaby et al., 2011; McKinney et al., 2013; Whitford, 2002). Examples of hot and dry deserts include the Chihuahuan, Sonoran, Mojave and Great Basin in the United States. Examples outside of the United States include the Southern Asian Realm, Neotropical of South and Central America, the Ethiopian of Africa and the Australian desert. These deserts are warm throughout the year to very hot over the summer months. Rainfall is scarce in these regions and when it does occur it is often in bursts after long dry spells. Common plants are low growing shrubs, trees, and cacti. Soils in these regions are course-textured and gravely, exhibit good drainage and have no subsurface water (Whitford, 2002). Semiarid desert regions of the United States include the

18

sagebrush of Utah, Montana, and the Great Basin. This biome can also be found in the Nearctic realm of North America, Newfoundland, Greenland, Russia, Europe, and northern Asia. Similar to hot and dry deserts, rainfall in these regions is low in the winter and summers are long and dry. Plants here consist of spiny and glossy leafed varieties. These regions differ in that they have cool nights which allow for condensation of dew providing more water to these regions than hot and dry deserts. Soils here range from sandy fines to larger fragmented rock, sand, or gravel. Mountain slopes will typically have shallow soils with good drainage while the lower slopes characteristically have well-drained soils. Both cases do not contain sub-surface water (Allaby et al., 2011; Lammers, 1991; Whitford, 2002). Coastal deserts occur in moderately cool to warm regions and are characteristic of the Nearctic and Neotropical realm with the Atacama Desert located in Chile being a primary example. They tend to have cool winters and somewhat long, warm summers. Average rainfall in these deserts is generally 8–13 cm but places such as the Atacama can see 1.5 cm or less. Soils here are generally fines and gravels with some salt content. The soil is porous with good drainage (Allaby et al., 2011; Warhol, 2007). Lastly cold Deserts can be found in regions of the Antarctic, Greenland, and the Nearctic realm. These deserts are known for cold winters with high overall rainfall during winter months. They also receive snowfall and some rain during the short, moderately warm summer months. Winters are quite long, cold, and receive considerable snowfall. Annual precipitation ranges from 15–26 cm but can reach a maximum of 46 cm and minimum of 9 cm. Soils consist of heavy silts with high extractable mineral content often coinciding with porous soil of good drainage allowing for mineral leaching (Jonasson et al., 2000; Moore, 1978).
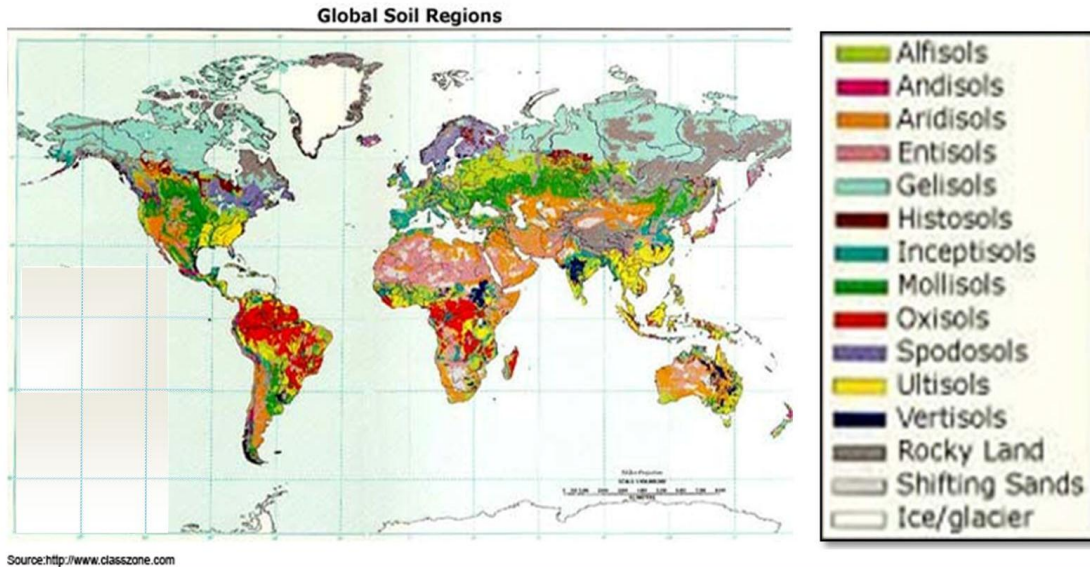
Figure 9.   The above figure is a map of world soil types and their distribution adapted
              from the http://www.cals.uidaho.edu/soilorders/i/worldorders.jpg (2012).
              Notice that the primary soil types associated with the arid regions in Figure
              7 are Aridisols (orange), and Entisols (pink) to some extent.

B.   CHEMICAL AND BIOLOGICAL SOIL COMPONENTS

1.   Soils

Aridisols are the predominant soil type associated with the desert environment
(Whitford, 2002). Figure 9 illustrates different soils throughout the world along with their
respective regions, and Figure 10 shows the percentage distribution of aridosols in the
United States. Aridosols are $CaCO_3$ containing soils generally found in arid regions that
experience some subsurface horizon development. Characteristically, these soils are dry
through most of the year with limited leaching (Balba, 1995; Whitford, 2002).

Subsurface horizons have accumulations of clays, calcium carbonate, silica salts,
and gypsum in some cases, though gypsum and calcium carbonate tend to leach from
soils in most climate types (Balba, 1995). The properties of the subsurface soil horizons
are important to know because variability in soil materials is detectable through Imaging
Spectrometry (Clark, 1999; Kruse et al., 2000) and their presence may
tell something about activities in the area (Webb et al., 2009). Other soil types also found

in desert regions include argids, orthids, mollisols, entisols, and shrink swell soils also known as cracking clays (Whitford, 2002).

The structure and processes that occur within desert regions can be directly linked to soil properties and therefore make it possible to link changes in those properties to alterations in ecosystem functions (Prose, 1985; Whitford, 2002). Because soils are a product of geology, geomorphology, and climate it is possible to make inferences as to what types of soil components may be present based on local geologic, geomorphologic and climatologic information (Whitford, 2002; Lammers, 1991). These similarities should also allow for use of endmembers from a geographically different yet geologically similar area to be used to study surface disturbances in different arid regions of the world (Whitford, 2002; Lammers, 1991). Soils also play a key role in nutrient availability and nutrient cycling critical to survival of biologic soil components such as cryptobiotic soil crusts (BSCs) (Whitford, 2002; Bowker et al., 2005). It is a reasonable assumption that biological soil components exhibiting signs of stress can yield information (Smith et al., 2004) on anthropogenic activities causing surface disturbances; because these impacts change ecosystem functions and nutrient delivery systems (Bowker et al., 2005; Evans et al., 1999; Prose, 1985) within and around an area (Webb et al., 2009).
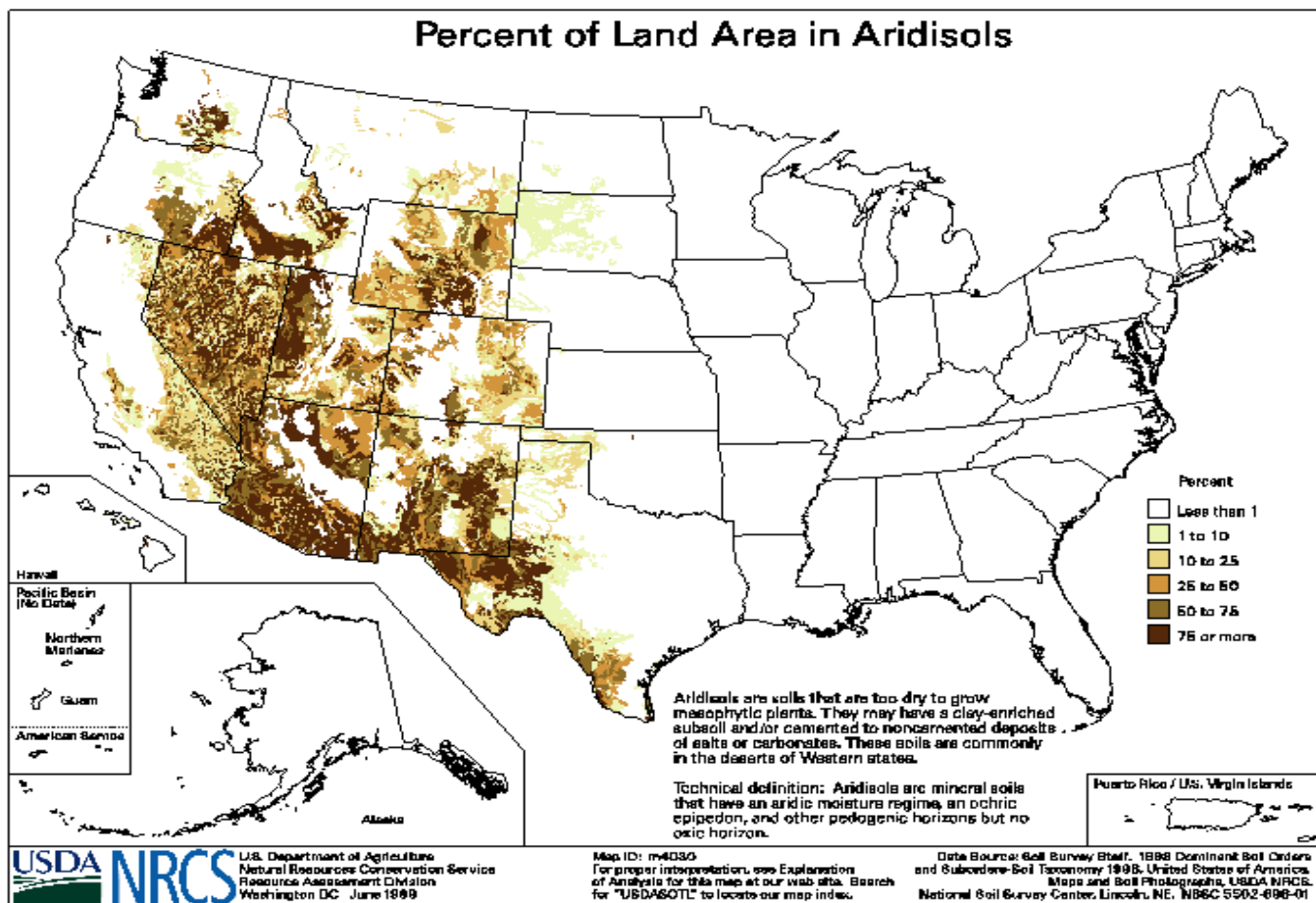
Figure 10.   The above figure from the http://www.cals.uidaho.edu/soilorders/percentarid.gif shows the distribution of Aridisols in the US and includes areas of the ASD collection sites and AVIRIS imaged areas. Knowing what soils are present in an area will be helpful in making predictions about how soil properties will respond to surface disturbances, which can in turn aid in tracking those disturbances consistently (Lammers, 1991; Whitford, 2002).

2.   Biological Soil Crusts (BSCs)

Biological soil crusts (BSCs) are prevalent in two of the areas used for this study; both the Owens/Death Valley collection area and Canyonlands National Park (see Section IV below). Figure 11 shows a photograph of the predominant species in the Owens Valley collection site compared to that of Canyonlands National Park. Also known as cryptobiotic soils, BSCs are communities of sessile organisms that include bryophytes, lichens, eukaryotic algae, cyanobacteria, free-living fungi, and bacteria (Bowker et al, 2005). Found on all continents, and in most habitats, BSCs are so prevalent, there are few areas in the world that can be considered BSC free (Bowker et al., 2005; Johnston, 1997).
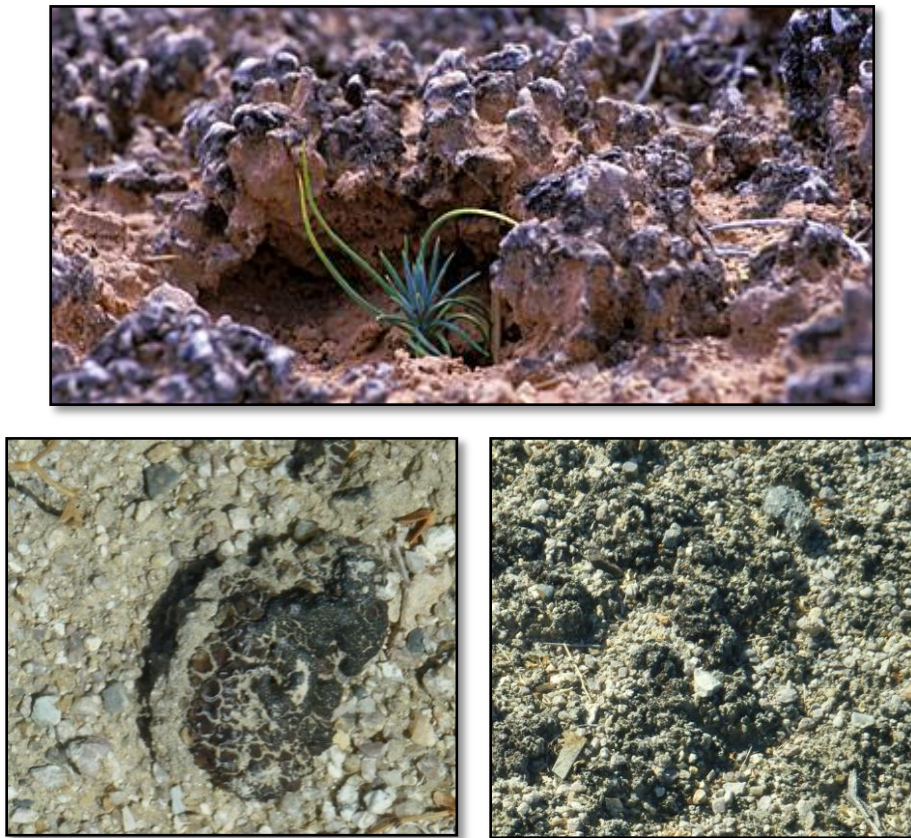
Figure 11.   Photograph of BSCs taken at the Owens/Death Valley collection (bottom two) site compared to those of Canyonlands National park (top photograph) (http://www.nps.gov/cany/naturescience/images/SoilCrust_CloseUp.jpg , Jessica Howard)

BSCs are characteristically located on the surfaces of mineral soils and perform key ecosystem functions in a variety of habitats worldwide and cover ~40% of the land surface up to 10cm thick in arid environments (Bowker et al., 2005). BSCs have many names, cyptogamic, cryptobiotic, microphytic, though all imply some commonality. The difference between cryptobiotic crusts and chemical/physical crusts is the fact that BSCs are formed by living organisms and their by-products while chemical/physical crusts (e.g., salt crusts) are inorganic (Johnston, 1997). These soils contribute to carbon and nitrogen fixation as well as affecting soil moisture and nutrient levels (Bowker et al., 2005; Evans and Belnap, 1999). In fact, soil texture, pH, and conductivity all play a role in whether crusts will be in an area or not (Johnston, 1997; Whitford, 2002). As Prose pointed out in his study, surface disturbances change intrinsic properties of the soil and can therefore be exploited by hyperspectral imagery (Clark, 1999; Prose, 1985). Davis (2007) made similar determinations about soil water content and vegetation health in his study on helicopter brown out. It was found that the amount of chlorophyll present in the soil served as an indication of whether or not the soil was barren (Davis, 2007). It is this premise that chlorophyll concentrations can be related to soil moisture and vegetation health that should allow for detection, using imaging spectrometry, on a sub pixel level of impact-related surface disturbance; since BSCs are typically at the top 1–4 mm of soil (the soil air interface) (Davis, 2007; Johnston, 1997; Weber et al., 2008). Soil-air interface processes include soil stability and erosion, atmospheric N-fixation, nutrient contributions, soil-plant water relations, infiltration, seedling germination, and plant growth (Asner and Heidebrecht, 2002; Johnston, 1997; Webb et al., 2009; Whitford, 2002).

In non-disturbed regions, correlation between soil properties and BSCs can be made (Whitford, 2002). One correlation is water availability (Weber et al., 2008). Disturbances generated by impact decrease water infiltration rates in soils and can register as stress in a biological soil component, further supporting the idea that BSCs can be useful in adversary tracking (Prose, 1985; Whitford, 2002). Soil nutrients such as N, P, K, Mg, Fe, Mn, Zn, Cu, and others are also likely factors that affect the abundance of cryptobiotic soils making them useful in detection of IED supply lines (Smith et al.,

2004), especially in cases where materials are spilled. Adding Nitrogen to soil has demonstrated a retarding effect on natural nitrogen fixation by soil organisms (Asner and Heidebrecht, 2002; Johnston, 1997), however, studies on the relationship between nutrient availability and BSC abundance are limited (Bowker et al., 2005). The study by Bowker et al. (2005) had data supporting the correlation between BSC abundance and micronutrient availability. They found that in particular, Mn and Zn, had a strong relationship to the abundance of BSCs which could be useful in determining where soil crusts are located based on spectral signatures of soil composition. Overall, components of BSCs were positively correlated with nutrient availability. Because it is thought that BSCs are useful in monitoring the condition of various rangelands and determining when restoration efforts are successful, it makes sense that they can also be useful as indicators of when ecosystems are becoming off balance, and if there is an anthropogenic impact occurring in their region of growth causing the balance shift to occur (Haboudane et al., 2008; Webb et al., 2009).

According to Evans et al. (1999) cryptobiotic crusts in arid environments are especially susceptible to degradation resulting from land use changes and other impacts from both anthropogenic and natural causes. Direct crustal damage is most often in the form of trampling because it breaks up sheaths and filaments which hold crustal soils together (Johnston, 1997). If soil properties can be altered with even minimal impacts/disturbances (Prose, 1985), then the loss of permeability to water, changes in nutrient availability, and structural breakdown-related stresses should also register on a spectral level (Smith et al., 2004; Weber et al., 2008). Studies have demonstrated that activities related to the military, overland recreational vehicles (ORVs) such as dirt bikes/all-terrain vehicles, hiking, biking, and livestock grazing place a heavy toll on BSCs because of unsuccessful adaptations to compressional disturbances such as trampling (Johnston, 1997). The organisms comprising the crust have a different range of sensitivities with the dominant species being partially affected/determined by microclimate. In particular an absorption feature related to chlorophyll *A* at 680 nm differentiates the BSCs from bare soil (O'Neill, 1994; Weber et al., 2008). Since this feature has shown responses to the addition of water in a study done by O'Neill (1994) it

25

seems a likely candidate for analysis (O'Neill, 1994; Weber et al., 2008). Similarly to soils, predictions based on climate, geology, and geomorphology of the region should also be possible with these biological soil components (Whitford, 2002).

IV.   STUDY SITES

The focus area of this study is in an area around Canyonlands National Park, covering areas in parts of Grand and San Juan Counties, Utah (Figure 12). Geology units in the area range from 570 million years to about 80 million years old. The area was relatively low and flat until around 11 million years ago when the Colorado Plateau began to uplift due to a laccolithic igneous intrusion (Lammers, 1991). Elevation ranges from 1,219.2 m (4,000 ft) to 3962.4 m (13000 ft) with the higher elevations seeing nine different periods of glaciations (Lammers, 1991). Major natural resources here consist of scenery, potash, copper, gold, silver, uranium, natural gas, oil, vegetation, soil, and surface and ground water. The climate of the area is highly variable due to drastic changes in relief. Precipitation can range from less than 8 inches to 30 inches annually or more with average annual snowfall consisting of 20 to 70 inches on the plateau (Lammers, 1991).
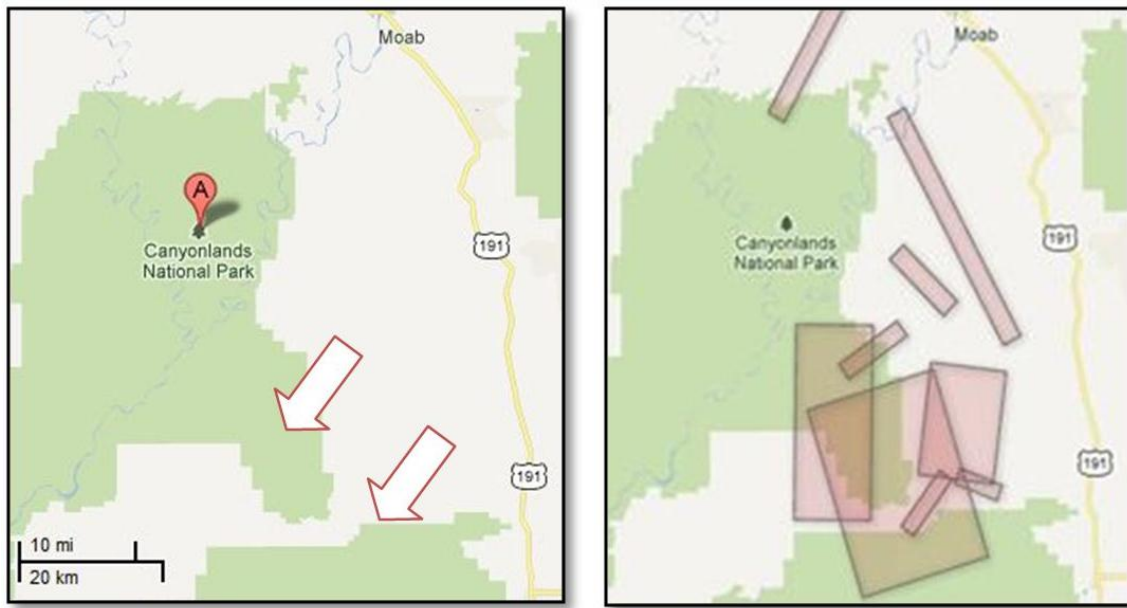
Figure 12.   This figure adapted from Google maps and from the JPL AVIRIS website shows the primary study locations marked by the white arrows, and the available AVIRIS flight lines (red boxes) for the area.

The soil distribution of the Canyonlands study area is depicted in Figure 13 and includes some information on the parent material as well as the geomorphology of the area. Overall the soil types are consistent with the nature of those of the ASD collection sites in Mono Basin and Mazourka Canyon. Characteristics of all sites include igneous and sedimentary soil origins (Lammers, 1991; Tallyn, 1996) with sandstone, shale, diorite, limestone, and granite being the primary parent materials. Soils of both locations show a history of being influenced by Aeolian, glacial, lake, and river presence with most soils exhibiting well drained characteristics though some units are poorly drained soils (Lammers, 1991; Tallyn, 1996). Both the Utah and California sites are used primarily for rangeland, wildlife habitat, watershed, recreation, along with some cropland use and urbanization (Lammers, 1991; Tallyn, 1996).

The area of collection for the Mono Basin and Owens and Death Valley areas consisted of Panum Crater in the vicinity of Mono Lake, and Mazourka Canyon near Independence, Ca. (Figure 14, Inset B). Figure 14, inset C shows the author getting the spectrometer ready for collection at the Panum Crater location. The geology of Mono Basin includes Mono Lake, the remnant of Pleistocene Lake Russell, which has twice the salinity of the ocean (Figure 15, inset A). The most recent volcanic eruption in this area was roughly 300 years ago with highly silicic lava types of dacite and rhyolite; obsidian is also present in the dome (Sharp and Glazner, 1997; Tallyn, 1996). Panum Crater had eruption events between 1325 and 1365 CE and was the youngest vent of the Mono Craters eruptions and exhibited both pyroclastic (explosive) and phreatic (steam) type eruptions (Bursik and Sieh, 1989; Sieh and Bursik, 1986). The ring around the dome of the volcano is the result of a strombolian type of eruption (Sieh and Bursik, 1986; Sharp and Glazner, 1997). Rocks underlying Panum Crater consist of the granitic and metamorphic batholith associated with the Sierra Nevada. On top of this sits a mixture of basaltic to rhyolitic volcanic rocks that are from 3.5 million years to less than 760,000 years of age. Also present are glacial deposits, gravel sediment, and rhyolitic glass and pumice formed domes (Sieh and Bursik, 1986).

SOIL LEGEND

DOMINANTLY WELL DRAINED AND SOMEWHAT EXCESSIVELY DRAINED, NEARLY LEVEL TO MODERATELY STEEP SOILS ON LOW BENCHES, TERRACES, CUESTAS, AND VALLEYS IN AN ARID CLIMATIC ZONE

1 ROCK OUTCROP-MOENKOPIE: Rock outcrop, and shallow, well drained, gently sloping to strongly sloping soils that formed in residuum derived from sandstone; on low benches and cuestas

2 MOENKOPIE-ROCK OUTCROP-HOSKINNINI: Shallow, well drained, nearly level to moderately steep soils that formed in residuum derived from sandstone and limestone, and Rock outcrop; on low benches and cuestas

3 THOROUGHFARE-SHEPPARD-NAKAI: Very deep, well drained and somewhat excessively drained, nearly level and gently sloping soils that formed in alluvium and eolian deposits derived from sandstone and shale; on valley floors and low benches

DOMINANTLY WELL DRAINED, GENTLY SLOPING TO EXTREMELY STEEP SOILS ON BENCHES, CUESTAS, MESAS, ESCARPMENTS, AND CANYON WALLS IN A SEMIARID CLIMATIC ZONE

4 USTIC TORRIORTHENTS-LITHIC TORRIORTHENTS-ROCK OUTCROP: Shallow to very deep, strongly sloping to extremely steep soils that formed in colluvium and residuum derived from sedimentary rock, and Rock outcrop; on escarpments and canyon walls

5 ROCK OUTCROP-RIZNO, DRY-MIDO: Rock outcrop, and shallow and very deep, gently sloping to steep soils that formed in residuum and eolian deposits derived from sandstone and shale; on escarpments, mesas, benches, and cuestas

DOMINANTLY WELL DRAINED, GENTLY SLOPING TO MODERATELY STEEP SOILS ON BENCHES, CUESTAS, FANS, MESAS, ALLUVIAL BOTTOMS, STREAM TERRACES, AND VALLEY FLOORS IN A SEMIARID CLIMATIC ZONE

6 BEGAY-MOAB-REDBANK: Very deep, gently sloping to moderately steep soils that formed in alluvium and eolian deposits derived from sandstone and diorite; on benches, cuestas, alluvial fans, alluvial bottoms, stream terraces, and valley floors

7 RIZNO, DRY-ROCK OUTCROP: Shallow, gently sloping to strongly sloping soils that formed in eolian deposits and residuum derived dominantly from sandstone, shale, and Rock outcrop; on benches, cuestas, and mesas

DOMINANTLY WELL DRAINED, GENTLY SLOPING TO VERY STEEP SOILS ON UPLAND BENCHES, LANDSLIDES, CUESTAS, HILLSIDES, AND ESCARPMENTS IN A DRY, SUBHUMID CLIMATIC ZONE

8 CAHONA-BEGAY-HAGERMAN: Moderately deep and very deep, gently sloping soils that formed in eolian deposits derived from sandstone; on upland benches and cuestas

9 RIZNO-ROCK OUTCROP: Shallow, gently sloping to moderately steep soils that formed in residuum and eolian deposits derived from sandstone and shale, and Rock outcrop; on upland benches and cuestas

10 USTIC TORRIORTHENTS-USTOLLIC CALCIORTHIDS-USTOLLIC HAPLARGIDS: Moderately deep to very deep, strongly sloping to very steep soils that formed in residuum and colluvium derived from shale and sandstone; on hillsides, landslides, and escarpments

DOMINANTLY WELL DRAINED, GENTLY SLOPING TO VERY STEEP SOILS ON HIGH BENCHES, CUESTAS, FANS, LANDSLIDES, AND ESCARPMENTS IN MOIST SUBHUMID AND HUMID CLIMATIC ZONES

11 HERM-FALCON-WAAS: Shallow and very deep, gently sloping to moderately steep soils that formed in alluvium, residuum, colluvium, and eolian deposits derived from igneous and sedimentary rock; on high benches, cuestas, fans, and landslides

12 FALCON-HERM-TOONE: Shallow and very deep, moderately steep to very steep soils that formed in residuum, colluvium, and alluvium derived from sedimentary rock and diorite, and Rock outcrop; on landslides and escarpments

DOMINANTLY WELL DRAINED, GENTLY SLOPING TO VERY STEEP SOILS ON HIGH MOUNTAINSIDES, FANS, MORAINES, LANDSLIDES, VALLEY TRAINS, ARETES, AND CIRQUE BASINS IN A HUMID CLIMATIC ZONE

13 FLYGARE-SKYLICK-TOONE: Very deep, gently sloping to steep soils that formed in colluvium, glacial till, and alluvium derived from diorite, shale, and sandstone; on high mountainsides, fans, and landslides

14 BROAD CANYON-NAMON-LEIGHCAN: Very deep, strongly sloping to very steep soils that formed in colluvium and glacial till derived from diorite; on high mountainsides, moraines, and valley trains

15 RUBBLE LAND-LEIGHCAN-MEREDITH: Rubble land, and very deep, steep to very steep soils that formed in colluvium derived from diorite; on high mountainsides and aretes and in cirque basins

Compiled 1989
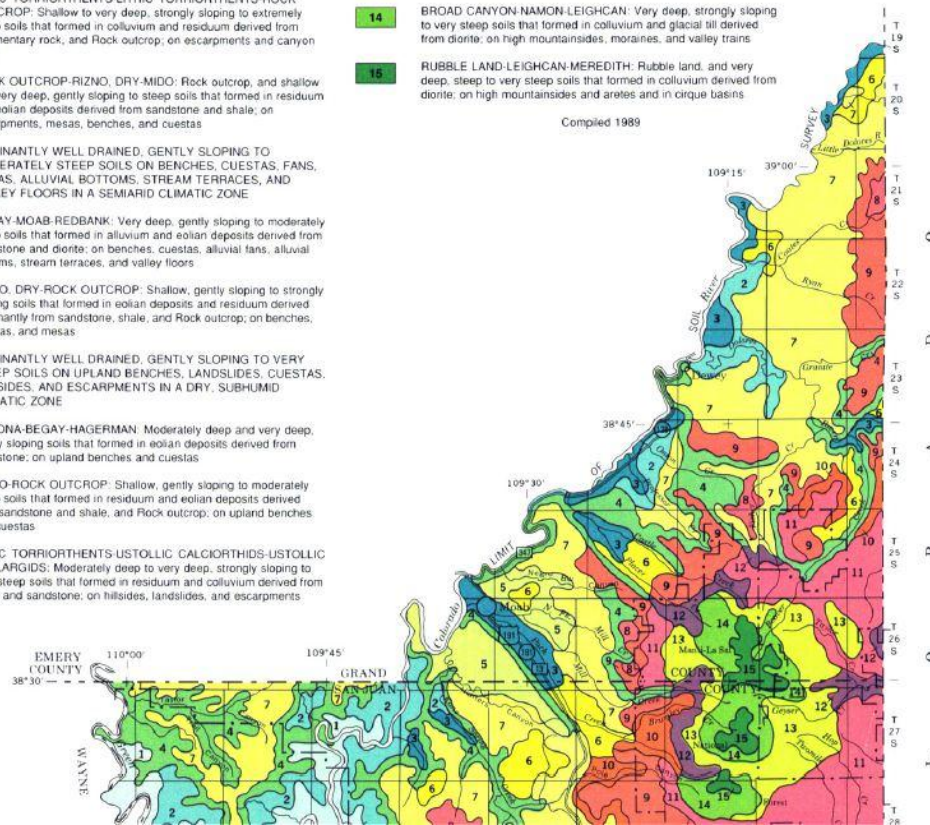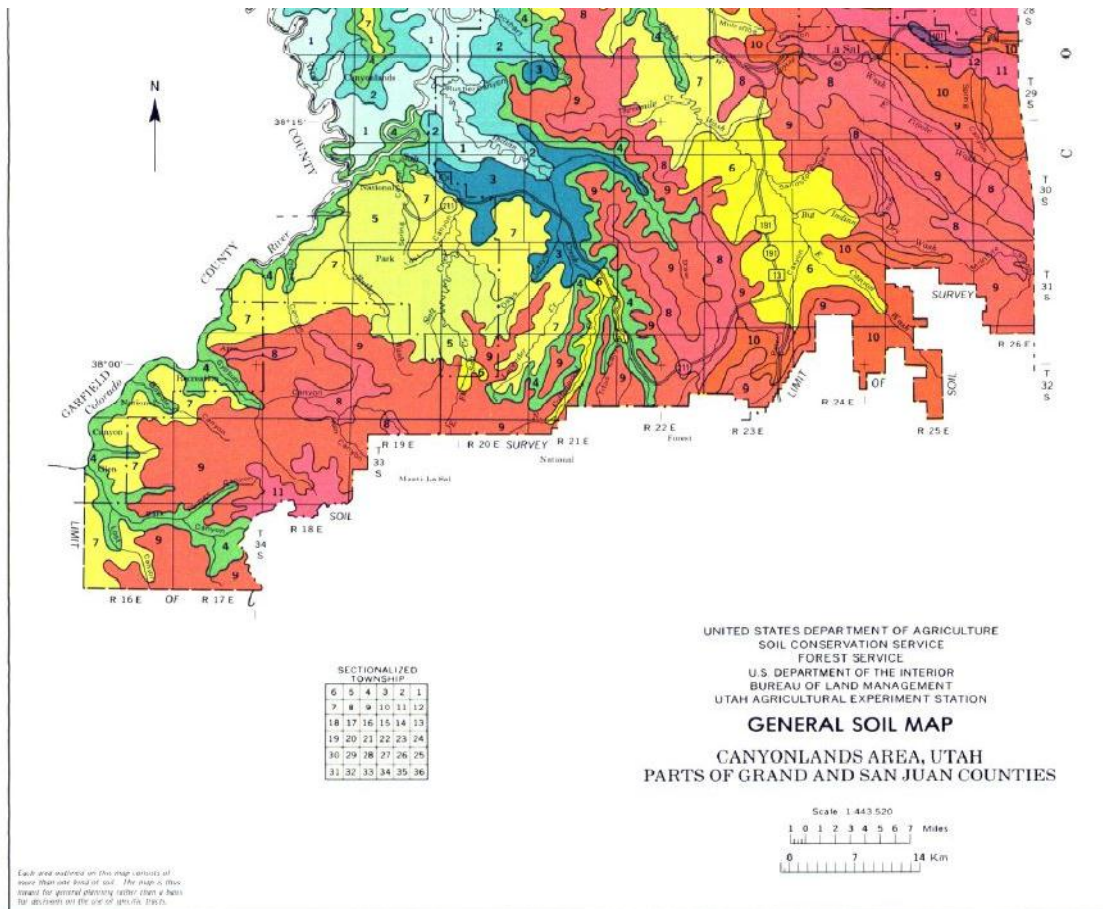
Figure 13.   This figure illustrates the soil type and distribution of the Canyonlands
National Park study site (Lammers, 1991).

Mazourka Canyon of the Inyo Mountains between Owens Valley and Death
Valley is the second collection area (Figure 14, inset C). The geology of this region
(Figure 15, inset B) consists of a continuous sequence of limestone roughly 457.2 m
(1500 ft) thick (Merriam, 1973).   Other components of the limestone structure in
Mazourka Canyon include calcareous siltstone, black chert, and gray chert (Merriam,
1973). Mazourka Canyon is part of the Inyo Mountains which once were part of the
North Americas western continental shelf (Stone et al., 2009). The substrate is the result
of shallow-water sediments being uplifted during the mid to late Paleozoic era
(570–240 mya). Once on the continental shelf, the marine sediments went through several
periods of subsidence and uplift related to thrust faulting (Stevens and Stone, 2007; Stone
and Stevens, 1998; Stone et al., 2009).

Figure 14.   Inset A is the Mono Lake area collect showing the location of Panum Crater with a blowup image of the crater area. Inset B shows the Independence, California area with a blow up image of the Mazourka Canyon collect site (adapted from Google maps). C shows the author getting ready for collection using the ASD spectrometer at Panum Crater (Nathan Stuart).

Following the uplift that occurred during the Paleozoic, the Mesozoic Era (240–65 mya) resulted in the recession of ocean waters, during this time volcanism and volcanically generated sedimentation from the Inyo Mountains Volcanic Complex began covering the newly dried land (Dunne and Walker 1993; Dunne et al., 1998; Stone et al., 2009). The most recent activity in the formation of the Inyo Mountains has been uplift related to basaltic volcanic activity associated with Basin and Range extension throughout the Cenozoic (65 mya-present) (Snow and Wernicke, 2000; Stone et al., 2009).
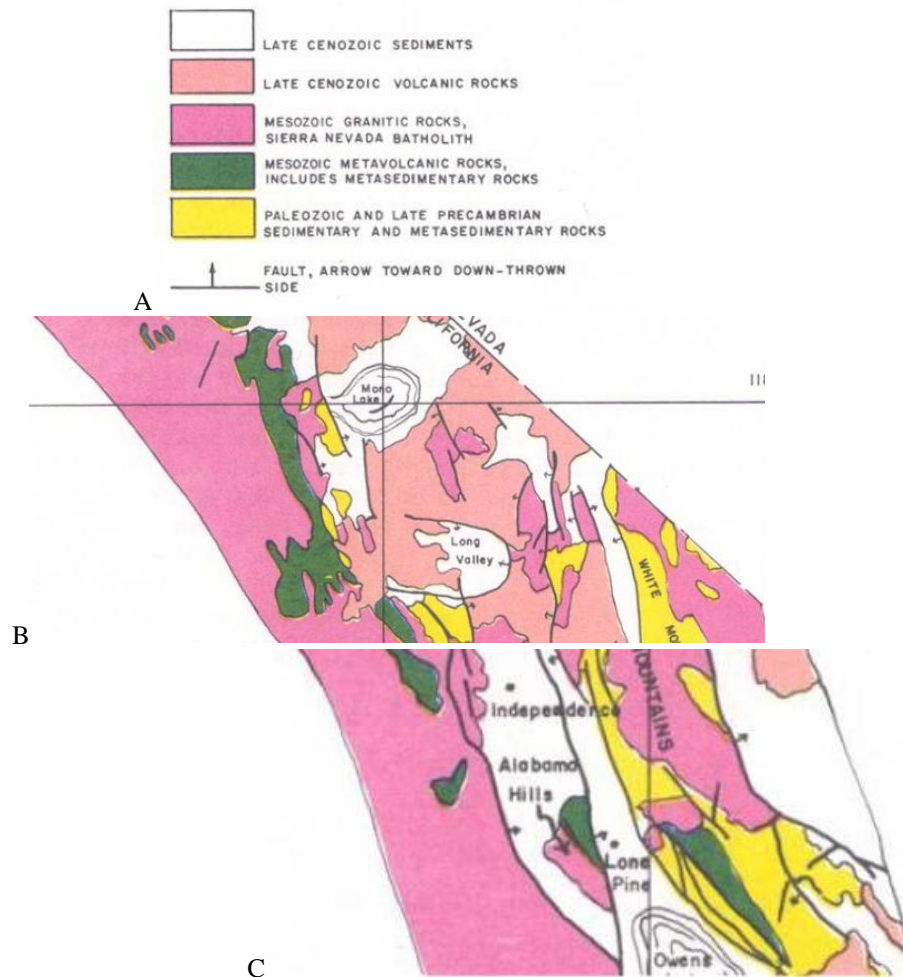
Figure 15.   A shows the key for the Mono basin and Owens/Death Valley collection areas, B shows the Mono Lake area, and C shows the Independence/Mazourka Canyon area. Knowing the geology of an area is helpful in predicting what kind of soils will be present, allowing for predictability in disturbance related changes of properties (FromTallyn, 1996).

V.   DATA AND METHODS

A.   DATA

Airborne imagery data were collected by the Airborne visible/Infrared Imaging Spectrometer (AVIRIS) system for the Canyonlands National Park area in Utah during 2011. AVIRIS utilizes a whisk-broom imaging method collecting high resolution spectra over the 0.4–2.5 micrometer (400–2500 nm) wavelength range (Green et al., 1998). Through the employment of 224 contiguous spectral channels set at 10 nm intervals over the breadth of the spectrum, AVIRIS is able to measure detailed upwelling radiance of surface materials. These measurements can then be used for determination of material composition based on the physics and chemistry of those materials. A more detailed account of this process can be read in the paper by Green et al., (1998) and Roberts and Herold, (2004) (Green et al., 1998; Roberts and Herold, 2004). AVIRIS imagery flight lines analyzed are of areas around Canyonlands National Park (Figure 12).

The AVIRIS data used for this study were obtained from the JPL website (aviris.jpl.nasa.gov/alt_locator/) for multiple flight lines in the Canyonlands National Park area in Utah and Arizona on the Colorado Plateau. The flight ID numbers for the flights used were f110512t01p00r07, f110512t01p00r08, f110609t01p00r13, f110615t01p00r05, f110623t01p00r10, f111110t01p00r08, and f111110t01p00r09. These flight lines were flown on 05/12, 05/12, 06/09, 06/15, 06/23, 11/10, and 11/10 of 2011, respectively. The data sets came as zipped archive files and were extracted then loaded into the Environment for Visualizing Images (ENVI) software for analysis. AVIRIS images were examined for quality and usefulness (e.g. clarity, cloud cover, bad data, etc.).

Imaging spectrometer data collected in the Mono Basin and the Owens/Death Valley areas were also used for this study. The main areas of collection were the Panum Crater and surrounding vicinity in Mono Basin at approximately 37^0 55.537' N, 119^0 02.923' W, part of the Lee Vining quadrangle in the California 7.5 minute topographic quadrangle (Sharp and Glazner, 1997). The Owens/Death Valley collection took place in

the Mazourka Canyon OHV park between Owens Valley and Death Valley at the base of the Inyo Mountains, the approximate coordinates for this site are 36^0 49' 18"N, 118^0 05' 17"W. A collection of spectra were also taken from the Santa Cruz mountains at approximately 37^0 07' 26.55"N, 122^0 00' 42.22"W for analysis of how soil reflectance changes with the same material under different disturbance conditions.

B.   **METHODS**

1.   Atmospheric Correction

Atmospheric correction must be performed on the AVIRIS data to remove the effects of atmospheric absorption and scattering in order to obtain the surface reflectance of a material for comparison to library spectra (Figure 16). Atmospheric corrections are applied on a pixel by pixel basis in order to analyze reflectance for materials in specific regions of the imagery. AVIRIS data were atmospherically corrected using the Fast Line-of-sight Atmospheric Analysis of Spectral Hypercubes (FLAASH) method.
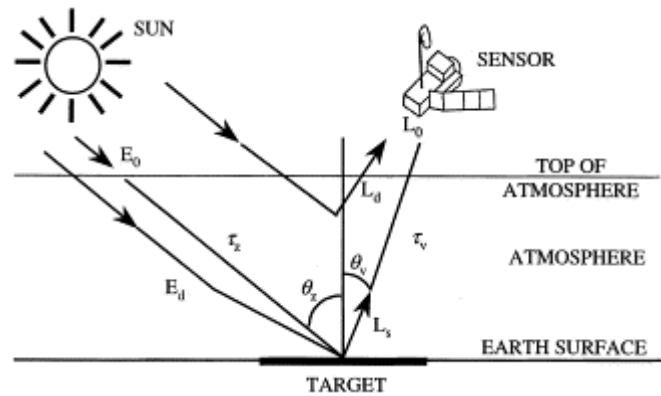
Figure 16.   In this figure from Birvio et al. (2001) the solar radiation interactions are illustrated. E_0 is solar irradiance at the top of the atmosphere, E_d is diffuse solar irradiance. L_s represents radiance emitted from the target, L_d is the atmospheric path radiance and L_0 is radiance measured by the sensor. θ_z and θ_v are downward and upward transmittance from the atmosphere, respectively, and θ_z and θ_v represent the solar zenith and sensor viewing zenith angles, respectively.

FLAASH, which supports hyperspectral sensors such as Hyperspectral Mapper (HyMAP), AVIRIS, Hyperspectral digital Imagery Collection experiment (HYDICE), and a few others as well as multispectral sensors like Advanced Spaceborne Thermal Emission and Reflection Radiometer (ASTER), is an automated atmospheric correction method developed by Spectral Sciences Inc. under sponsorship from the U.S. Air Force (Bernstein et al., 2012). FLAASH performs atmospheric correction on wavelengths in the visible through shortwave infrared regions (up to 3000 nm) incorporating Moderate Resolution Atmospheric Radiance and Transmission Model 4 (MODTRAN4) radiative transfer code into the processing. Options include standard MODTRAN atmosphere and aerosol types, but FLAASH also allows for correction for the adjacency affect, where pixel mixing occurs as a result of surface-reflected radiance scattering. An average aerosol/haze amount can also be calculated for the scene, and cirrus and opaque clouds can be masked (Kruse et al., 2004). FLAASH begins with the radiance equation at the sensor in the standard form of

$$L = \frac{A\rho}{1-\rho eS} + \frac{B\rho e}{1-\rho eS} + L_a \tag{3}$$

where:

ρ is pixel surface reflectance

ρ_e is the average surface reflectance for the pixel and the surrounding region

S is the atmosphere's spherical albedo

L_a is atmospherically back-scattered radiance

$A\ and\ B$ are coefficients dependent on atmospheric and geometric conditions

The values for A, B, S, and L_a are determined using MODTRAN4 calculations that utilize viewing and solar angles and the mean surface elevation of the measurement. A model atmosphere, aerosol type, and visible range can be selected. The values for A, B, S, and L_a are heavily dependent on the amount of water vapor present. To account for this, MODTRAN4 calculations are looped over a column amount series with selected

wavelengths being analyzed to obtain the estimation per pixel. Two channels are used, an absorption set centered on 1130 nm (a water band) and a reference set taken from beside the water band, in conjunction with a look up table constructed to look up the water vapor values (Bernstein et al., 2012).

Once the water vapor calculation has been completed, Equation (3) must then be solved to get pixel surface reflectance for all of the sensor channels. The calculation computes a spatially averaged radiance image L_e, which is how ρ_e is estimated. The following equation is used to calculate L_e.

$$Le \approx \frac{(A+B)\rho e}{1-\rho eS} + L_a \qquad (4)$$

The averaging is conducted using a point-spread function describing relative contributions of points on the ground to pixel radiance after cloudy pixels have been removed. The ground points are measured at different distances relative to the direct line of sight (Bernstein et al., 2012). Aerosol and haze estimation in the FLAASH model is done using dark land pixels in the imagery. The aerosol/haze amount is obtained by running multiple iterations of Equations (3) and (4) over several visible ranges (say 12–50 Km) and then interpolating the best estimate of the visible range through matching that ratio to an average ratio of ~0.45. MODTRAN4 calculates a final loop over water using this visible range estimation (Bernstein et al., 2012).

In order for the FLAASH atmospheric processing to be conducted information had to be obtained in the form of gain files and flight parameters from the JPL website (http://aviris.jpl.nasa.gov/alt_locator/). These files come as part of the imagery zip files though one must go through them to obtain the required data. This includes information on the elevation of the sensor, average scene elevation, time and date of acquisition, and the latitude/longitude position of the scene center. Figures 17 A and B show the spectrum corresponding to latitude 37 57'43.92"N, -109 47' 46.03"W of the June 23 Canyonlands data set (f110623t01p00r10rdn). Noise-containing bands related to water vapor were removed at wavelengths near 1.4 and 1.9 micrometers by editing the bad bands list of the header file.
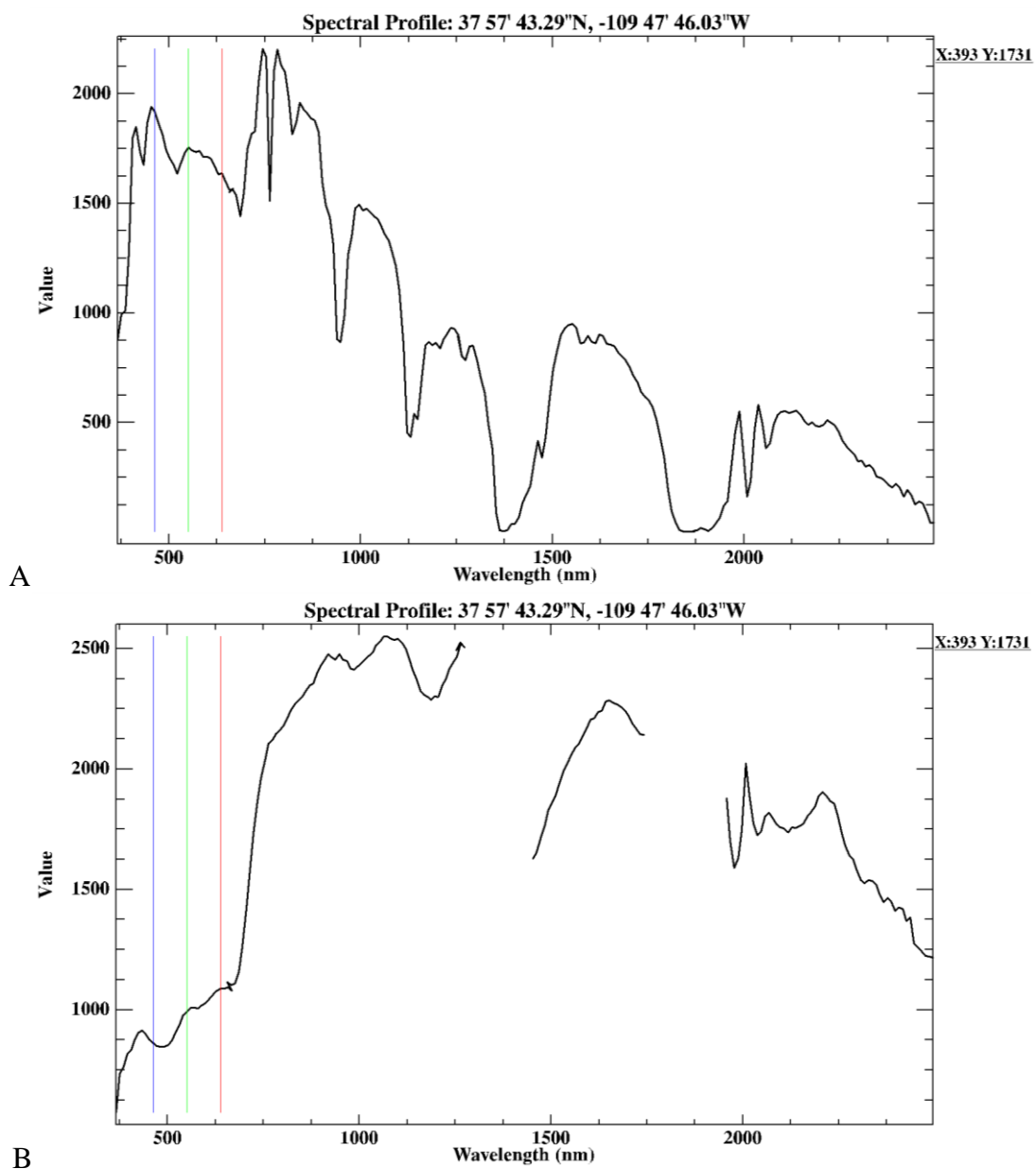
Figure 17.   A illustrates an AVIRIS radiance spectrum from pixel 393, 1731 in the
f110623t01p00r10rdn file before atmospheric correction, and B illustrates
the AVIRIS reflectance spectrum of the same location after atmospheric
correction. Radiance spectrum A illustrates the domination of the spectrum
by atmospheric effects. Reflectance spectrum B shows the spectrum after
removal of the atmospheric effects.

2. Field Spectroscopy

An Analytical Spectral Device (ASD) Imaging Spectrometer was also utilized to collect spectra in the California desert areas of the Mono Lake Basin Owens Valley, and Death Valley. Imaging spectrometers, similar to AVIRIS, measure radiance from surface materials in the UV to near infrared (NIR) and shortwave infrared (SWIR) range (350-2500nm) (Green et al., 1998; Roberts and Herold, 2004). Unlike AVIRIS, an imaging spectrometer, field spectrometers such as the ASD do not portray collections as imagery, but as an individual spectrum or series of spectra (Figure 18) (Roberts and Herold, 2004). Spectra measured consisted of a variety of areas around the Panum Crater Trail and Mazourka Canyon Off Highway Vehicle (OHV) Park. Spectra were taken from areas of zero disturbance, areas of minimal disturbance related to foot paths, areas of light duty dirt roads, areas of heavy duty dirt roads, and areas with both disturbed and non-disturbed vegetation including cryptobiotic soils. Examples of non-atmospherically corrected spectra collected with the ASD imaging spectrometer can be seen in Figure 18.

Figure 18.   This figure shows a series of non-atmospherically corrected spectra collected with the ASD spectrometer.

38

Specimens were sampled during the time periods of 0930–1130 and 1300–1500, falling within the +/- 2 hours of solar noon described by (Roberts and Herold, 2004). Collected spectra were then converted to reflectance using spectral math. The spectral math equation used was s1/s2 where s2 was the average white reference spectrum and s1 was one of the field collected spectra. This process was conducted on each individual spectrum from each collection site, and utilized the site specific white reference spectrum for a given calculation. One of the results of this process can be seen in Figure 19. Once the spectra were in units of reflectance, they were examined for proof of concept with respect to detecting soil disturbance using reflectance spectroscopy and the continuum removal method. To verify if differences were significant enough to be considered spectrally extreme, band depths were analyzed between both the ASD collected spectra and the imagery derived endmembers using the following equations (5) and (6) described by Kokaly and Clark, (1999) and Kokaly (2001). Equation (5) calculates the continuum removed reflectance required to then calculate the band depth using equation (6) (Kokaly and Clark, 1999; Kokaly (2001).

$$R' = \frac{R_{\lambda i}}{R_{c(\lambda i)}} \qquad (5)$$

where:

R' is the continuum removed reflectance at the absorption feature,

$R_{\lambda i}$ is the the reflectance at the base of the absorption feature, and

$R_{c(\lambda i)}$ is the reflectance of the fitted continuum line that corresponds to the absorption feature.

$$BD = 1 - R' \qquad (6)$$

where:

BD is the calculated band depth of the continuum removed absorption feature and R' is the previously calculated continuum removed reflectance from equation (5).

A spectral library was then built and the spectra for the various levels of disturbance were used as inputs for the mixture analysis and mapping of the AVIRIS imagery.
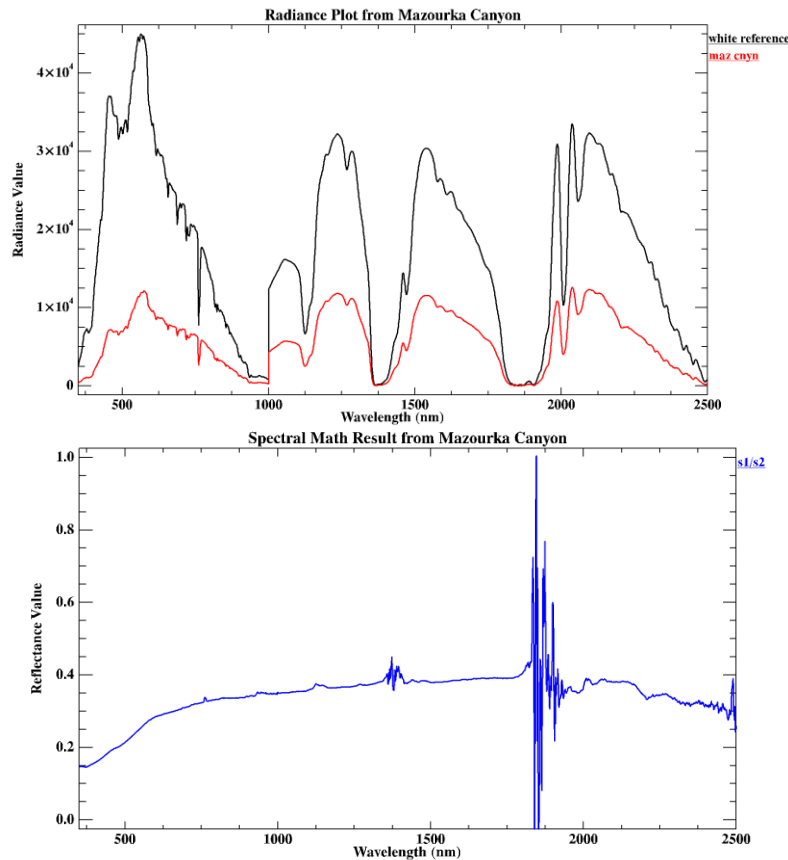
Figure 19.   This figure illustrates the original sample radiance data (red) and white reference spectrum (black) collected with the ASD spectrometer (left) compared to the spectrum calculated using spectral math (right). The blue reflectance spectrum (right), represents the red spectrum (left) divided by the black spectrum (left) (solar spectrum removed).

3.   Spectral Mixture Analysis

The mixture-tuned matched filter (MTMF) approach was used in this research. The MTMF process combines older methods of Matched Filtering (MF), used for target signal detection and signal processing, with newer methods and algorithms that account for mixing of reflectance that occurs within a pixel (Figure 20) (Boardman and Kruse, 2011). The previous MF method had a high false alarm rate and exhibited difficulty distinguishing between similar yet rare targets in the image space because of mixing that

occurs on a sub-pixel level (Boardman and Kruse, 2011). The MTMF method has proven successful at leveraging mixing between a point of interest and the background to eliminate such problems as false alarms during the analysis process (Boardman and Kruse, 2011). Through the combination of spectral unmixing, MF, and convex geometry, MTMF excels at accurately mapping subtle sub-pixel targets with sufficiently reduced false alarms (Boardman and Kruse, 2011).
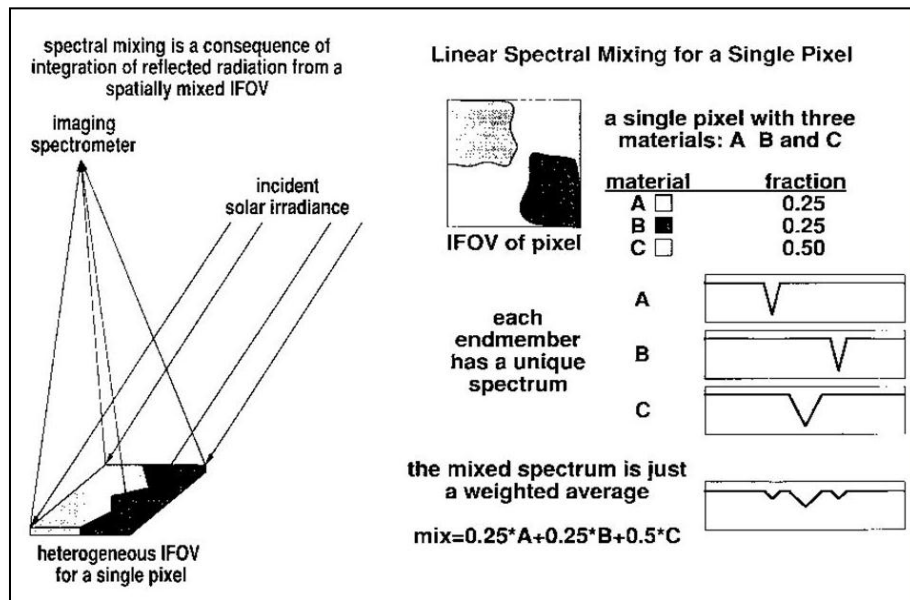
Figure 20.   This figure from Boardman and Kruse (2011) shows how mixing in a picture element (pixel) occurs based on 2 (left) and 3 (right) endmember concepts. The 3 endmember example shows how this occurs both spatially and spectrally within the pixel.

The MTMF method is broken into the following steps: pre-processing and data preparation, MF abundance estimation, and mixture tuning (MT) to reject any false positives (Boardman and Kruse, 2011). Before MTMF can be conducted, it makes sense to first derive endmembers from the data using the hourglass method illustrated in Figure 21 (below) (Boardman and Kruse, 2011). For the purposes of this research, endmembers have been derived both from the data using the hourglass approach described in (Boardman and Kruse, 2011), as well as via the use of a spectral library created using the ASD collected spectra. Imagery derived endmembers come from the AVIRIS flight lines

after atmospherically correcting the data using the FLAASH method described previously. As Figure 21 illustrates, once the endmembers have been identified, the next step is to perform MTMF to determine where endmembers occur within an image and what their abundances are within a given pixel. Once this has been conducted, maps of this information can then be generated (Boardman and Kruse, 2011).
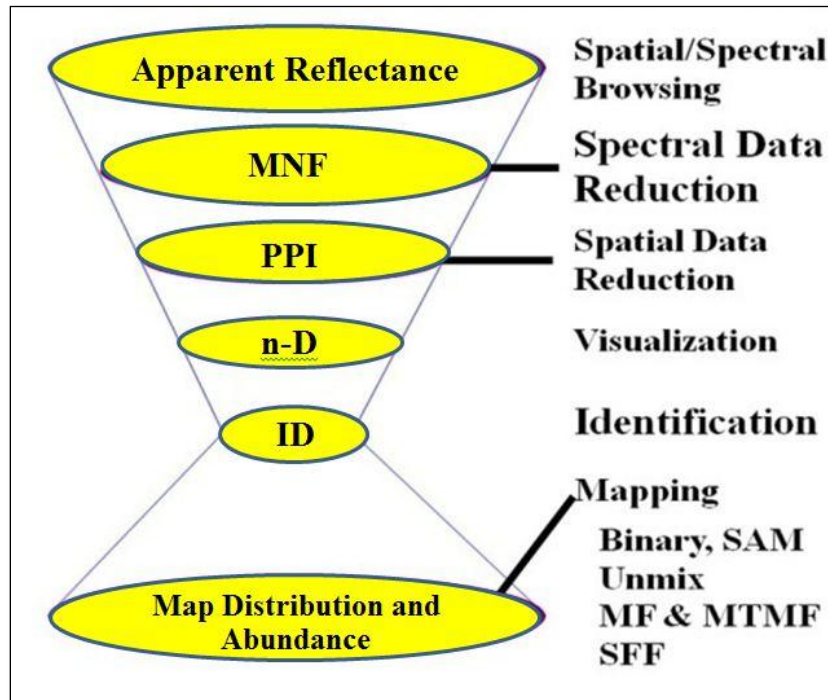
Figure 21.   This figure shows the processing methods for spectral mixing analysis using the N-dimensional approach adapted from Kruse et al., (2003) and Boardman and Kruse (2011).

a.   *The Hourglass Approach*

The hourglass method is suitable for the purposes of this study because it allows for accurate endmember extraction without any prior knowledge of location details (Boardman and Kruse, 2011). In general, the hourglass method converts radiance data to apparent reflectance (required for spectral analysis) using an atmospheric correction model (in this case FLAASH). The minimum noise fraction (MNF) (transformation resulting in new components being ordered by image quality (Boardman

and Kruse, 2011; Green et al., 1988)) portion performs noise suppression within the data as well as some reduction in both spatial and spectral space. Pixel Purity Index (PPI) determination is where the purest pixels (endmembers) are identified using convex geometry. Endmembers are then visualized through utilization of the n-dimensional visualizer in the ENVI software package. The endmembers were identified through the use of both the ASD spectral library described previously and libraries built by USGS (Clark et al., 2007). The endmembers were then run through the MTMF spectral (partial) unmixing process to determine location and abundance in the HSI data.

b.   The MTMF Method

MTMF involves three analysis steps. Step one involves an MNF transform, step two calculates the matched filter, and step three is where mixture tuning (MT) occurs. MT utilizes convex geometry to measure pixel mixture probabilities that are composites of both the target spectrum and background spectra. MTMF is an automated process that only requires the data and predetermined endmembers (Boardman and Kruse, 2011). In order for step one to occur, pre-processing of the data must be completed. Pre-processing has two main objectives performed as part of the execution of the MNF transform (Boardman and Kruse, 2011). During the pre-processing phase, noise whitening is done via decorrelation of noise present in the data and unit variance across all dimensions of the spectra. The noise whitening and data characterization step is a crucial part of the MTMF process because it is a main element of what allows estimation and target detection within the imagery (Boardman and Kruse, 2011). Three possible options exist in estimating an MNF transform, estimation using a shift difference, using a dark current image, or through use of known noise parameters. All three methods are statistical approaches that are useful under varying conditions. The end result is to determine the eigenvectors and project the noise whitened data onto them in order to decorrelate the data using equation (7) from Boardman and Kruse (2011).

$$D_{mcnw(i,j)} = NW * N_{evec} * (D_{(i,j)} - dm_j)^T \tag{7}$$

where:

$D_{mcnw(i,j)}$ is the mean corrected and noise whitened result

NW is the diagonal matrix with elements being a square root of the reciprocal to the noise eigenvalues

N_{evec} is the nb, nb matrix of noise eigenvectors with nb being the number of bands

$D_{(i,j)}$ is the original data set as a number of pixels, number of bands matrix

dm_j is set as the mean value of a band j of $D_{(i,j)}$

The goal of step two is use of the calculated matched filter along with the minimum noise fraction (MNF) to estimate target abundances on a sub-pixel level. With the final MNF output (D_{mnf}) being calculated using equation (8) from Boardman and Kruse (2011).

$$D_{mnf} = D_{mcnwevec} * D_{mcnw} \tag{8}$$

where:

D_{mnf} is the MNF data,

$D_{mcnwevec}$ represents the diagonal covariance structure containing MNF eigenvalues that are equivalent to the covariance values,

D_{mcnw} is the principal component transform result from the data that has been both mean corrected and noise whitened.

The MNF data have a zero mean and uncorrelated unit variance white noise that, when projected onto their eigenvectors, yield a diagonal covariance structure. The covariance values are equal to the MNF eigenvalues and are the base by which MTMF processing then occurs (Boardman and Kruse, 2011).

When a pixel is filled with certain materials, the degree of spectral variability is reduced simultaneously. If the pixel is filled to 50% with that material, one encounters

the situation where mixing freedom within the pixel is halfway between the background-plus-noise freedom of a 0% filled pixel and the noise-only-freedom of the pixel filled to 50% (Boardman and Kruse, 2011). It is this concept that allows the MTMF process to identify false positives by placing pixels well outside their plausible mixing freedom into an infeasible mixtures category. Finally, MTMF creates a distribution range for feasible mixtures (Boardman and Kruse, 2011). Further details on the mathematics behind this process are given in the paper by Boardman and Kruse (2011).

The MNF process revealed that the eigenvalues for the AVIRIS f110512t01p00r07 flight log drop to 1 at approximately eigenvalue band 49, which means that the bands after eigenvalue band 49 contain mainly noise. Based on this, the data were then reduced from the initial 207 bands used to using only the first 50 bands in steps after the MNF process in order to eliminate noise from the data and providing a new dimensionality of 50 (Figure 22).
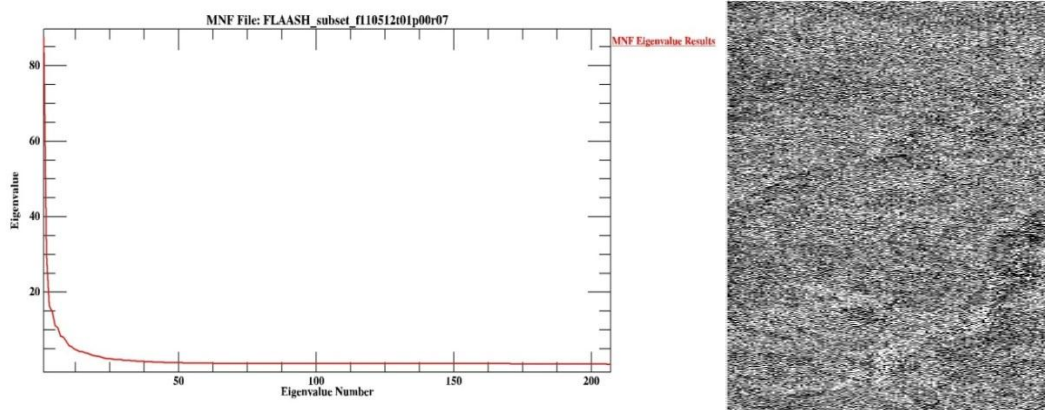
Figure 22.   The plot (A) shows that the eigenvalues calculated for the image drop toward 1 at approximately eigenvalue band 50, meaning that most of the data in this band is noise. The bottom figure (B) is a visualization of eigenvalue band 50, confirming that though there is some signal present, band 50 is dominated by noise.

As an example of the Pixel Purity Index (PPI) calculation using the f110512t01p00r07 data set, the number of PPI iterations was set at the default setting of 5,000 iterations, and a PPI threshold value of 2.5. The resulting plot can be seen in Figure 23. When looking at the plot, the curve flattens off at around 2000 iterations, so the index was run a second time with 3000 iterations because 5000 seemed unnecessary. The lower iteration plot can

also be seen in Figure 23. The leveling off of the pixel purity index curve at approximately 2000–3000 pixels is the basis that determines the maximum number of pixels to be used in the visualization step. To be sure that the best subset possible was used, 3000 pixels were set for the maximum. Once the purest pixels were identified and previewed, they were then extracted as endmembers.

Two options for endmember extraction are possible, the first is imagery derived endmembers, which intuitively means that the endmembers are extracted from the imagery itself and is generally thought of as the best option (Kruse and Boardman, 2011, Kruse and Perry, 2009). The second option is to input user supplied endmembers, which means one can input field or laboratory collected spectra into the algorithm and try to detect those as target material. Both options were run on the two data sets with the highest spatial resolution for the Canyonlands site. The data sets were AVIRIS flight logs f110512t01p00r07 and f110512t01p00r08 with 2.9 m and 3.3 m spatial resolution, respectively. In some cases a third data set with 15.2 m resolution was utilized (f110623t01p00r10). This was done for two reasons; the first is because the BSC component does not necessarily take up large areas and the bigger the pixel, the less likely it is that BSCs will be detectable in the imagery. To test how the BSCs and other endmembers might be distributed in the imagery, they were compared to the results using imagery derived endmembers. The second reason it was run on two data sets was for a repeatability test with the same endmembers at the same success rate. To try and create the most similar conditions, the data sets with the most similar spatial resolution and topography were selected; the third data set was used when further testing was required. Figure 24 shows some of the 48 endmembers derived from the imagery sets compared to the spectra collected using the ASD imaging spectrometer in the Owens/Death Valley area and input as user supplied endmembers. MF and infeasibility scores were then used to determine areas with high MF and low infeasibility scores. These correspond to areas with high abundance and feasible mixtures.   These areas were then analyzed to see if the endmembers could actually be related to any features within the imagery and potentially mapped as areas of interest.
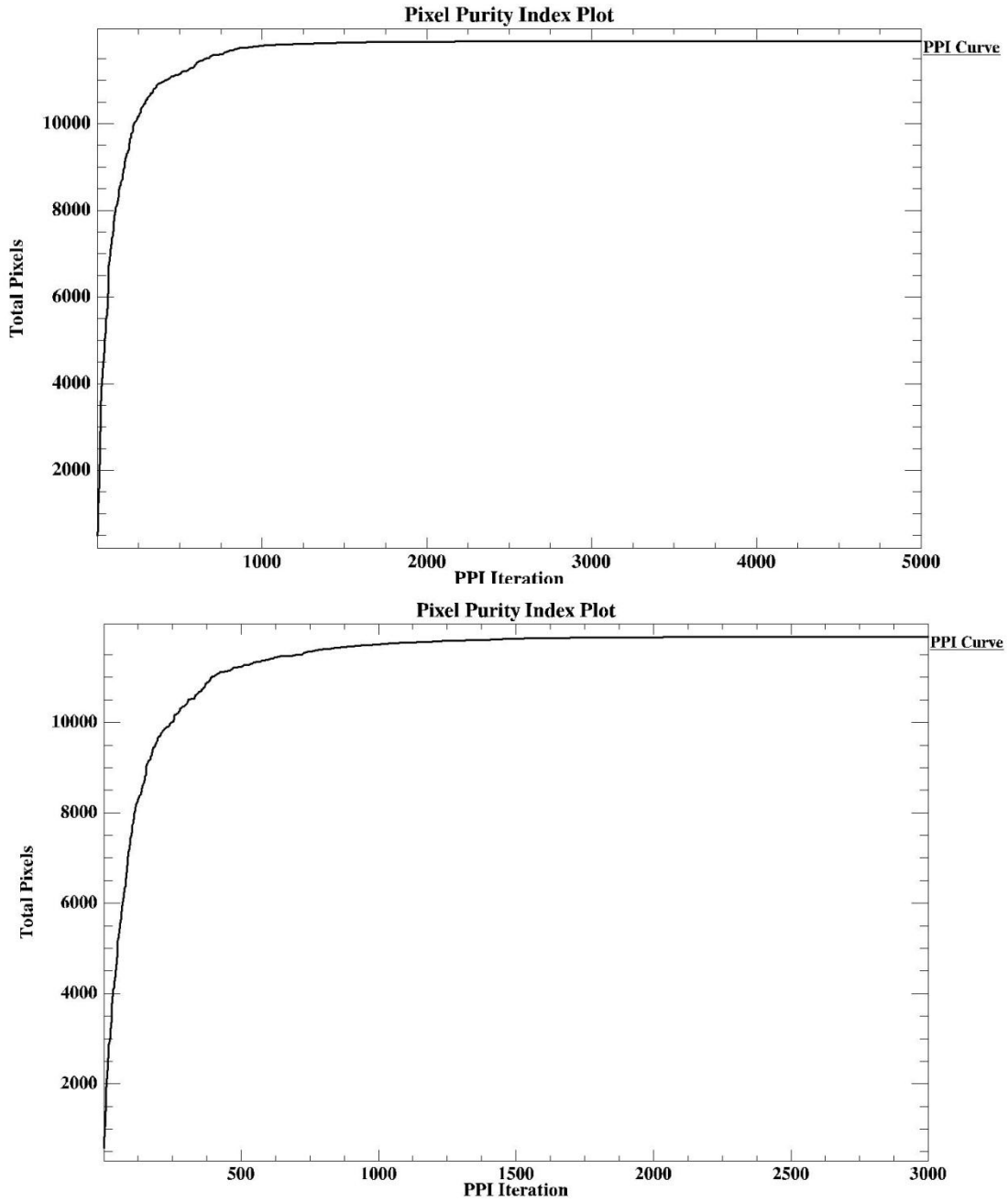
Figure 23.   This figure illustrates the number of times a pixel is marked as pure and shows the leveling off of pixels at around 2000. Analysis of this graph helps to determine how many pixels to use in visualization and endmember derivation.
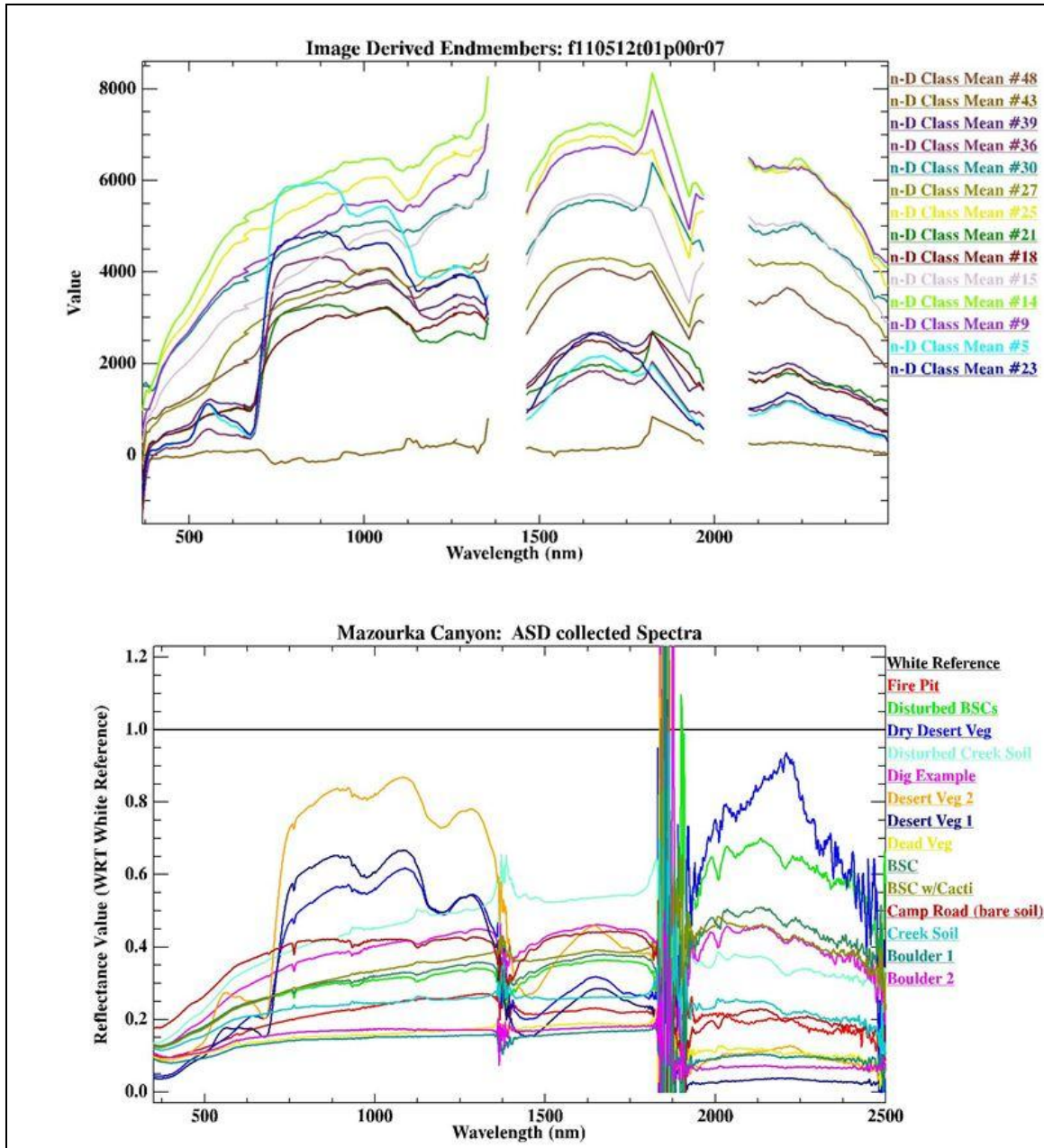
Figure 24. This figure is a comparison between the imagery derived endmembers (top) and the spectra collected from Owens/Death Valley Mazourka Canyon (bottom). Looking at the two plots, one sees similarities between the two so it is feasible that using the collected spectral library may be useful as an endmember input for the AVIRIS imagery.

VI.   RESULTS AND ANALYSIS

Spectral libraries collected using the ASD spectrometer were analyzed to determine if differences could be seen in reflectance and absorption features of spectra between those collected before and after disturbance. This was primarily to determine if changes in soil characteristics could be immediately seen within the individual spectra. Upon examination there were visual differences in spectra collected from the same location before and after disturbance and they are illustrated in Figure 25 below. The most noticeable differences show up around 500 nm (0.5 µm), 1125 nm (1.13µm), and 2200 nm (2.2µm) and are regions of absorption features in the spectra. These changes show not only difference in apparent reflectance, but also show variation in the width and depth of the absorption features at these key locations when using the continuum removed function previously discussed.
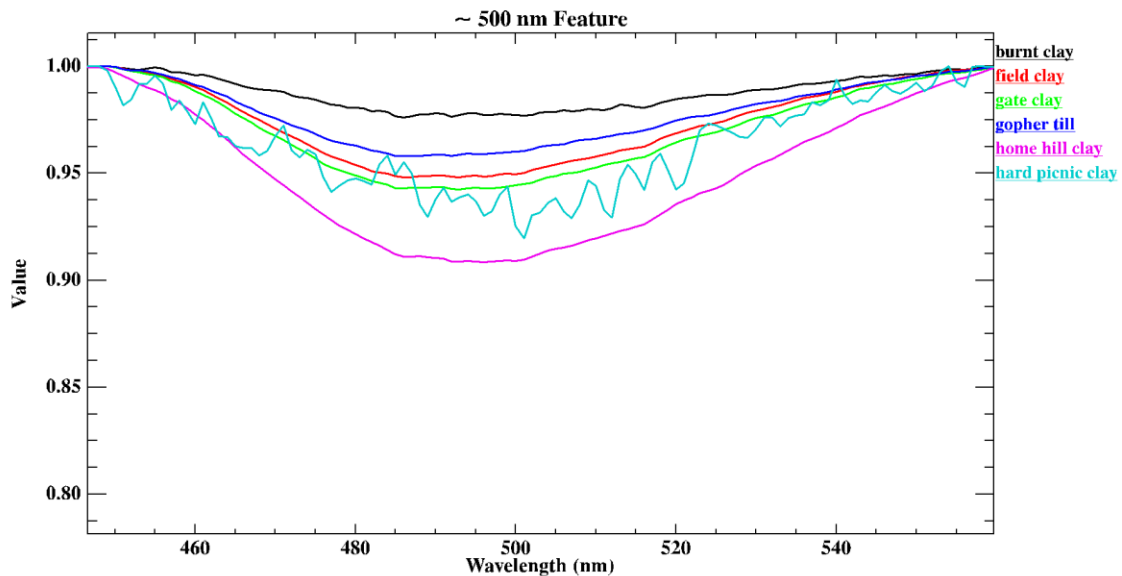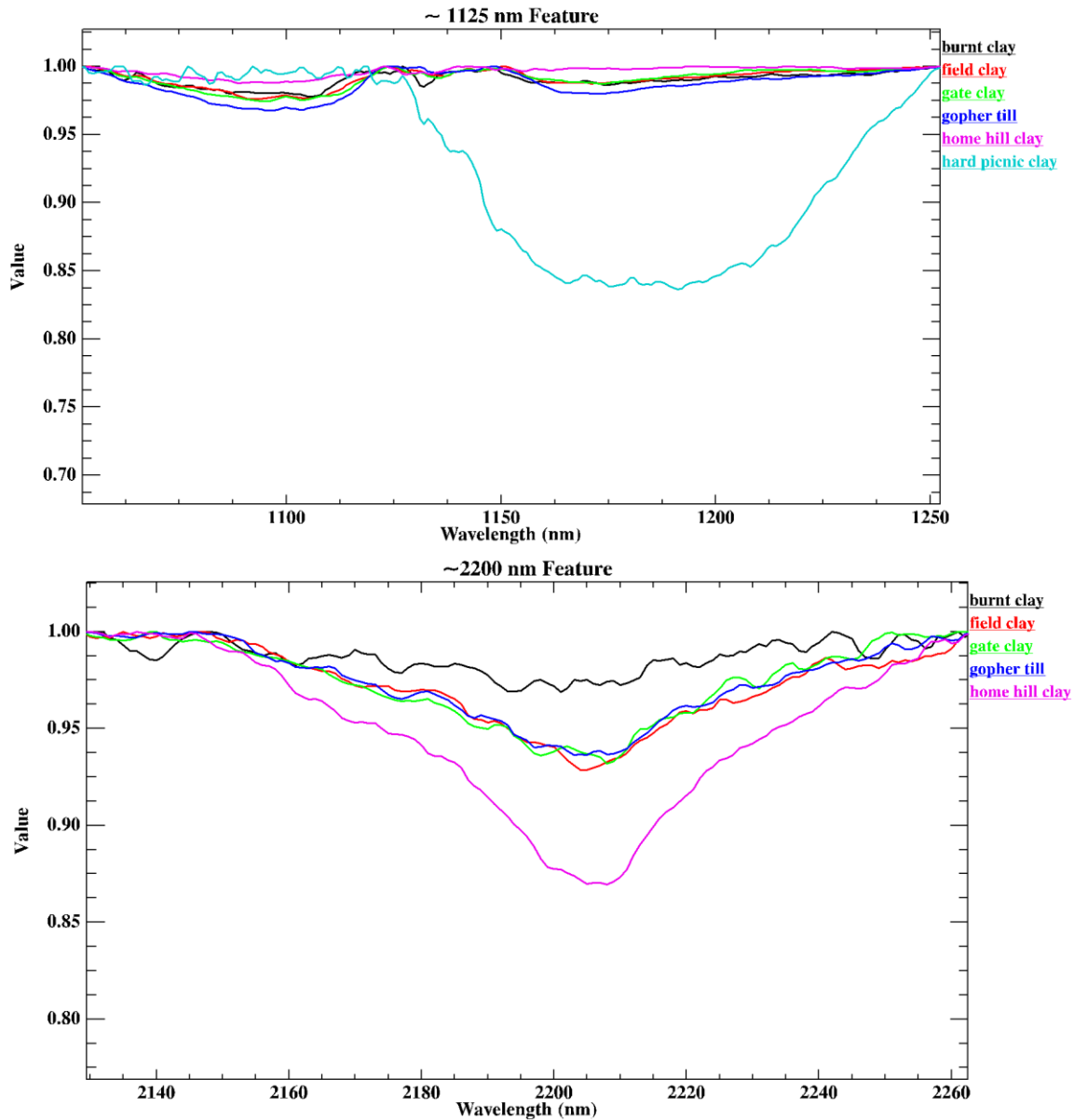
Figure 25.   This figure shows ASD collected soil spectra under various conditions of impaction/surface disturbance with the continuum removed. Variation in feature depths and widths at 500 nm, 1100–1125 nm, and 2200 nm are measureable, supporting the prediction that surface disturbances are detectable in Hyperspectral imagery. The depths of features show an overall pattern of decreasing feature depth with increasing disturbance at 500 nm and 2200 nm. At 1125 nm the depth of features seemed to increase, for the most part, with increasing disturbance.

The absorption feature band depths for the ~500 nm, 1125 nm, and 2200 nm features are 0.0232, 0.0176, and 0.0304 for burnt clay (Table 1). The field road clay values were 0.052, 0.0193, 0.0745, gate clay values 0.057, 0.021, 0.0645, gopher till values 0.0419, 0.026, 0.073, home hill clay values 0.092, 0.0087, 0.137, and hard picnic area clay values 0.0805, 0.154, 0.000 (flat) are for 500 nm, 1125nm, and 2200 nm, respectively (Table 1). The continuum removed values are representative of the depths of the absorption features at each wavelength calculated using (5) and (6), and are thought to be associated with how the soil components are altered with various levels of disturbance. As previously mentioned, Clark and Roush (1984) discussed how the use of the continuum removed function allows one to analyze a spectrum that is not heavily influenced by the processes of other minerals in a mixture or those within the mineral itself. Therefore, the depths of the absorption features and the changes occurring amongst them must be related to some change in the intrinsic properties of the soils themselves, as was suggested by Prose (1985) and postulated by this study.

Table 1.   This table lists the absorption feature depths for each soil spectrum using the continuum removed function and the deepest portion of the feature. The values listed show changes in the depth of features for the same material under different disturbance conditions for wavelengths of ~500 nm, 1125 nm, and 2200 nm. The depths are ordered by least to greatest disturbance and show, for the most part, a trend of decreasing depth, increasing depth, and decreasing depth at 500 nm, 1125 nm, and 2200 nm, respectively.

Absorption Feature Depth

Spectrum	500 nm	1125 nm	2200nm
Hill Clay	0.092	0.0087	0.137
Field Road Clay	0.052	0.0193	0.0745
Gate Clay	0.057	0.021	0.0645
Gopher Till	0.0419	0.026	0.073
Burnt clay	0.0232	0.0176	0.0304
Hard Picnic Area Clay	0.0805	0.154	0

Looking at Figure 25 it is apparent that the top four spectra are the same material based on the similarity of the visible features. The only exception to the similarities of the spectra is the hard packed picnic area clay. However, the picnic clay spectrum (with the continuum line) has heavily subdued features that are much shallower in depth and shifted slightly. When considering this, there are some similarities between it and the other spectra. The burnt clay expresses higher overall reflectance values than the gopher till, but has more similarity to the hard packed clay than the other soil spectra. Like the hard packed clay, the burnt clay absorption features are subdued and the absorption feature at 2200 nm seems to have disappeared altogether. The home hill clay is the least disturbed of the samples, the gopher till was a recent dig site and had not been exposed to any rains or sitting long. Gate clay was a less recent dig site conducted a few months prior to collection that was then packed back down, and the field road clay has been exposed to impact disturbance on a level between the home hill and picnic clay spectra. Based on the fact that each spectrum is comprised of the same soil material and were collected under the same weather conditions, the only known differentiating factor between them is the level and type of disturbance the soil has been exposed to and is likely the cause of the differences illustrated by the spectra.

Table 1 has spectra ordered by least to greatest disturbance with hill clay being the least and hard picnic clay considered the greatest; however the type of disturbance seems more relevant at this point. Using hill clay as the undisturbed reference as previously discussed, impact-related disturbances show decreases in absorption features at 500 nm and 2200 nm but increases in depth of absorption features at 1125 nm. Digging-related disturbances show decreases in absorption features at all three wavelengths. Burning disturbances show a decrease in feature depth at 500 nm and 2200 nm, and increase in feature depth at 1125 nm similar to impacts. Since the patterns of depth change at each wavelength are the same for the same type of disturbance, it can be inferred that depth changes increasing at 500 nm and 2200 nm can be correlated with impact disturbances and those that decrease at all wavelengths can be correlated with digging disturbances. Also, a burn disturbance seems to register a pattern similar to that of impact disturbances but the depths do not appear to change as much.

BSC collected spectra show similar results to those discussed by Weber et al (2008) and O'Neill (1994) with an absorption feature around 650 nm that can distinguish BSCs from bare soils because bare soils have a mainly flat spectrum in this region. The absorption features can be seen in Figure 26 along with a spectrum of soil (bottom) that does not have the absorption feature at 650 nm; these features have been emphasized using the previously discussed continuum removal method. Also of note is the difference in reflectance between the healthy BSC spectrum and the disturbed BSC spectrum representing a measure of 0.00359 difference in depth calculated using the difference of the results of each spectrum from equations (5) and (6). The deepest portion of the feature is also shifted from 675.40 nm for the healthy BSC to 685.20 nm for the disturbed BSC. The disturbance for this particular BSC is related to trampling by foot traffic of one pass. This means a single footstep registers an immediate decrease in feature depth of 0.00359, a shift to longer wavelengths of 9.8 nm, and visible narrowing of the feature for this BSC.
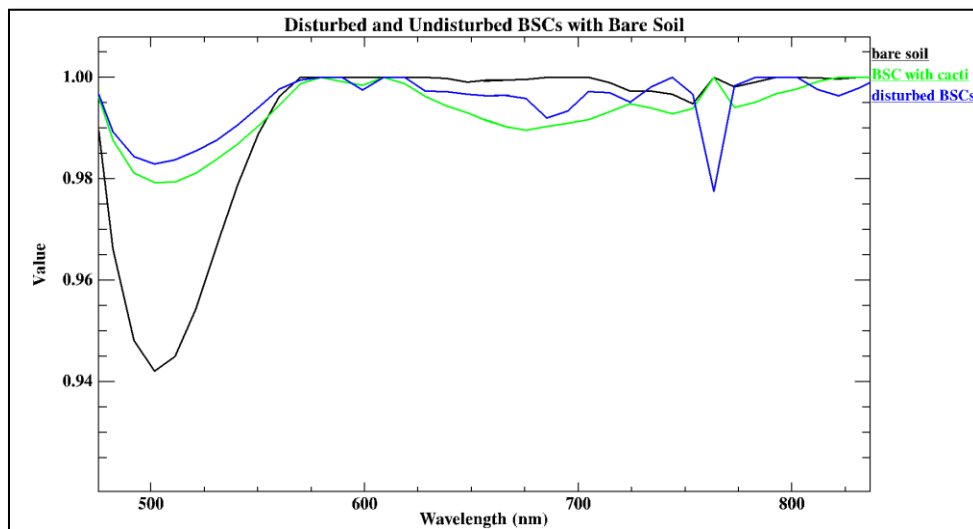
Figure 26.   This figure shows undisturbed and disturbed BSC spectra collected from Mazourka Canyon plotted with bare soil. These BSCs have a prominent absorption feature around 650 nm similar to that observed by Weber et al (2008) that is useful for discrimination from bare soils. The absorption feature at 650–700 nm changes in width and depth between BSCs. Also, as mentioned by Weber et al (2008) the bare soil does not express the absorption feature. The feature exhibited by the spectra at around 760 nm is possibly due to ozone that was not fully removed by the atmospheric correction.

A. IMAGERY DERIVED ENDMEMBERS

The initial run of the MTMF algorithm was conducted using imagery derived endmembers for the purpose of determining if the patterns observed were comparable to those of the collected field spectra. Imagery derived endmembers are obtained from the imagery itself and are typically thought to yield the best results so should provide a good standard of achievement for the user supplied endmembers (Kruse and Boardman, 2011). The MF score verses infeasibility plots of imagery derived endmembers were also analyzed to see how imagery derived endmembers stacked up against user supplied endmembers (Figure 27). Figure 27, inset C shows a 2D scatter plot of MF versus infeasibility for the mean class 1 endmember from the f110512t01p00r07 flight and includes a true color version (Figure 27, inset A) of the imagery for comparison.

The colored area (Figure 27, inset B) is the class created in the scatter plot based on the criteria of a high MF score and low infeasibility score, corresponding to areas with high abundances (0.30–0.76) and feasible mixtures with the composite background. The imagery depicted in Figure 27 is from flight f110512t01p00r07 of the Newspaper Rock National Historic Monument area near the Needles entrance of Canyonlands National Park so trails are expected. The average trail can be between 2 and 6 feet depending on what it is used for. With a resolution of 2.9 m per pixel (9.5149 ft), a 0.61 m (2 ft) trail would represent a maximum of 21%, a 1.22 m (4 ft) trail would be a maximum of 42%, and a 1.83 m (6 ft) trail would reach a maximum of 63% of the pixel. Based on the results from endmember 1 and other imagery derived endmembers, and the maximum possibilities for trails, which would be the largest target to identify, the goal for a match of user supplied endmembers will be between 15−60 %. Mainly the 15−60% range is based on the fact that while achievable higher percentages are possible with imagery derived endmembers, user supplied endmembers utilized for imagery are from geographically different areas. Therefore, the expectation is that the user supplied endmembers will produce less accurate results.
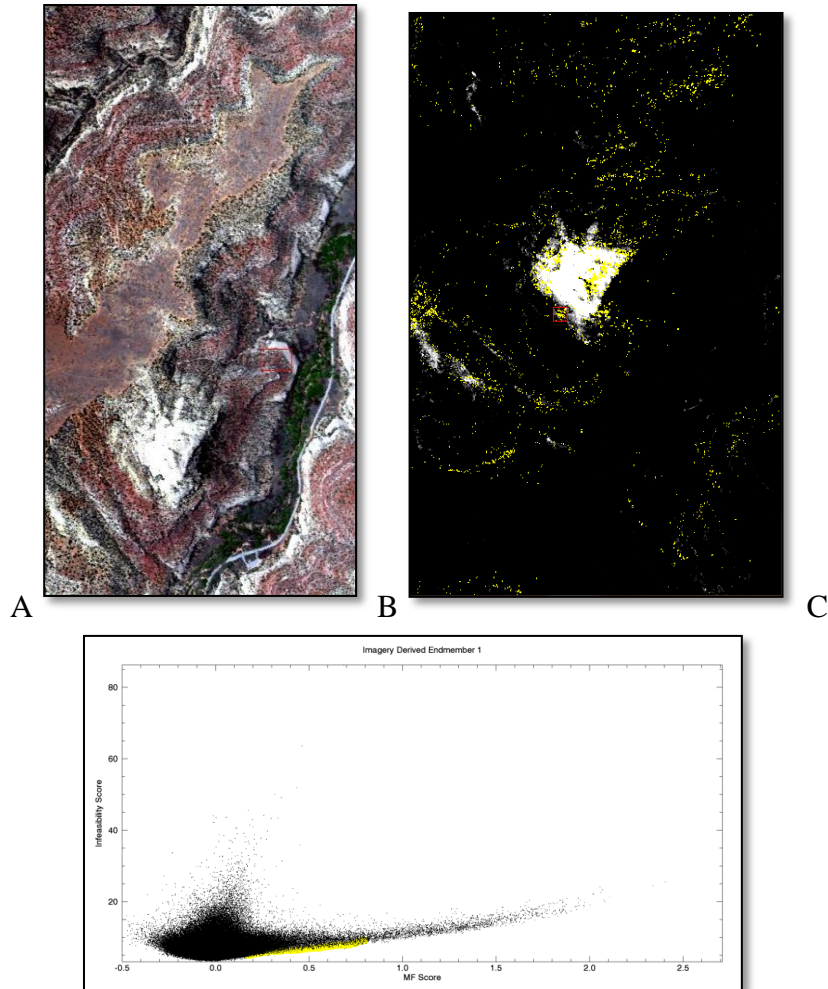
Figure 27.   This figure shows the true color image (A) and the associated MF verses infeasibility scatterplot (C) being utilized to analyze an imagery derived endmember and see what type of score distribution is associated with areas of the highest pixel concentration. In B, Yellow ranges are areas with low infeasibility and high MF scores highlighted in the scatterplot, and represent the most likely areas for target mixtures. The range associated with these areas contains 30–76 % of the endmember.

Figure 28 illustrates some of the imagery-derived endmembers utilized. Figure 29 illustrates one of the imagery derived primary soil components identified using the USGS mineral spectral library as a possible zunyite mixture. Zunyite is a mineral common to the San Juan County area of Colorado and is associated with the Zunyite Mine in Anvil Mountain of the Red Mountain District proving it to be a feasible match for the imagery area (http://www.merriam-webster.com, http://colorado.hometownlocator.com).

55
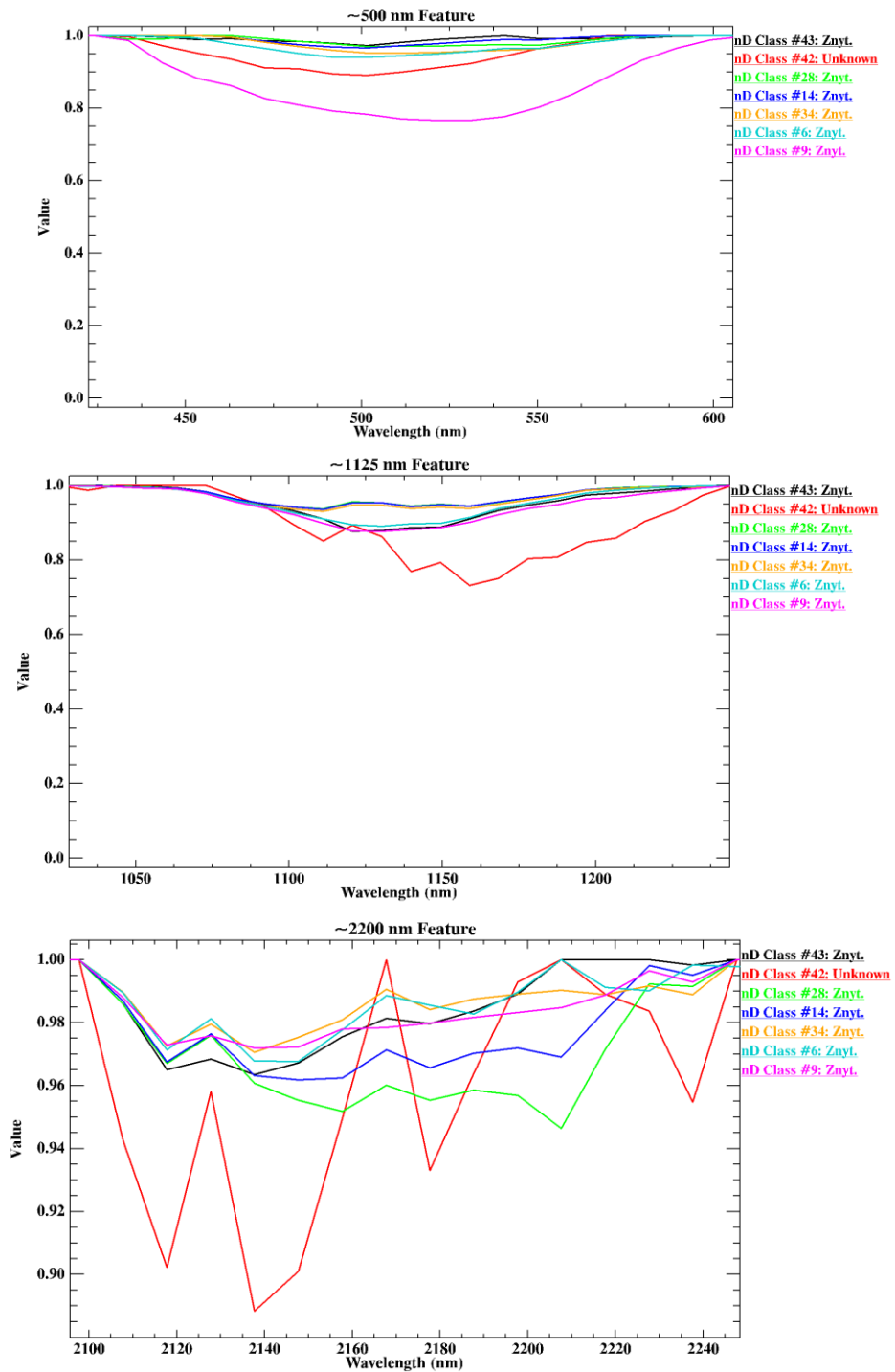
Figure 28.   The above shows some of the imagery derived endmembers from the Colorado AVIRIS flight log f110512t01p00r07 where the endmember has been identified as a Zunyite mixture. The continuum removal allows us to see how absorption feature depth differences show a similar pattern to those collected with the ASD spectrometer in figure 24 at ~500 nanometers, 1125 nanometers, and 2200 nanometers.
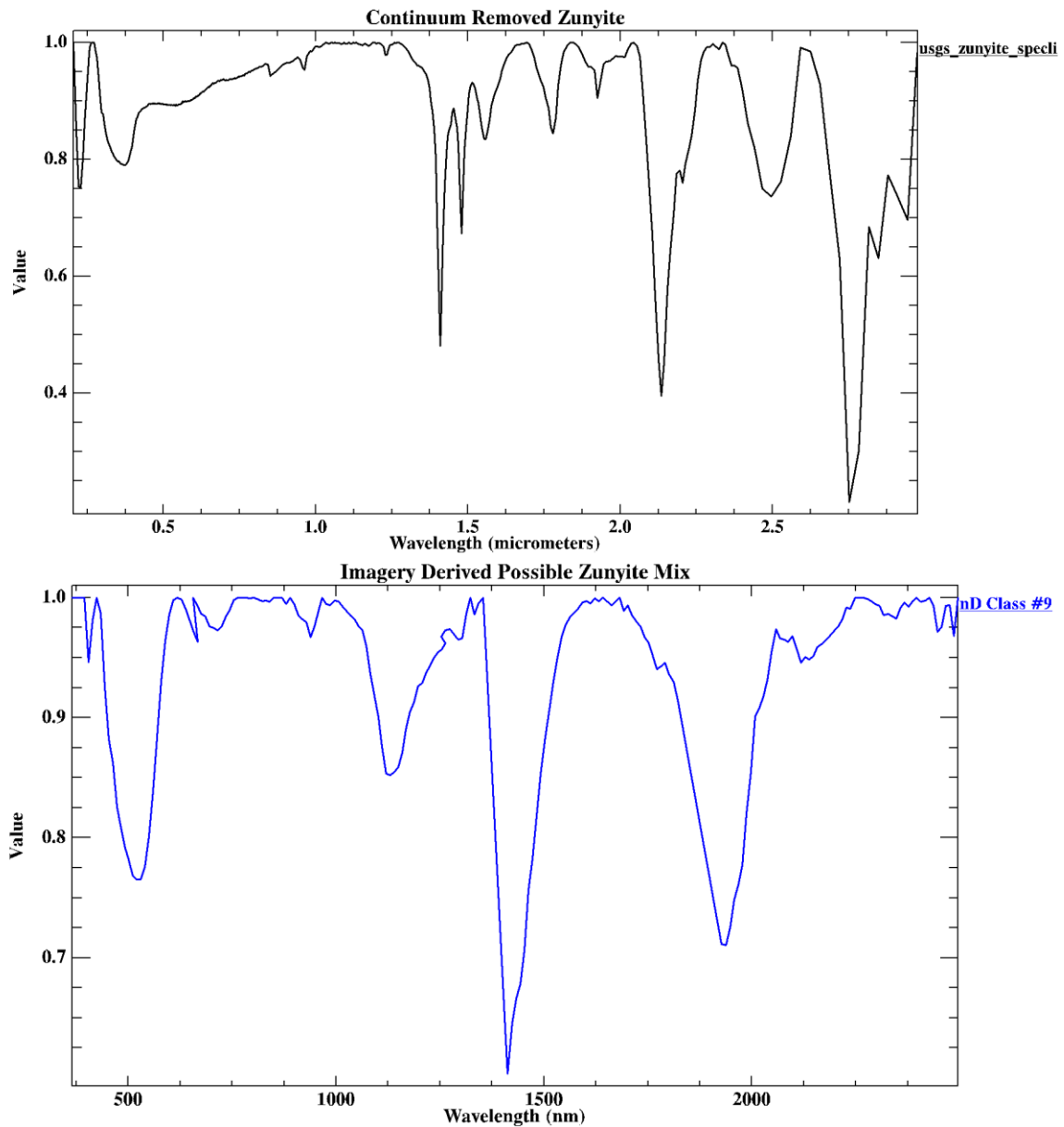
Figure 29.   This figure shows the USGS spectral library entry for Zunyite and the
imagery derived endmember mean class 9 thought to be a Zunyite mix.
Both spectra are shown with the continuum removed.

The zunyite spectra show similar spectral reflectance differences to those
observed by Smith et al (2004) as well as in the ASD clay collected spectra previously
discussed (Figure 28).   Differences again show up at the wavelength regions of
approximately 500 nm, 1125 nm, and 2200.   Like the spectra collected using the ASD

spectrometer, reflectance values were used to identify regions of change in absorption feature overall spectral reflectance for the zunyite mixtures. These endmembers were also analyzed using the continuum removed method to calculate the absorption depths at 500 nm, 1125 nm, and 2200 nm for endmembers. Absorption feature depths for endmembers 6, 9, 14, 28, 34, 43, and 42 are 0.056, 0.133, 0.0340; 0.225, 0.1281, 0.0350; 0.034, 0.0693, 0.0376; 0.028, 0.0688, 0.0535; 0.047, 0.076, 0.0293; 0.026, 0.128, 0.050, and 0.109, 0.301, 0.117, respectively (Table 3). The similarity between the band depth calculation results of both the user-supplied endmembers and the imagery-derived endmembers suggest that differences in the features can potentially be related to different levels of disturbance affecting the surface material (Table 3). The spectra in Figure 28 also show slight shifts in location and prominence of the features. Widths of features in this case varied as well.

For the clay collect, the hill clay sample appeared to be the least impacted by disturbance and was therefore used as a control to determine the disturbance-related differences. Since the least impacted clay sample had similar reflectance characteristics to the imagery derived zunyite endmember 28, that endmember was used for the zunyite control. The average differences in absorption depth at 500 nm, 1125 nm, and 2200 nm for the ASD collected clay spectra and imagery derived zunyite endmembers are 0.0342, 0.0190, .0738; 0.0476, 0.0553, and 0.0207, respectively (Table 2). These values shown represent the difference in depth of absorption features (including the averages) at each respective wavelength for two different materials with similar, not identical properties. Since these materials are similar, not identical, some minor differences are expected.

For example, impact-related disturbances in the clay showed a decrease in the feature at 2200 nm; endmembers derived from the imagery also showed patterns of absorption features decreasing in the SWIR region of the electromagnetic spectrum with respect to what is thought to be an undisturbed zunyite spectrum; but unlike the clay, they show an increase at 1125 nm. While the patterns of feature depth do not match those of the clay at 1125 nm, the correlation is still possible because the clay and zunyite materials are not an exact match. Certain features may express themselves differently at 1125 nm because those features are related to vibrational processes while wavelengths less than

1000 nm are affected by electronic processes (Clark, 1999; Jensen, 2007). Ground-truthing needs to be conducted to verify a relationship between the observed spectral phenomena of the imagery-derived endmembers and types/degrees of disturbance.

Table 2.   This table shows the differences in absorption feature depth from the imagery derived Zunyite endmembers corresponding to the approximate deepest point of the absorption features at wavelengths of 500 nm, 1125 nm, and 2200 nm. The pattern of difference (features decreasing in depth with greater disturbance) in the 500 nm range were used to try and predict endmembers of greatest disturbance for the Zunyite endmembers because it shows a close value for average depth differences to that of the clay spectra.

Feature Depth Differences

Spectrum	500 nm	1125 nm	2200nm
Burnt clay	0.0688	0.0108	0.1066
Field Road Clay	0.04	0.01849	0.0625
Gate Clay	0.035	0.0093	0.0725
Gopher Till	0.0501	0.02076	0.064
Hill Clay	0	0	0
Hard Picnic Area Clay	0.0115	0.0545	0.137
Average Difference	0.03423	0.018975	0.073767
6 Znyt.	0.028	0.0642	0.0195
9 Znyt.	0.197	0.0593	0.0185
14 Znyt.	0.006	0.0005	0.0159
28 Znyt.	0	0	0
34 Znyt.	0.019	0.0072	0.0242
43 Znyt.	0.002	0.0592	0.0035
42 Unknown	0.081	0.197	0.0635
Average Difference	0.04757	0.0553429	0.020729

While it is understood that such properties as grain size and soil moisture content can have effects on reflectance values (Ben-Dor et al., 2003), the fact that impact energy applied to the soils also can have dramatic effects on these characteristics is the reason

such an inference can be made (Ben-Dor et al., 2003; Davis, 2007; Prose, 1985).   Other imagery-derived endmembers corresponded to various types of vegetation, rivers, paved roads, and different mineral depositions.   These endmembers were evaluated only on their ability to be identified within the imagery as a method of determining what spatial extent should be expected and as a comparison to where user supplied endmembers were detected to make sure there was no crossover.

Table 3.   This table shows the depths for the zunyite features in the order of decreasing feature depth at 500 nm. It is inconclusive how the pattern of feature depth change is associated with different levels of disturbance, though patterns of change with respect to the reference endmember 28 can be seen. These are imagery derived endmembers so the level of disturbance is unknown. Without proper ground-truthing there is no way to be sure if a relationship exists, however the similarity between these patterns and those in the clay spectra suggests disturbance can be correlated with these changes in depth as well.

Imagery Derived Endmember Depths: Zunyite

Endmember	500 nm	1125 nm	2200 nm
9	0.225	0.1281	0.035
42	0.109	0.301	0.117
6	0.056	0.133	0.034
34	0.047	0.076	0.0293
14	0.034	0.0693	0.0376
28	0.028	0.0688	0.0535
43	0.026	0.128	0.05

B. ASD SPECTROMETER MEASURED ENDMEMBERS

ASD collected endmembers yielded some interesting results. They were, to an extent, able to identify features, however the method required significant human interference, unlike using imagery derived endmembers. User supplied endmembers also rarely turned out MF scores greater than 50% and in many cases they could only achieve 30%. Likely this is the result of the endmembers used being either too dissimilar to materials in the imagery, or not being spectrally unique enough to be detected in large quantity. In this particular study the results were still useful because the size of the features (trails in particular) being identified would generally only occupy a pixel percentage between approximately 20 and 60% in conditions where the feature is unoccluded by other objects in the imagery.

1. Camp Road Endmember

User supplied endmembers from the clay collect, and the Mono/Owens valley areas were processed using the MTMF method first on the f110512t01p00r07 image subset then on the f110512t01p00r08 flight log subset. Figure 30 shows one of the endmember infeasibility images along with the resulting analysis using the scatterplot of infeasibility verses MF score. In this case, the endmember used is the spectrum of a moderate use dirt road leading into a camp at the Mazourka Canyon site that has been input into the f110512t01p00r07 flight log data. Infeasibility images show the highest value pixels, and therefore the least feasible mixture of the target and background, as the brightest. There are a few dirt roads visible in the true color imagery that appear in the infeasibility image with scores of 5–10. These scores are close enough to zero (zero being a perfect match) to confirm the target material, especially since the brightest materials have scores of 30–100 (not feasible mixtures of background and target material). Using this information with a scatterplot analysis, only sections with very low infeasibility (around 0–6) scores and an MF score of 10–25 were selected (Figure 30, inset A). The result was very few pixels being highlighted, and those that were had an MF of .11 or 11%.

While this is lower than the hoped for 15–60%, comparison of the imagery to higher spatial resolution Google Earth imagery shows that there do seem to be trails in most of the areas that were marked. Other areas with higher MF scores between 15 and 25 also yielded positive results for trails not readily seen in the imagery, but also had some false positives.
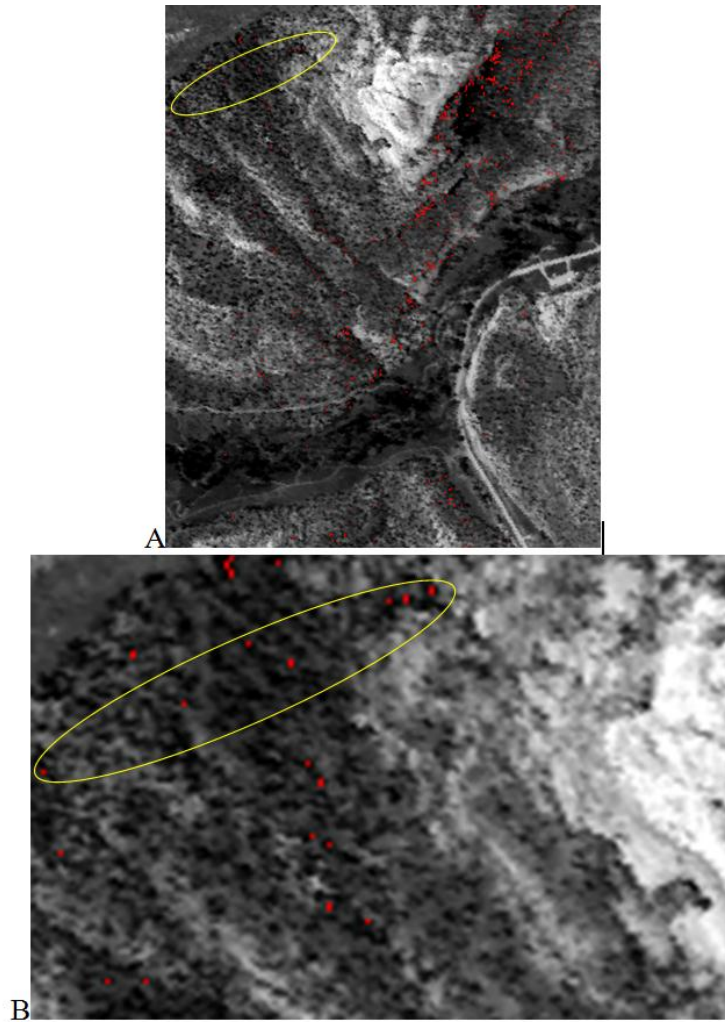
Figure 30. The above figure shows the MF verses Infeasibility scatter plot for the camp road endmember result plotted on a grayscale image of the f110512t01p00r07 data set with B being the zoomed in version of A. Red pixels represent target material with MF scores between 10 and 49%. The NE to SW trending pixels are thought to be a trail and have MF scores of 11–12%, the NW to SE trending pixels are along a drainage and have MF scores of 16–22% but may still be trail material.

The false positives were typically associated with bare rock drainages in the imagery when they had an MF score between 16 and 25 though values of this range were also associated with what appeared to be trails. Pixels with MF scores for this endmember that represented greater than 25% of the pixel were always associated with bare lithified rock features, typically steeply sloped and unlikely to harbor any trails due to terrain. When the camp road endmember was run on the second data set, similar results were obtained. Figure 31 shows results of the camp road endmember for both the 3.0 m pixel resolution data set (f110512t01p00r08) (inset A) and the 15.2 m pixel resolution data set (inset B).

The higher resolution image had positive matches for target material at 9–11%, very similar to the results of the f110512t01p00r07 data set, and the latter (f110623t01p00r10) had positive matches at 4–9% target material (Figure 31).
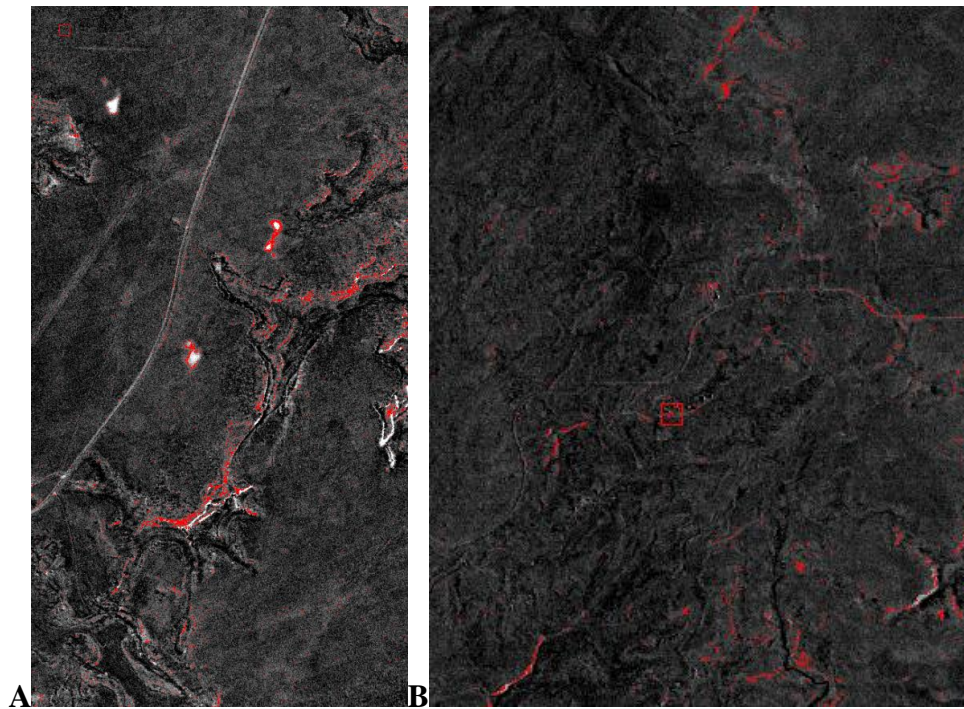
Figure 31.   This image shows the camp road endmember MF verses infeasibility image for the f110512t01p00r08 (A) andf110623t01p00r10 (B) data sets. The result is similar to that of the camp road endmember in the f110512t01p00r07 in that the target material identified as road had between 9 and 11% target fill in the pixel for A and 4 to 9% for B.

While the lower value would initially seem a setback, remember a larger pixel size means the same feature will occupy a smaller percentage of the pixel so this result is actually within the predicted range. As Figure 31 illustrates, the results were actually better with the larger resolution image for this particular endmember. Upon inspection of Google Earth imagery of the site, dirt sides of a paved road, what looked like ridgeline trails, dirt roads, dirt parking areas, and what appear to be ATV roads that look like drainages in the actual data set all had positive matches to the target material ranging from 4–9%.

2. Adjacent to Tread Endmember

The adjacent to tread endmember collect also yielded the close to expected results. Areas with the MF scores between 7 and 49 (49 was the highest yielded percentage value) are shown in red (Figure 32).
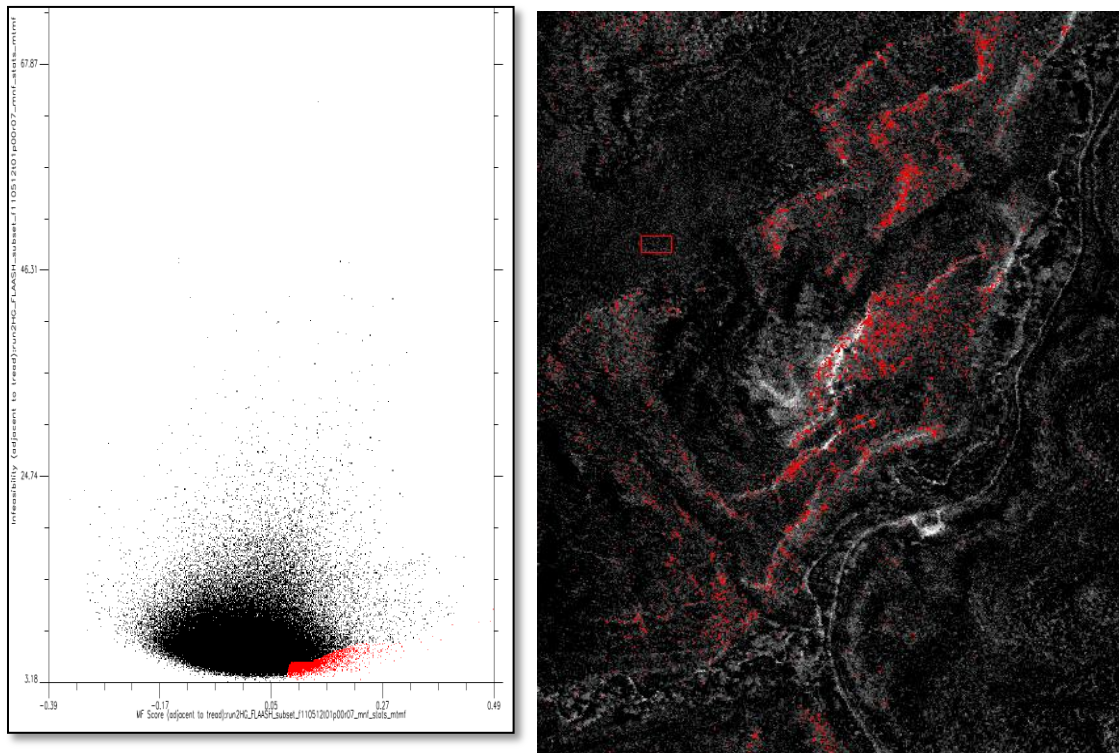
Figure 32. The image shows the MF vs infeasibility scatterplot and target material image of the user supplied adjacent to tread endmember in the f110512t01p00r07 data set. Detected target material corresponds with red areas (regions with highest MF score and lowest infeasibility) suggesting they are the best matches.

The target material shows up in various regions associated with what appears to be steeper terrain and the sides of drainages where unconsolidated material often appears; corresponding to the conditions of the material during collection. This endmember was given a slightly different margin for MF and infeasibility scores (closer to 5 and 10, respectively) because unconsolidated material is expected to be mixed with other material such as vegetation and different mineral mixtures. Therefore, you would expect the pixel percentages to potentially be lower.

For the repeatability test, the f110512t01p00r08 data set also had positive matches to targets. In this test, however, there were significantly fewer pixels identified with feasible mixtures (Figure 33). Since there were so few pixels identified under the standard ranges, the scatter plot class was increased to encompass MF scores to 52 (the highest possible range, and as low as 5. Even then most of the pixels were concentrated in certain areas rather than distributed throughout the imagery as seen in the f110512t01p00r07 data set. This is a good result however, considering the terrain is very flat in most of this image. Areas where the endmember corresponds to flat areas appear to be areas of runoff in both the imagery and looking at Google Earth. The high concentrations of areas determined to be target material are again associated with regions of steep terrain where you would expect loosely consolidated material. The majority of those regions are located, in most instances, around the edges of the landscape features depicted in Figure 33. These main imagery features appear to be highly lithified rock structures in the imagery and are confirmed as such to the greatest possible extent using Google Earth. The areas where the target material has been identified do appear to be steeper regions with less consolidated surface material as well as deposits at the base of the structures.
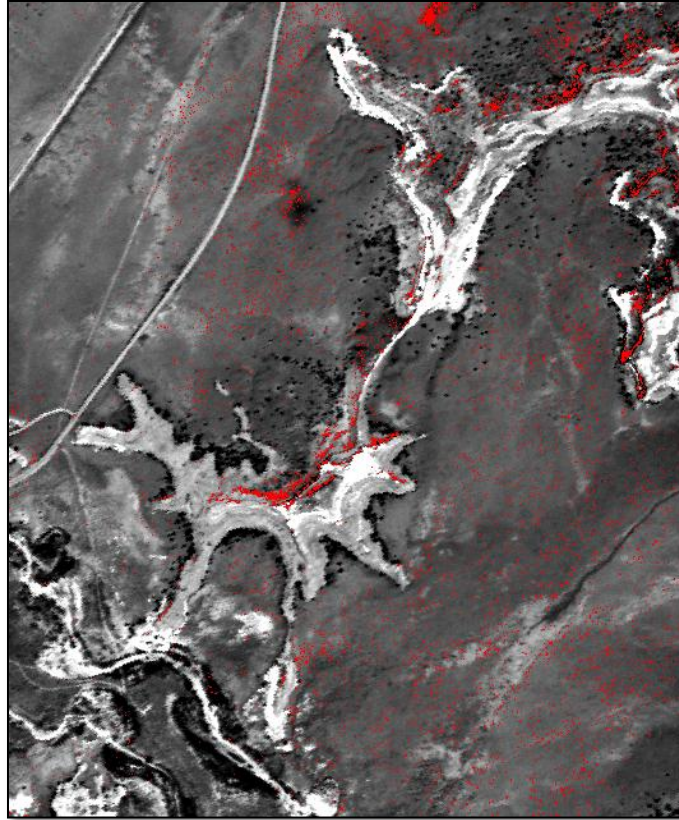
Figure 33.   This figure shows the adjacent to tread endmember results with MF scores of 5–52% using the f110512t01p00r08 for a repeatability test. Areas of highest target material concentrations are associated with regions of unconsolidated material on steep sides of lithified rock structures. Areas surrounding the rock structures are thought to have less target material because they are flat and may be more settled.

3.   Biological Soil Crust Endmembers

BSCs yielded results with similar value ranges to other endmembers of 9–11% in most cases. Some areas yielded smaller values closer to 5–7%. To test BSCs, imagery-derived endmembers, following the parameters of Weber et al (2008), had to be identified. This meant first identifying imagery derived endmembers as BSCs using the absorption feature seen around 650 nm in continuum removed spectra not present in bare soils (Weber et al., 2008). Most of the endmembers corresponded to vegetation and soils,

but there were a few that looked plausible. Endmembers 2, 3, and 32 (BSC 2, BSC 3, and BSC 1 in Figure 34, respectively) seemed the most likely candidates when inspected using the continuum removed method.
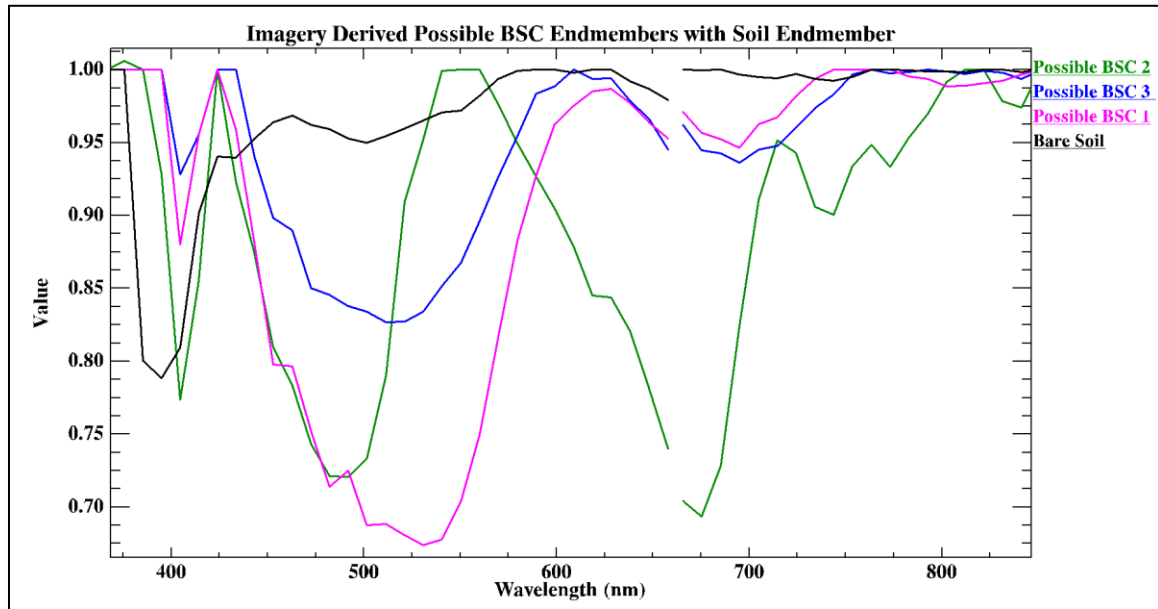
Figure 34.   This figure is the spectra for three imagery derived mean class endmembers thought to be BSCs and the spectrum for an endmember believed to be soil based on criteria established previously from Weber et al (2008) and the results of the spectral libraries with the continuum removed function showing an absorption feature at ~650 nm not seen in soil (Figure 25).

The endmembers chosen for BSC candidates showed shallower absorption features than vegetation endmembers that were slightly offset from the vegetation absorption feature near 650–700 nm. Endmember 14 is thought to be bare soil, though there may be a BSC or vegetation component there as well due to a slight absorption feature also around 700 nm; though it is much shallower and a different shape. Once the endmembers were determined they were scatter plotted as MF verses infeasibility to see how they were distributed within the imagery and what MF scores would be associated with the most likely matches. The result of this can be seen in Figure 35 A and B.

The collected endmembers from Mazourka Canyon were then scatter plotted in the same image data set as the imagery derived ones and analyzed (Figure 35 C and D).

Inset C of Figure 35 is the same data set (f110512t01p00r07) utilized with the imagery derived BSC endmembers in Figure 35, inset A and B. Inset D of Figure 35 is the f110512t01p00r08 data set result using the same endmember as in inset C for a repeatability test. While the healthy BSC result using the imagery derived endmember (Figure 35, inset A) was not repeatable using any of the ASD collected BSC endmembers, the disturbed BSC endmember results did appear to be replicable to the imagery derived ones with 7–11% providing the best result range in the f110512t01p00r07 data set. Similar results for the f110512t01p00r08 data set of 5–9% yielding the best range for the disturbed BSC endmember were obtained.

Slightly different results are expected as the resolution of the two images is close but not exact. Figure 35, inset D shows the result for the f110512t01p00r08 data set. BSC results are, however, somewhat inconclusive as they appear in high concentrations in areas that other endmembers have also been detected, particularly the adjacent to tread endmember. The distribution of the BSC pixels did look slightly different, and there is no reason they could not occur in the same location, as BSCs tend to also cause soil to become more consolidated via their growth method and are known to be a stabilizing mechanism of slope material (Johnston, 1997).
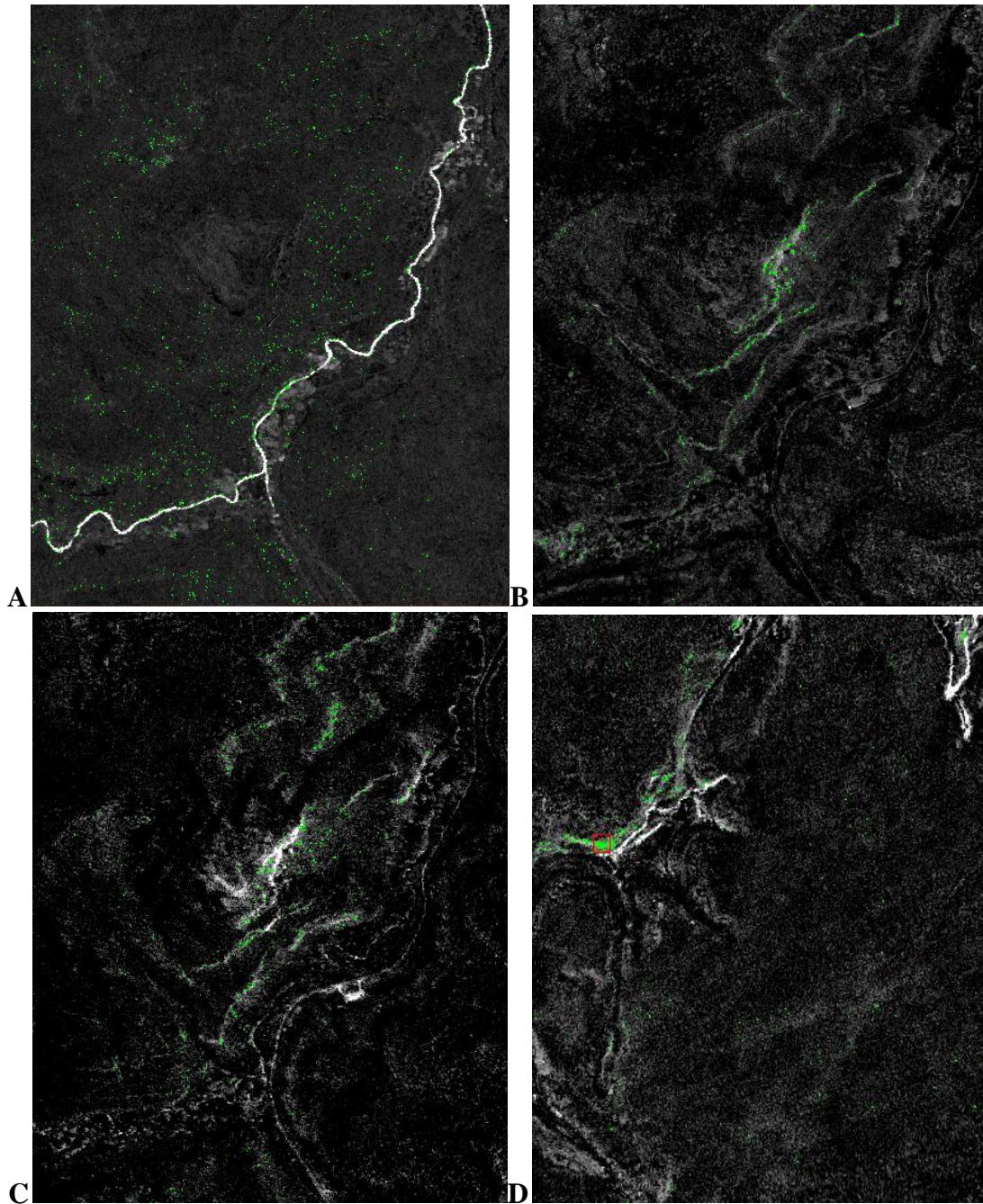
Figure 35.   A shows results using BSC endmember 2 derived from the imagery. B and
             C show areas suspected to contain BSCs using endmember 3 and the
             Mazourka Canyon disturbed BSCs in green. While B and C show similar
             results, the results of A were not repeatable with the collected BSC
             endmembers. D shows the results from the repeatability test using the same
             endmember as in C. In all cases, the range was between 9–11% for target
             material, with higher values of 15–30% associated with possible bare to
             nearly bare soil.

However, the presences of BSCs are much more difficult to determine even utilizing Google Earth for virtual ground-truthing; the resolution is just not good enough to make a positive determination. Also, the expectation was that BSCs would be found in higher concentrations but the lack of large swaths of target material does not support this assumption, indicating that either there is minimal to no presence of BSCs or the spectra are not unique enough to be differentiated from the soil.

### 4.	Disturbed Creek Soil Endmember

While the majority of this analysis focuses on the two data sets with the highest resolution, the lack of a substantial creek feature in the f110512t01p00r08 data set made it necessary to use the lower resolution 15.2 m pixel f110623t01p00r10 data set. Fortunately this larger data set had several creek features that could be analyzed using the disturbed creek soil endmember for a repeatability test. Figure 36, insets A-C show the results, which are somewhat similar to the camp road endmember in the initial f110512t01p00r07 data set (Figure 36, inset A-C). However, the f110623t01p00r10 results were quite different than the camp road endmember (Figure 37). Similarly to other results, the best identifications of target material are consistently within ranges between 9-16% with increasingly greater false positives for larger percentage pixel contributions.
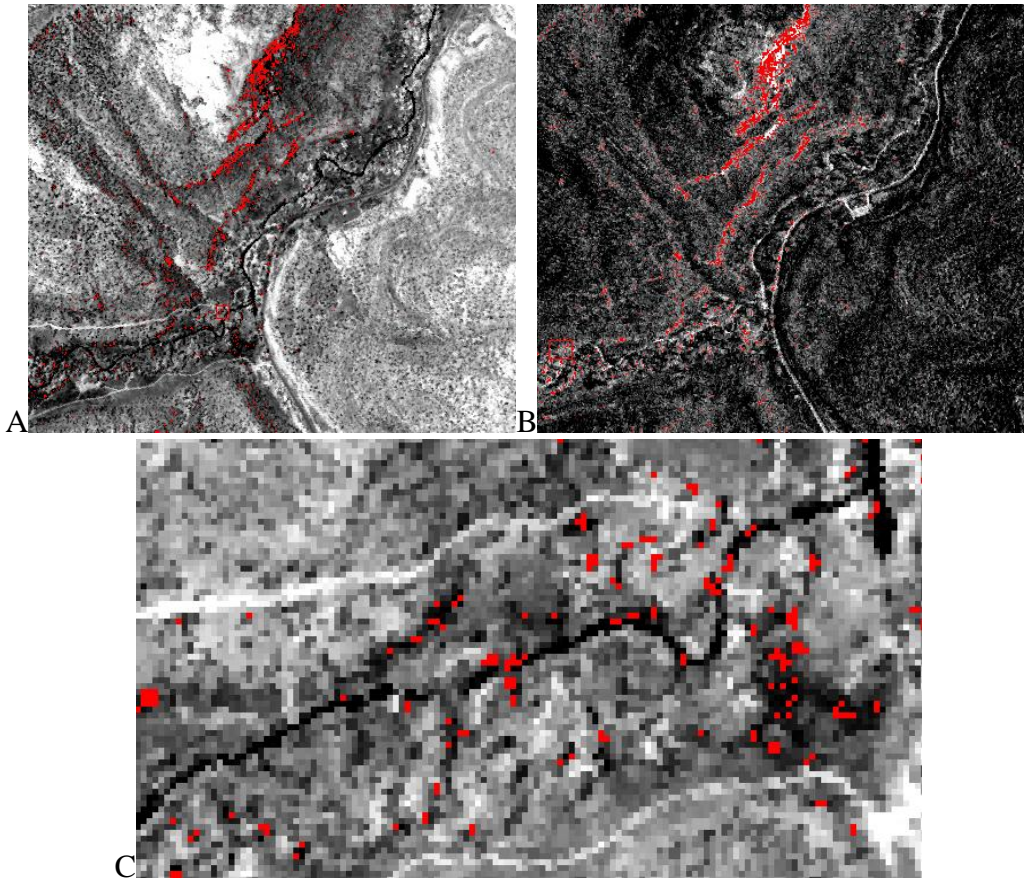
Figure 36.   A and B are the results from the initial f110512t01p00r07 data set overlain on a gray scale image and in the MF verses infeasibility class scatterplot results, respectively. C shows a zoomed in portion of the creek area with red pixels representing the disturbed creek soil endmember in the f110512t01p00r07 data set. Pixel percentages range from 9-37% with the best matches falling between 9 and 16%.

The repeatability test seemed to yield much more accurate results with the lower resolution image. The results were between 5 and 11 % which at first seems low, but remembering that the resolution is 15.2 m per pixel, even large features are expected to occupy lower percentages of pixels. Red pixel areas correspond to what appeared to be creek drainages with potential oxbow lakes (Figure 37, inset A and C), but upon looking at Google Earth for virtual ground-truthing, most of these pixels are associated with ATV trails within the drainages (Figure 37, inset B). This is a very good result as the endmember was collected from ATV trails along creek drainages in Mazourka Canyon.
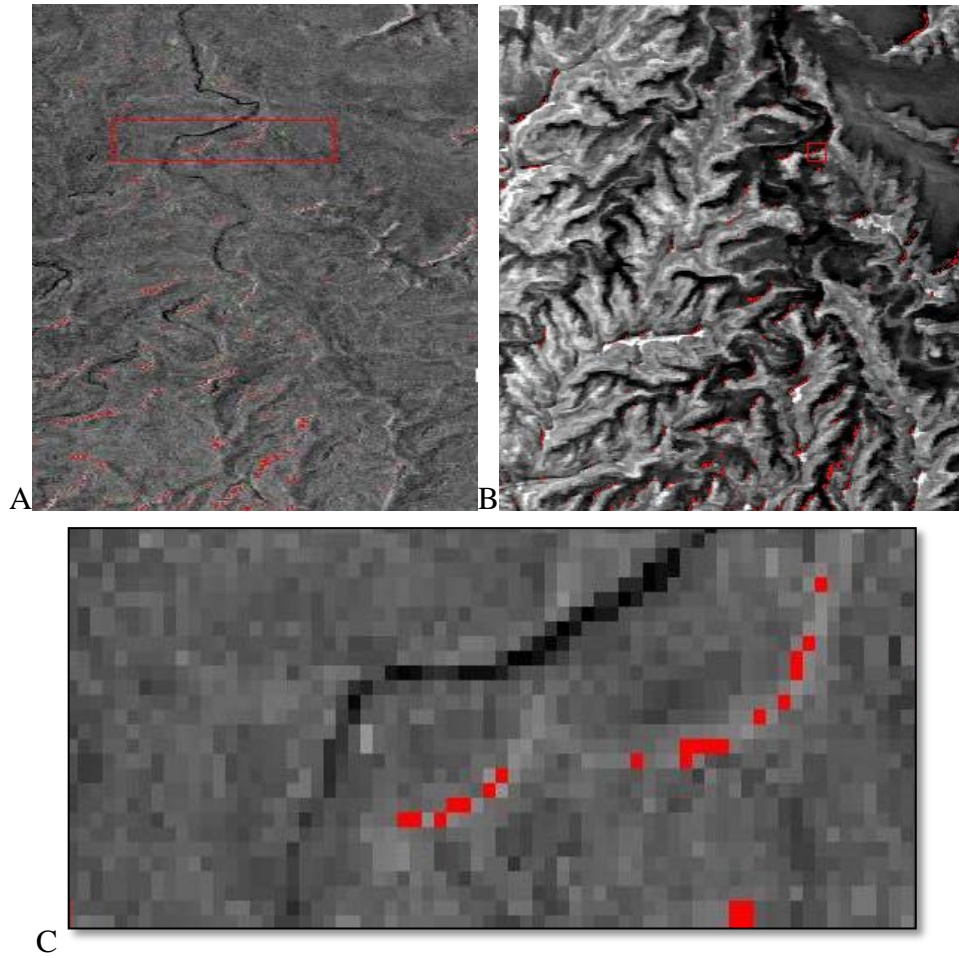
Figure 37.   Inset A shows the image result of the MTMF analysis for the disturbed creek soil endmember in the f110623t01p00r10 data set. As expected, this endmember shows up in areas that look like dry creek beds and along river banks. Inset B shows the gray scale image with the results overlain, and Inset C shows a concentration of endmember containing pixels corresponding to the area in the red box in A. The red pixels are not only in creek drainages, but looking at Google Earth; these drainages also contain ATV trails. In most cases, the red pixels are associated with the ATV trails, some not readily apparent in the imagery.

5.   Color Composites of Endmembers

A final test of the endmembers was to look at them as color composites enhanced to emphasize the endmember being investigated. The best results were when a user supplied (ASD measured) endmember was put into a composite (R, G, B space) with two imagery derived endmembers. Figure 38, insets A and B illustrate the creek soil and

72

camp road endmembers, respectively. Figure 38, inset C shows a color composite of the atmospherically corrected imagery from the f110512t01p00r07 data set. The image colors were chosen to enhance different surface materials in the image to makes sure the endmembers were accurately identifying potential target material, particularly in the creek areas where there are significant quantities of vegetation (shown as red in inset C of Figure 38).

The composites illustrate both the successes and failures of the endmembers, yet still seem to do the job of identifying the types of features being looked for based only on changes in spectra related to surface disturbances supplied by the ASD collected endmembers. In the color composites, the brightest pixels are associated with the largest percentage values, typically around 20%. These were generally associated as false positives, while the more muted pixels corresponded to lower ranges between 9 and 18% and were the most accurately identified pixels, as far as trail like features are concerned. Many of the endmembers yielded similar results but with higher concentrations in areas associated with the type of region the samples were collected from. For example, the disturbed creek soil endmember had more successes and higher positive matches in areas where creeks and drainage basins were found.
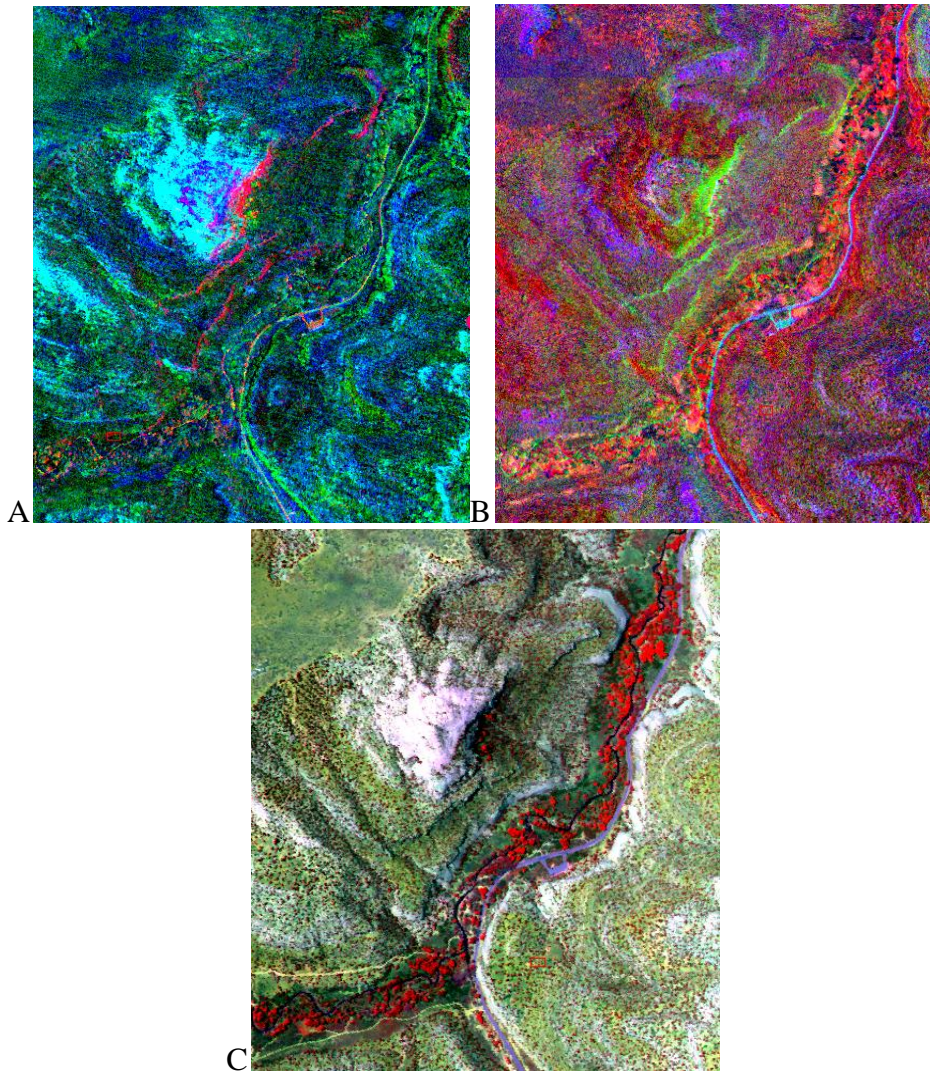
Figure 38.   Inset A shows a color composite result using the ASD measured camp road endmember and 2 imagery derived endmembers for RGB color composite. Red pixels represent the camp road material. Inset B shows a color composite using an imagery derived endmember, the ASD measured camp road endmember, and another imagery derived endmember for R, G, B, respectively with green pixels representing target material. The potential trail identified with this endmember in Figure 29 shows up in green here, and is particularly noticeable as an s shape closer to the creek. With both ASD measured endmembers, the most accurate results were in the range of 9-18% pixel fill. Higher than 18% resulted in some matches and some false positives with lithified rock faces. Inset C shows an example of a color composite of the actual imagery with band combinations highlighting specific image elements. This was to help verify target material was accurately identified in the color composites depicted in A and B.

VII. DISCUSSION AND CONCLUSIONS

A. SPECTRAL MEASUREMENTS AND SOIL DISTURBANCE

Analysis of the collected spectral libraries established that there were measurable differences between spectra of disturbed versus undisturbed areas of the same composition materials. Endmembers collected in the field were all categorized by a material first undisturbed and then disturbed from the same location. The disturbances were all caused by impact-related use such as walking, driving over, or dropping something onto the soil, OHV and equestrian use (horses). Firerelated disturbances were also used in order to have information regarding camp fires to help associate the source as anthropogenic. For the initial clay collection the samples were all taken from the same area and spanned a section of roughly 1.62 Km^2. The continuum removed spectral differences occur in the wavelength regions of approximately 500 nm, 1200 nm, and 2200 nm. The changes observed at these wavelengths involve differences in apparent reflectance received at the sensor and calculated differences in band depth and observable width differences of absorption features in the same material. Similarities in the amount of difference in depths between ASD collected endmembers and imagery derived endmembers suggested that these differences made the spectra unique enough to be successfully used to detect features such as trails based on differences in spectral characteristics.

Clearly properties of soils are altered once they have been exposed to some surface disturbance, particularly those caused by impacts. It is the chemical and structural make-up of soil that causes it to exhibit its characteristic absorption feature. Previous studies have found similar changes in reflectance and spectra shape, depth, and width of vegetation exposed to gasses injected into soils. These changes were the result of a stress response by vegetation to the gasses as a function of distance from the source. It makes sense then that if reflectance changes in vegetation are a response to an ecosystem disturbance, then the reflectance changes in this study can be correlated to anthropogenically caused surface disturbances as well. The data shown in this report support this line of thinking because the changes in reflectance are similar enough to the

differences in the studies by other researchers to suggest that they too can be correlated with some sort of functional disruption. Supporting evidence of spectral alteration due to impact was determined between ASD collected undisturbed BSC spectra and BSC spectra associated with trampling. Because the endmembers are soils and biological soil components that are confirmed to have undergone impact-related surface disturbances, then it is reasonable to think the differences in reflectance are related to impact-related changes in the soil.

B.   INFEASIBILITY AND MF SCORES

For comparison purposes, both imagery derived and field-measured endmembers were used in the MTMF analysis. The idea behind this was to determine if the measured endmembers could achieve similar success results to the imagery derived ones for identifying disturbance-related changes in reflectance. If so, then it could be said that user supplied endmembers from geologically similar areas would be a successful way of tracking disturbances in imagery from a geographically different area. Imagery derived endmembers and user supplied ones were evaluated by continuum removed changes in band depth, and results indicate that these differences are similar to those collected in the field. The similarities in calculated band depths associated with absorption features at 500 nm, 1125 nm, and 2200 nm allowed for the postulation that if the results using the user supplied endmembers were similar to those achieved with the imagery derived endmembers for similar types of materials (soils and BSCs), then the test could be considered successful. The MF and Infeasibility scores obtained for the measured endmembers were, for the most part, as successful as the imagery derived endmembers.

Because the measured endmembers come from areas that are different than the location of the imagery data, a perfect match was not expected and the percentage rate for successful detection was set at a lower value than those of the imagery derived endmembers. The idea here was to have the results yield a low enough infeasibility number that one could reasonably assume what you were looking at was some mixture of that endmember and the background. The camp road endmembers are a good example of this at work. While not a perfect match, the infeasibility score of between 6 and 10

allows for reasonable certainty that the linear feature depicted is a dirt road because it is close to zero, with zero indicating a perfect match to the target material. Also, the fact that the second imagery data set yielded a result of 5–10 is significant; because not only is the endmember from a geographically different area, but the two images are also from geographically different parts of the Canyonlands area. The two images yielding such similar results is a sign of both successful use of the endmember to find roads/trails, but also that it can be used with similar success rates in different areas. Not only that, but we know that these infeasibility scores do accurately identify dirt roads because each image has at least one that can be confirmed as such within the true color imagery. The roads/trails were identified with these scores and the data sets have been compared to Google Earth for virtual ground-truthing.

The adjacent to tread endmember performed well in areas associated with steep terrain and is likely associated with poorly consolidated material. This is a promising result because this particular spectra was collected on an unconsolidated hill side with a moderate slope angle of around 15^0–20^0. When looking at the red colored target material distribution, you can begin to make out what looks like topography. Comparing the material distribution image to the true color imagery, the NW to SE trending features are drainages in the true color image. Other features that can be seen with the target material in the NE corner, these are steep curving slopes in the true color image.

One area that did not quite yield the anticipated results was the use of BSCs as endmembers. While pixels with a reasonable percentage level were detected, there were so few of them that it is hard to say without ground-truthing that these areas legitimately contained BSCs. Potentially, the reason for this is twofold. On the one hand, the concentration of BSCs in the field collected spectra from Mazourka Canyon were not heavily concentrated and therefore contained more of the soil spectra with a minimal peak in the green portion of the spectrum (500 nm) making them not spectrally significant enough to show up en masse in the data sets. The other issue may have been a resolution problem. BSCs were expected to occupy larger swaths of imagery if present, even with a resolution of approximately 3 m pixels in both the f110512t01p00r07 and f110512t01p00r08 data sets. If present in the imagery, they may well have been in very

small concentrations making them un-useful for target detection. If, however, higher resolution imagery were available it may still prove to be a useful target based on the fact that positive hits were detected and BSCs were found to exhibit similar changes in spectral characteristics as soils when exposed to impact-related surface disturbances.

What seems, at this point to be the most successful test, was the disturbed creek soil endmember in the f110623t01p00r10 data set. This was a bit of a surprise because the expectation was that the higher resolution imagery would be more successful which is why it was utilized for both the initial and repeatability tests. The lower resolution imagery was only utilized when results in the repeatability test were too inconclusive to be considered a valid test and further testing was required. The fact that the f110512t01p00r08 data set was not successful and the f110623t01p00r10 was can also serve as a positive reflection on the test. The issue was that the distribution of positively identified pixels was confined to steep slopes for the most part with a few in what looked like runoff areas in the higher resolution data set.

This could mean that the circumstances creating the spectral characteristics specific to the disturbed creek endmember were not present in the imagery. This theory is further supported by the lack of a substantial creek feature within the 110512t01p00r08 imagery. The f110623t01p00r10 data set however, had several features that appeared to be drainage basins. The result was significant successful identification of areas that appear to be drainage basins with OHV trails in them not always visible in the imagery. In almost every case, a pixel with a value between 5-11% was a positive match to an area with an OHV trail or a drainage basin. While 5-11% seems a lower range than other data sets, one must remember to take into account the fact that a larger pixel size means similar features will take up less of a percentage than in smaller pixels. The positive identification range is consistent with the expected percentage of a pixel that a trail/OHV route should occupy.

C.   COLOR COMPOSITES

Color composites using the user supplied endmembers in conjunction with imagery derived endmembers provided useful results. While the composites illustrate

potential failures in endmember ability to accurately identify target material beyond a certain threshold, they also illustrate the success of these endmembers in identifying features such as trails. Use of the color composites filled in gaps between pixels that were difficult to correlate alone, such as s shaped feature seen in Google Earth. This feature did appear to be part of a trail that continues up a ridgeline and around the back side of the peak identified by the camp road endmember. These color composites serve as an example of the potential for this method in identifying features not readily seen in true color satellite imagery.

D.   FUTURE WORK

Given more time, further work on this topic should include going to the imagery flight locations to physically ground truth the MTMF results and trying the experiment again on other types of available Hyperspectral imagery. Hyperspectral systems of interest would be those covering a 380-2500 nm wavelength range, and higher spatial resolution if possible. Lower resolution imagery should also be explored due to the surprising success using the disturbed creek soil endmember in the f110623t01p00r10 data set. Studies utilizing BSC spectral changes should also be further explored. Endmembers for BSCs from areas with higher concentrations of the organisms should be collected as well as those with better species matches to the areas under analysis.

While the California collection sites were chosen to be as close to the Colorado sites as possible, there are other areas outside of California that have soil components more closely matched to the Colorado locations. Spectral libraries from other similar locations to the study sites should be collected and tested. Libraries should also be collected from the actual study areas while ground-truthing. The same analysis should be run with site spectra and compared to the California endmember results to test for accuracy. This could also serve in developing a difference threshold between collection and imagery sites that would still allow for successful target material identification. Another potential area of study is the amount of variation in feature depths as a response to disturbances. The amount of variation across a given soil component may help in establishing a baseline to judge how much/what type of disturbance has occurred in the

area making it possible to tell what type of traffic has come through the area.   This could potentially be useful when selecting the best possible endmembers from a library to use in analysis for a given type of disturbance.

LIST OF REFERENCES

Allaby, M., Anderson, R., and Crofton, I., (2011). *Deserts and Semideserts.* Chicago, IL: Heinemann-Raintree,.

Asner, G.P., and Heidebrecht, K.B., (2002). Spectral unmixing of vegetation, soil and dry carbon cover in arid regions: Comparing multispectral and hyperspectral observations. *International Journal of Remote Sensing*, 23(19), 3939–3958.

Asner, G.P., and Lobell, D. B., (2000).   A biogeophysical approach for automated SWIR unmixing of soils and vegetation. *Remote Sensing of Environment*, 74, 99–112.

Balba, A. M., (1995). *Management of problem soils in arid ecosystems.* Boca Raton, FL: CRC Press, 13-18.

Ben-Dor, E., Goldlshleger, N., Benyamini, Y., Agassi, M., and Blumberg, D.G., (2003). The spectral reflectance properties of soil structural crusts in the 1.2 to 2.5 μm spectral region. *Soil Society of America* Journal, 67 (1), 289–299.

Bernstein, L.S., Jin, X., Gregor, B., and Adler-Golden, S.M., (2012). Quick atmospheric correction code: algorithm description and recent upgrades. *Optical engineering,* 51 (11), 111719-1–111719-11.

Birvio, P.A., Giardino, C., Zilioli, E., (2001). Validation of satellite data for quality assurance in lake monitoring applications. *Science of The Total Environment*, 268 (1-3), 3–18.

Boardman, J.W., and Kruse, F.A., (2011). Analysis of imaging spectrometer data using N-dimensional geometry and a mixture-tuned matched filtering approach. *IEEE Transactions on Geoscience and Remote Sensing*, 49 (11), 4138–4152.

Bowker, M. A., Belnap, J., Davidson, D. W., and Phillips, S. L., (2005). Evidence for micronutrient limitation of biological soil crusts: Importance to arid-lands restoration. *Ecological Applications*, 15(6), 1941–1951. doi: 10.1890/04-1959

Bursik, M., and Sieh, K., (1989). Range Faulting and Volcanism in the Mono Basin, eastern California. *Journal of Geophysical Research,* 94 (B11), 15, 587–15, 609.

Collins, B. H., Olsen, R C., and Hackwell, J., (1997). Thermal imagery spectral Analysis. *SPIE,* 3118, 0277-786x.

Clark, R.N., (1999). Spectroscopy of rocks and minerals, and principles of spectroscopy. In *Manual of Remote Sensing, Volume 3, Remote Sensing for the Earth Sciences,* (A.N. Rencz ed.), New York, NY: John Wiley and Sons, 3–58.

Clark, R. N., Swayze, G. A., Livo, K. E., et al., (2003). Imaging spectroscopy: Earth and planetary remote sensing with the USGS Tetracorder and expert systems. *Journal of Geophysical Research,* 108 (E12), 5131. doi: 10.1029/2002JE001847

Clark, R. N., and Roush, T. L., (1984). Reflectance spectroscopy-Quantitative analysis techniques for remote sensing applications. *Journal of Geophysical Research,* 89 (NB7), 6329-6340. doi: 10.1029/JB089iB07p06329

Curran, P. J., Dungan, J. L., and Peterson, D. L., (2001), "Estimating the foliar biochemical concentration of leaves with reflectance spectrometry; testing the Kokaly and Clark methodologies," *Remote Sensing of Environment,* 76 (3), 349–359. doi: 10.1016/s0034-4257(01)00182-1

Davis, A., (2007). *The use of commercial remote sensing in predicting helicopter brownout conditions.* Master's Thesis Naval Posgraduate School, Monterey, CA, 1-72.

Dunne, G. C., and Walker, J. D., (1993). Age of Jurassic volcanism and tectonism, southern Owens Valley region, east-central California. *Geological Society of America Bulletin*, 105, 1223–1230.

Dunne, G.C., Garvey, T.P., Oborn, M., Schneidereit, D., Fritsche, A.E., and Walker, J.D., (1998). Geology of the Inyo Mountains Volcanic Complex: Implications for Jurassic paleogeography of the Sierran magmatic arc in eastern California. *Geological Society of America Bulletin*, Part II, 92, 1–38.

Elachi, C. and van Zyl, J., (2006). *Introduction to the physics and techniques of remote sensing*. Hoboken NJ: Jon Wiley & Sons.

Evans, R.D., and Belnap, J., (1999). Long-term consequences of disturbance on nitrogen dynamics in an arid Ecosystem. *Ecology*, 80 (1), 150–160.

Gao, B. and Goetz, A. F. H., (1990). Column atmospheric water vapor and vegetation liquid water retrievals airborne imaging spectrometer data. *Journal of Geophysical Research,* 95 (D4), 3549–3564.

Gathercole, G. R., (1987). Earth observation science and applications. *The Geographical Journal*, 153 (3), 319–326.

Goetz, A. F. H., and Rowan, L. C., (1981). Geologic remote sensing. *Science*, 211 (4484), 781–791.

Goetz, A. F. H., Vane, G., Solomon, J. E., and Rock, B. N., (1985). Imaging spectrometry for Earth remote sensing. *Science*, 228 (4704), 1147–1153.

Green, A. A., Berman, P. S., and Craig, M. D., (1988). A transformation for ordering multispectral data in terms of image quality with implications for noise removal. *IEEE Trans. Geosci. Remote Sens.*, 26 (1), 65–74.

Green, R.O., Eastwood, M. L., and Sarture, C. M., (1998). Imaging spectroscopy and the Airborne Visible Imaging Spectrometer (AVIRIS). *Remote Sensing of the Environment*, 65 (3), 227–248.

Haboudane, D.; Tremblay, N.; Miller, J. R.; Vigneault, P., (2008). Remote Estimation of Crop Chlorophyll Content Using Spectral Indices Derived From HyperspectralData. *IEEE Transactions on Geoscience and Remote Sensing,* 56 (2), 423–437.

Halvatzis, A. G., (2002). *Passive detection of gases in the atmosphere. Case Study: Remote sensing of SO2 in the UV using LINUS*. Master's thesis, Naval Postgraduate School.

Jensen, J. R., (1983). Biophysical remote sensing. *Annals of the Association of American Geographers*, 3 (1), 111–132.

Jensen, J. R., (2007). *Remote Sensing of the Environment: An Earth Resource Perspective (2nd ed)*. Upper Saddle River, NJ: Prentice Hall, 355-402, 507–566.

Johnston, R., (1997), " Introduction to microbiotic crusts," *United States Department of Agriculture Natural Resouces Conservation Service*, 1-16.http://soils.usda.gov/sqi/management/files/micro_crusts.pdf

Jonasson, S., Callaghan, T. V., Shaver, G. R., and Nielsen, L. A., (2000). Arctic terrestrial ecosystems and ecosystem function. In *The Arctic: Environment, People, Policy* (Nuttall and Callaghan eds.). Amsterdam, The Netherlands: Harwood Academic Publishers, 275-314.

Kokaly, R.F., and Clark, R.N., (1999). Spectroscopic determination of leaf biochemistry using band-depth analysis of absorption features and stepwise multiple linear regression. *Remote Sensing of Environment,* 67, 267–287.

Kokaly, R.F., (2001). Investigating a physical basis for spectroscopic estimates of leaf nitrogen concentration. *Remote Sensing of Environment,* 75, 153–161.

Kruse, F. A., (1988). Use of Airborne Imaging Spectrometer data to map minerals associated with hydrothermally altered rocks in the northern Grapevine Mountains, Nevada and California. *Remote Sensing of Environment,* 24 (1), 31-51.

Kruse, F. A., Boardman, J. W., and Lefkoff, A. B., (2000). Extraction of compositional information for   trafficability mapping from hyperspectral data. *Proceedings SPIE International Symposium on Aero Science*, 24 – 28 April 2000, Orlando, FL, 4049, 262–273.

 Kruse, F.A., Boardman, J.W., and Huntington, J.F., (2003). Comparison of airborne hyperspectral data and EO-1 Hyperion for mineral mapping. *IEEE Special Issue, Transactions on Geoscience and Remote Sensing (TGARS),* 41 (6), 1388–1400.

Kruse, F. A., Boardman, J. W., and Livo, K. E., (2004). Comparison of ATREM, ACORN, and FLAASH atmospheric corrections using low-altitude AVIRIS data of Boulder, Co. *13th JPL Airborne Geoscience Workshop, Jet Propulsion Laboratory*, 31 March – 2 April 2004, Pasadena, CA, JPL Publication 05-3, at: ftp://popo.jpl.nasa.gov/pub/docs/workshops/04_docs/Kruse-JPL2004_Boulder_Urban.pdf

Kruse, F.A., (2012). Mapping surface mineralogy using imaging spectrometry. *Geomorphology*, 137 (1), 41–56.

Kruse, F. A., (2008). Expert system analysis of hyperspectral data. *Proceedings, SPIE Defense and Security, Algorithms and Technologies for Multispectral, Hyperspectral, and Ultraspectral Imagery XIV, The International Society for Optical Engineering (SPIE),* 6966, 69660Q-1-69660Q-12.

Kruse, F. A. and Perry, S. L., (2009). Improving multispectral mapping by spectral modeling with hyperspectral signatures. *Journal of Applied Remote Sensing,* Volume 3, 033504.

 Kruse, F. A., Taranik, J. V., Coolbaugh, M., Michaels, J., Littlefield, E. F., Calvin, W. M., and Martini, B. A., (2011). Effect of reduced spatial resolution on mineral mapping using imaging spectrometry-Examples using hyperspectral infrared imager (HyspIRI)-Simulated Data. *Remote Sensing,* 3, 1584–1602.

Dr. Lammers, D. A. (1991). *Soil Survey of Canyonlands Area, Utah, Parts of Grand and San Juan Counties.* United States Department of Agriculture, Soil Conservation Service.

Manolakis, D., Marden, D., and Shaw, G. A., (2003). Hyperspectral image processing for automatic target detection applications. *Lincoln Laboratory Journal*, 14 (1), 79–116.

McKinney, M. L., Schoch, R. M., and Yonavjak, L., (2013). *Environmental Science, Systems and Solutions(5th ed).* Burlington, MA: Jones and Bartlett, 113-124.

Merriam, C. M., (1973). Silurian rugose corals of the central and southwest Great Basin. *Geological Survey Professional Paper 777*, United States Government Printing Office, Washington D.C.

[online] blm.gov, Milliken, M., Saint-Amand, P., Saint-Amand, D., (2007).   Roadside
geology and Mining History Owens Valley and Mono Basin. *U.S. Bureau of
Land Management*.
http://www.blm.gov/pgdata/etc/medialib/blm/ca/pdf/bakersfield/geology.Par.5633
2.File.dat/ovm07_guidebook.pdf

Moore, T. R., (1978). Soil formation in northeastern Canada. *Annals of the Association
of American Geographers,* 68 (4), 518-534.

Mustard, J. F., Murchie, S.L., et al, (2008). Hydrated silicate minerals on Mars observed
by the Mars Reconnaissance Orbiter CRISM instrument. *Nature*, 454, 305–309.

Mutanga, O., Skidmore, A.K., and Prins, H.H.T. (2004). Predicting in situ pasture
quality in the Kruger National Park, South Africa, using continuum-removed
absorption features. *Remote Sensing of Environment,* 89, 393–408.

Nauman, J. C., Anderson, J. E., Young, D. R., (2008). Linking physiological responses,
chlorophyll Fluorescence and hyperspectral imagery to detect salinity stress using
the physiological reflectance index in the coastal shrub, Myricacerifera. *Remote
Sensing of Environment,* 112 (10), 3865–3875.

Noomen, M.F., Skidmore, A.K., van der Meer, F.D., and Prins, H.H.T., (2006).
Continuum removed band depth analysis for detecting the effects of natural gas,
methane and ethane on maize reflectance. *Remote Sensing of Environment,* 105,
262–270.

Olsen, C.E. Jr., (1979). Elements of image interpretation. *Supplementary Notes for the
University of Michigan School of Natural Resources Training Programs,* Ann
Arbor, MI., 1-88.   Retrieved from
www.ferris.edu/faculty/burtchr/gisc239/papers/vegetation%20remote%20se
nsing/Fundamentals/elements%20of%20image%20interpretation.pdf

Olsen, R.C., (2007). *Remote sensing from air and space*.   Bellingham, WA: SPIE-
International Society for Optical Engineering, 55–100.

O'Neill, A.L., (1994). Reflectance spectra of microphytic soil crusts in semi-arid
Australia. *International Journal of Remote Sensing,* 15 (3), 675–681.

 Prose, D., (1985). Persisting effects of armored military maneuvers on some soils of the
Mojave Desert. *Environmental Geology,* 7 (3), 163–170.

Roberts, D. A., and Herold, M., (2004). Imaging spectrometry of urban materials.
*Infrared Spectroscopy in geochemistry, Exploration and remote sensing, Mineral
Association of Canada, Short course series*, 33, 155–181.

Sharp, R. P., and Glazner, A. F., (1997). *Geology underfoot in Death Valley and Owens Valley*. Missoula, MT: Mountain Press Publishing.

Sieh, K., and Bursik, M., (1986). Most recent eruption of the Mono Craters, eastern central California. *Journal of Geophysical Research,* 91 (B12), 12,539-12,571.

Smith, K .L., Steven, M. D., and Colls, J. J., (2004). Use of hyperspectral derivative ratios in the red-edge region to identify plant stress responses to gas leaks. *Remote Sensing of Environment*, 92, 207–217.

Snow, J. K., and Wernicke, B. P., (2000). Cenozoic tectonism in the central Basin and Range: Magnitude, rate, and distribution of upper crustal strain. *American Journal of Science*, 300, 659–719.

Stevens, C.H., and Stone, P., (2007). The Pennsylvanian-early Permian Bird Spring carbonate shelf, southeastern California: Fusulinid biostratigraphy, paleogeographic evolution, and tectonic implications. *Geological Society of America Special Paper*, 429, 82.

Stone, P. and Stevens, C.H., (1998). Pennsylvanian and early Permian paleogeography of east-central California: Implications for the shape of the continental margin and the timing of continental truncation. *Geology*, 16, 330–333.

Stone, P., Swanson, B.J., Stevens, C.H., Dunne, G.C., and Priest, S.S., (2009). Geologic map of the southern Inyo Mountains and vicinity, Inyo County, California, *United States Department of the Interior US Geological Survey*, 1-20. Retrieved from http://pubs.usgs.gov/sim/3094/sim3094_pamphlet.pdf

Tallyn, E.F., Jr., (1996). Soil survey of Benton-Owens Valley Area, California, Parts of Inyo and Mono Counties. *United States Department of Agriculture, Natural Resources Conservation Service*.

Warhol, T., (2007). *Earth's Biomes: Desert.* Tarrytown, NY: Marshall Cavendish Benchmark, 63-69.

Webb, R.H., Fenstermaker, L.F., Heaton, J.S., Hughson, D.L., Mcdonald, E.V., and Miller, D.M., (2009). *The Mojave Desert: Ecosystem processes and sustainability*. Reno, NV: University of Nevada Press.

Weber, B., Olehowski, C., Knerr, T., Hill, J., Deutschewitz, K., Wessels, D.C.J., Eitel, B., Budel, B., (2008). A new approach for mapping of biological soil crusts in semi-desert areas with hyperspectral imagery. *Remote Sensing of Environment*, 112, 2187–2201.

Whitford, W.G., (2002). *Ecology of desert systems*. San Diego, CA: Elsevier Science Ltd., Academic Press.

Zhang, J., Rivard, B., (2005). Spectral unmixing of normalized reflectance data for the deconvolution of lichen and rock mixtures. *Remote Sensing of Environment*, 95 (1), 57–66.

INITIAL DISTRIBUTION LIST

1. Defense Technical Information Center
    Ft. Belvoir, Virginia

2. Dudley Knox Library
    Naval Postgraduate School
    Monterey, California

3. Jessica Stuart
    Naval Postgraduate School
    Monterey, California

4. Fred A. Kruse (Digital Only)
    Naval Postgraduate School
    Monterey, California

5. Richard C. Olsen
    Naval Postgraduate School
    Monterey, California

6. D. C. Boger (Digital Only)
    Naval Postgraduate School
    Monterey, California